博士論文

Research on Wireless Power Transfer System for PV Powered Lunar Rover with Maximum Power Point Tracking Control

（太陽電池給電月面ローバーのための無線電力
伝送システムと最大電力追従制御に関する研究）

氏　　名　　Ji Bingcheng

（季　炳成）

THE UNIVERSITY OF TOKYO

DOCTORAL THESIS

Research on Wireless Power Transfer System for PV Powered Lunar Rover with Maximum Power Point Tracking Control

(太陽電池給電月面ローバーのための無線電力伝送システムと最大電力追従制御に関する研究)

Author: Bingcheng JI

Supervisor: Prof. Yoichi HORI

A thesis submitted in fulfillment of the requirements for the degree of Doctor of Philosophy

in the

Department of Advanced Energy
Graduate School of Frontier Sciences

February 9, 2020

Abstract

With the rapid developments of economy and technology in the past decades, the Moon exploration activities are focused all over the world. As one of the most convenient instruments for lunar investigations, the lunar rover has achieved great developments in various areas, such as the lunar magnetic field distribution, water existence and Moon origin as well as evolution. So far, almost all the launched lunar rovers are powered by the PV panel, and the solar irradiance at lunar day can be utilized to generate electricity to be stored to provide energy to the lunar rover at lunar night. However, in the conventional lunar rover structure, the PV panel is connected to the rover instruments via a wire connection through the multilayer insulation (MLI) materials which is employed to block the heat exchange between the rover inside instruments and outside circumstances. Because the wire connection brings about a slit on the MLI materials, there will be a heat leakage from the internal instruments to the outside at lunar night. Because the rover internal temperature is kept by the thermal management system which is powered by battery, the heat leakage will need extra battery volume to cover the thermal dissipation. Therefore, the extra battery volume will cause excess burden to the lunar rover launch mission.

In this paper, a wireless power transfer (WPT) system is proposed for lunar rover to replace the conventional wire connection in order to avoid the heat leakage at lunar night. The main content can be summarized into three parts: a novel lunar rover WPT system is proposed; a simulated annealing (SA) method to track the maximum DC-to-DC efficiency of the WPT system with parameter variations is proposed; two PV maximum power point tracking (MPPT) methods under partial shading conditions are proposed. The paper is organized as follows.

Chapter 1 introduces the recent lunar rover developments and analyzes the corresponding unsolved problems. In recent years, various lunar rovers have been launched to the Moon surface to conduct the lunar investigations, and currently, there are more lunar rover projects planned for the future. However, there are two issues which still need to be paid attention to, namely the heat leakage and PV MPPT under partial shading conditions. With the theory and simulation analysis, it can be concluded that for the lunar rover 1 W heat leakage power should be covered by approximately 2 kg lithium battery. Based on the designed lunar rover parameters, the expected heat leakage will be approximately 20 W, indicating there should be at least 40 kg lithium battery required to balance the thermal dissipation and generation. Furthermore, when the lunar rover moves on the Moon surface, the PV panel is highly probable to be partially shaded. In this case, in order to make the most of solar energy, the PV global MPPT control should be conducted.

Chapter 2 presents the proposed lunar rover WPT system structure and the PV output property with different solar irradiance cases. In the proposed lunar rover structure, the conventional wire connection is replaced with a WPT system, and in this way, there is no slit on the MLI materials, indicating the heat leakage is completely avoided at lunar night. Furthermore, the PV output property is analyzed based on the 1-diode and 2-diode PV cell models, and it is concluded that when the solar irradiance on the PV panel is not uniform, namely the PV panel works under the partial shading conditions, the global MPPT control should be conducted to make the full utilization of solar energy.

Chapter 3 presents the proposed lunar rover WPT systems. Based on the position of the converter used to conduct the PV MPPT control, the proposed WPT systems can be divided into the transmitter side converter (TC) WPT system and

receiver side converter (RC) WPT system, respectively. The feasibility of the TC and RC topologies in the PV MPPT control aspect is analyzed respectively, and both of them can meet the MPPT tracking accuracy and time requirements. Furthermore, considering the Moon surface circumstances and the lunar rover structure, the TC and RC topology WPT system feasibility for the lunar rover application is analyzed. Mainly based on the circuit device limitations, the RC topology is more applicable for the current lunar rover designs.

Chapter 4 presents the power management strategy for the TC and RC topology lunar rover WPT systems. The WPT system is composed of 3 parts which are related to the energy supply/requirement, and they are the PV, battery and load. The PV and load are the power supply and request respectively, and the battery is employed to achieve the system power balance. Considering the Moon surface solar irradiance distribution and lunar rover mission design, 6 working modes are designed for the lunar rover. Furthermore, based on the different topologies of TC and RC WPT systems, different system control methods are employed. The proposed power management strategy and control methods are verified by experiments.

Chapter 5 presents the maximum DC-to-DC efficiency tracking method of WPT system with parameter variations. Due to the extreme temperature conditions of the Moon surface, the WPT system transmitter side which is exposed to the lunar circumstances will encounter the circuit device parameter variations. With the parameter variations, the DC-to-DC efficiency of the whole WPT system will be sharply reduced with the preset nominal system parameters. Considering this issue, in this paper, a SA method is proposed to track the maximum value of the WPT system DC-to-DC efficiency. The proposed SA method is verified with simulations.

Chapter 6 presents the proposed PV MPPT algorithms under working conditions. In order to make the most of solar energy on the Moon surface, the PV MPPT control should be conducted. Based on the solar irradiance uniformity, the algorithm can be divided into the local and global MPPT algorithms. When the solar irradiance is uniform, the PV only possesses one peak at the power-voltage (P-V) curve, and local MPPT algorithm can track the power peak. In this paper, the variant step incremental conductance (InCon) method is proposed. In the proposed method, the power peak height is employed to tune the variant step to improve the tracking time sensitivity and accuracy. When the solar irradiance is not uniform, namely the PV works in the partial shading conditions, the PV outputs multiple peaks with respect to voltage. Therefore, the global MPPT method should be employed to track the power maximum. In this paper, two global MPPT algorithms are proposed, namely the simulated annealing assisted particle replaced Gaussian particle swarm optimization (SA-PR-GPSO) method and the simulated annealing assisted particle jump particle swarm optimization (SA-PJ-PSO) method. In the SA-PR-GPSO algorithm, the tracking process is divided into two stages. In this first stage, the particles at each iteration are replaced with Gaussian distribution to achieve the fast convergence, and in the second stage, the accurate optimal position tracking is conduced with GPSO method. Based on the two-stage algorithm structure, the tracking time will be reduced while the tracking accuracy will be increased. On the other hand, in the proposed SA-PJ-PSO algorithms, the two-stage algorithm structure is also employed, while in the first stage the fast particle convergence is achieved with particle jump and in the second stage, the accurate particle positioning is conducted with PSO algorithm. All of the 3 proposed algorithms are verified with experiments.

Chapter 7 summarizes the main research contents and also analyzes the future research prospects of the proposed combined method of PV and WPT system.

In this paper, a novel lunar rover WPT system is proposed to replace the wire connection in the conventional structure. The PV power can be transferred via magnetic coupling in the WPT system, and then the heat leakage at lunar night can be avoided. The PV MPPT control is achieved with a receiver side converter and in this way the transmitter side facility can be effectively reduced. Furthermore, considering the potential parameter variations caused by harsh Lunar circumstances, a SA method is proposed to track the maximum system DC-to-DC efficiency when the parameter variations happen. Finally, in order to conduct the global MPPT control when the lunar rover PV works under partial shading conditions, a SA-PR-GPSO and SA-PJ-PSO methods are proposed to accelerate the tracking process with fast particle position convergence.

Acknowledgements

Great oaks from little acorns grow. The journey to the current place has been an extremely long one and it has been made succeeded based on the numerous precious help from dozens of people. At the peak of what will be a truly prodigious list, appreciation and pride of place goes to my dissertation committee.

First and foremost, I would like to express my deepest and most sincere gratitude to my supervisor, Prof. Yoichi Hori. Prof. Hori has been an enlightening inspiration to me since I read his paper when I was in my master first year. I am extremely honored and thrilled I can become a member of his group. In the whole process of the past Ph.D. course, Prof. Hori has guided my research with precious advice, constant encouragement, great patience, priceless understanding and invaluable concern. Not only the research methodology and ability have I learned from him, but also the life altitude of always seeking the excellence has left me an indelible mark in my mind, which is a bright lamp that illuminates my life and points my way forward. Rivers pushes us to the vast sea and the dawn brings us bright morning. I am so grateful to Prof. Hori for the world exposed to me which I will never otherwise see and experience on my own.

I want to extend my gratitude to Prof. Fujimoto for his guidance and wisdom throughout my Ph.D. course from the inception to the completion. The precious advice and unwavering patience he has gave me have supported me to conduct my research. I have learned so much from Prof. Fujimoto of research enthusiasm, logical thinking and curiosity to knowledge. Without his patient instruction, the research project can not achieve the current level.

I also want to bring my profound appreciation to the dissertation committee members, Prof. Ohsaki, Prof. Koseki, Prof. Takamiya and Prof. Baba. I am so grateful to the invaluable academic comments, questions, criticism, support and encouragement.

Furthermore, I want to bring the warmest appreciation to Prof. Imura and Prof. Hata. The impressive wisdom and rigorous approach to research have instructed me throughout the research project process. The scrupulous altitude, devoted hard-working and unobtrusive patience are what I will learn from in my whole life.

I would like to express my sincere gratitude to Mrs. Sayuri Honda, Mr. Shuhei Shimada and Mr. Osamu Kawasaki. In the collaborated research project with JAXA, I have obtained the strongest support, most patient understanding and specific guidance. I am so grateful and honored to be able to take part in the JAXA project.

I also want bring my honest appreciation to the friends in our lab, Ri, Kenta, Takahashi, Utsu, Nawada, Helanka, Tantan, Koh, Matsumoto. I am grateful that all of you have communicated with me with great patience and understanding even though I can not speak Japanese very fluently. The friendship between us has made me I am still beloved and I want to keep the friendship forever. Furthermore, I would like to extend my gratitude to my friends, Xingyu, Qianmiao, Xiaoliang, Danyang, Lele, Mingyang and Fengzhe, who can share the happiness when I have achieved some accomplishments and provide me help when I encounter setbacks.

Finally, I want to express my deepest gratitude to my family, my father, mother and sister, who have constantly given me infinite love, encouragement, patience, concern and support. Thank you so much I can grow up in love. You are the reason that I can take the way up here and I love you all dearly.

Contents

List of Figures

List of Tables

This dissertation is dedicated to my family who instilled in my virtues of perseverance and commitment and relentlessly encouraged me to strive for excellence.

Chapter 1

Introduction

1.1 Lunar Rover Developments

Lunar rover is one kind of vehicles which are driven on the Moon surface to investigate the lunar information, such as the water existence evidence, lunar magnetic field distribution and Moon evolution **[1]**. So far, various lunar rovers have been launched to the Moon surface and they have played irreplaceable roles in the Moon exploration of human beings **[2]**.

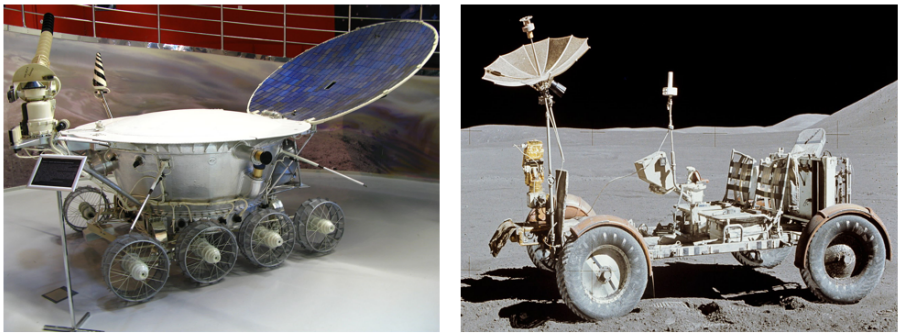

(a) (b)

FIGURE 1.1: Lunar rovers (a) Lunokhod 1 **[4]**. (b) Apollo **[5]**.

As the first polycrystalline-panel-powered lunar rover, Lunokhod 1 was launched to the Moon surface in 1969 **[3]**. It is the first remote-controlled robot to land on another celestial body in Fig. 1.1. In 1971 and 1972, the Apollo rover was launched for the Project Apollo to carry the astronauts and equipments **[6]**. Furthermore, it also can be employed to communicate with the earth side for the information transfer. In 1973, as a monocrystalline-panel-powered of two unmanned lunar rovers, Lunkkhod 2 was launched to the Moon surface **[7]**. The main missions included the Moon surface image analysis, ambient light level investigation, laser ranging experiment conduction, lunar local magnetic field measurement and Moon surface soil mechanics analysis. In 2018, as the second lunar rover of China, Yutu 2 rover was launched to the far side of Moon surface **[8]**. In order to conduct the required investigations, there are various equipments carried in the rover, such as the panoramic camera to obtain the Moon surface images, lunar penetrating radar to analyze the Moon surface soil elements, visible and near-infrared imaging spectrometer for identification of surface materials and atmospheric trace gases and advanced small analyzer for neutrals to investigate the interactions between the solar wind from the Sun and the Moon surface soils **[9]**.

For the future Moon exploration carried out by lunar rovers, various researches have been planned all over the world. In 2022, a volatiles investigating polar exploration rover (VIPER) is planned to be launched by NASA to the Moon south polar region to search for the water ice evidence **[10]**. The designed mission is expected that the lunar rover will explore the Moon surface for several miles for more than 100 days and will drill into the Moon surface soils to obtain element samples. The samples will be analyzed in the carried onboard instruments to search for the water ice existence evidence. Furthermore, also planned by NASA, the All-Terrain Hex-Legged Extra-Terrestrial Explorer (ATHLETE) is a six-legged robotic lunar rover test-bed under development by the Jet Propulsion Laboratory (JPL) **[11]**. The design objective of ATHLETE is to be employed in a wide range of terrains with roll and walk operations.

1.1.1 Lunar Circumstances Limitation Factors

Compared with the earth environment, the Moon surface is an unique circumstance in which various factors will be hazardous for the earth creatures.

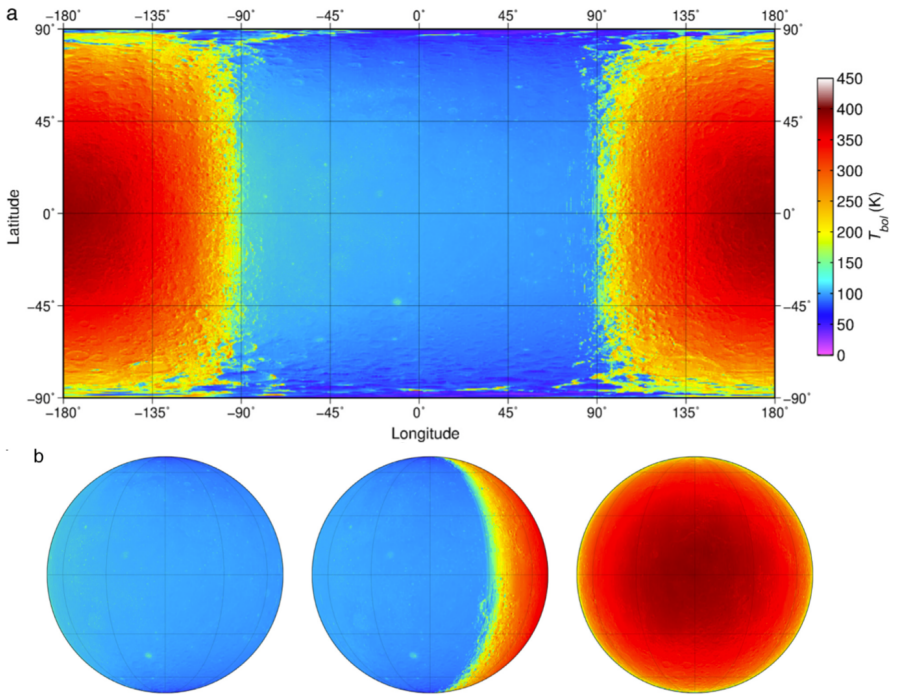

FIGURE 1.2: The solar irradiance and temperature distribution on the Moon surface **[12]**.

The first factor which should be focused is the lunar day and night. The rotation period of the Moon on the axis is approximately 27 earth days, 7 hours, 43 minutes, and 12 seconds **[13]**. On the near side of the Moon surface, the daytime lasts approximately for 13 and a half earth days, and the darkness will also last for the same time in the following in Fig. 1.2. As we know, almost all the launched lunar rovers are powered by the PV panel and then it can be concluded that the lunar rover should work at lunar day and sleep at lunar night **[14]**. The generated power by the PV panel at lunar day should be stored in the lunar rover for the lunar night preparation.

Secondly, the Moon surface temperature should be analyzed. At lunar day, for the area with solar irradiance, the Moon surface temperature will go up to 150°C,

and on the contrary, at lunar night, the surface temperature is as low as -100°C **[15]**, **[16]**. Furthermore, the Moon surface temperature varies with different positions all across the Moon surface. Therefore, the lunar rover internal thermal management system should be the key factor which can determine the lunar rover working life **[17]**. No matter it is the lunar day or night, in order to protect the rover instruments, the rover internal temperature should be kept at the room temperature, namely 25°C.

Thirdly, the solar irradiance distribution on the Moon surface should be focused. The Moon tilts on the axis approximately 1.54 degrees, which is far less than that of the earth (23.44 degrees) **[18]**. Therefore, it can be concluded that on the Moon surface there is no season changing while the Moon revolutes around the Sun **[19]**. In this way, there are some places on the Moon surface in which there is no solar irradiance all the time.

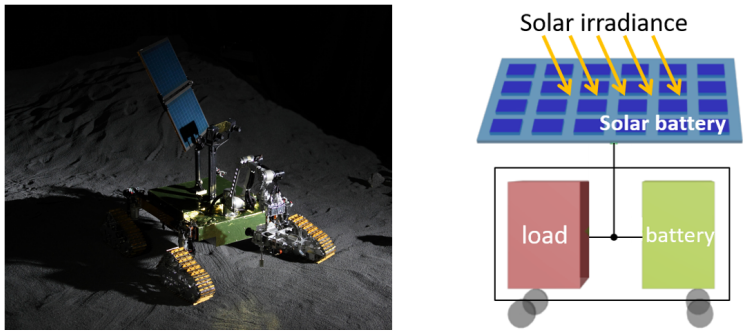

(a) (b)

FIGURE 1.3: (a) Lunar rover prototype **[25]**. (b) Lunar rover structure.

Fourthly, there is no air on the Moon surface and then there is no wind to blow the lunar dust up **[20]**. However, because the lunar dust diameter is extremely short it can be lifted up to float around the lunar rover by the tire rotation while it moves on the Moon surface **[21]**.

Fifthly, there are various radioactive rays on the Moon surface from the universe, and they are hazardous to the semiconductor devices because the 1 and 0 states can be changed **[22]**, **[23]**.

1.1.2 Lunar Rover General Structure

So far, almost all of the landed lunar rovers are powered by the PV panel and the battery banks are employed to store the generated power for lunar night **[24]**.

In general, the lunar rover structure can be expressed in Fig. 1.3(b). The conventional lunar rover structure consists of two parts, namely the external part and internal part. The external part is mainly composed of the PV panel. The internal part is mainly the rover body which is protected by the MLI materials to block the thermal exchange between the rover body and outside circumstances **[26]**. The instruments in the rover body mainly include the load and battery. The connection to transfer the power from the external part and to the internal part is conducted with a wire. However, because the rover body is covered by the MLI materials to approach thermal insulation, due to the wire connection, inevitably there will be a slit on the MLI materials **[27]**, **[28]**.

Based on the lunar rover structure, it can be concluded that at lunar day, the generated power can be transferred from the PV panel to the rover body with the

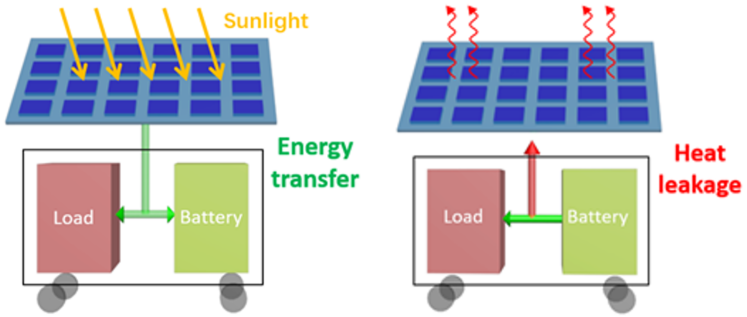

(a) (b)

FIGURE 1.4: (a) Power generation at lunar day. (b) Heat leakage at lunar night.

wire connection. Because the outside temperature is too high, the thermal assistance system will keep the internal temperature as the room temperature. At lunar night, because there is no solar irradiance which can be utilized by the PV panel, the lunar rover should sleep to save the power **[29]**. In this time, the thermal assistance system will also generate heat to maintain the preset internal room temperature to protect the instruments **[30]**.

1.1.3 Lunar Rover Current Development Limit

1.1.3.1 Lunar Rover Heat Leakage at Lunar Night

However, because in the conventional structure, the PV panel is connected to the rover side with a wire connection, unavoidably, there will be a slit on the MLI thermal insulation materials. At lunar night, because the outside temperature is extremely low (-100°C), there will be a heat leakage from the rover body internal part to the outside circumstances as shown in Fig. 1.4. Based on the lunar rover structure, there will be two kinds of heat leakages: the heat radiation through the slit to the outside and heat conduction along the wire to the outside.

The radiation heat leakage is caused by the gap between the wire and MLI materials. However, even though in theory the gap can not be completely avoided, with a certain designs, the heat leakage amount caused by the radiation can be omitted under working conditions. However, compared with the radiation heat leakage, the conduction heat leakage is relatively tremendous at lunar night. Due to the Wiedemann-Franz Law, the thermal and electrical conductivities possess a positive correlation, indicating the wire connection will also possess high thermal conductivity in expectation.

At lunar night, due to the huge temperature difference between the internal rover body and outside circumstances, it can be expected that there will be a heat leakage along the wire connection from the inside to the outside as shown in Fig. 1.4. The heat conducted from the internal circumstances will dissipate into the surrounding space. However, because the wire is connected to the PV panel, the heat dissipation from the wire will be accelerated because the PV panel can be seen as a radiator. Considering the PV panel area, the acceleration effect will cause more severe heat leakage from the rover body. Based on the rover internal thermal management system capability and battery property, when the heat leakage power is equal to 1 W, it needs nearly extra 2 kg lithium battery to power the system to generate equal amount heat. With theory analysis, the power of lunar rover heat leakage is expected

to be 20 W indicating there will be extra 40 kg lithium battery required, which is extremely uneconomical for the lunar rover launch and developments. Therefore, it is urgent for the lunar rover to find a method to remove the wire connection which can cause heat leakage at lunar night and still effectively transfer generated power from PV panel to the rover body at lunar day.

1.1.3.2 Lunar Rover PV Partial Shading Conditions

Another issue which has influenced the lunar rover developments is the PV partial shading conditions while lunar rover drives on the Moon surface.

PV is device based on the photovoltaic effect which can transform the light into electricity under working conditions. When the solar irradiance on the PV panel is uniform, the PV output power will only possess 1 peak with respect to voltage shown in Fig. 1.5. Therefore, the local MPPT control algorithm can achieve the tracking mission.

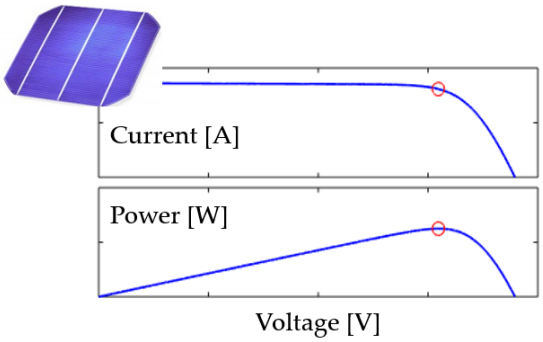

FIGURE 1.5: PV output property with uniform solar irradiance.

When the solar irradiance on the PV panel is not uniform, in other words, the PV panel works under partial shading conditions, the PV output power monotonicity will be influenced by the solar irradiance distribution. In general, there will be multiple peaks with respect to voltage as shown in Fig. 1.6. Because there are multiple power peaks with the voltage variations, the global MPPT control should be conducted.

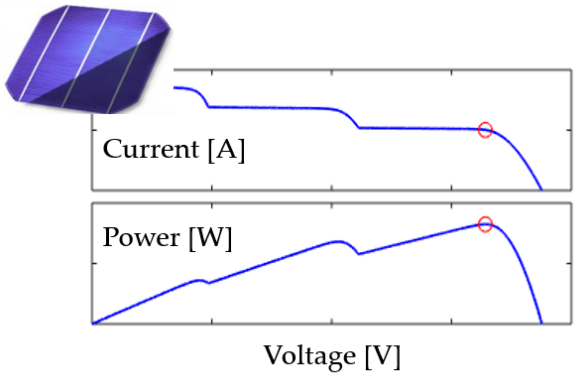

FIGURE 1.6: PV output property under partial shading conditions.

However, when the lunar rover runs on the Moon surface, the probability that the PV works under partial shading conditions is extremely high. The shadow on

the PV can be divided into three types based on the origin: (1) Moon surface terrain; (2) lunar rover other instruments; (3) lunar dust.

The shadow caused by the Moon surface terrain is very huge and while the lunar rover moves on the Moon surface, the shadow can be seen to be constant. The partial shading conditions caused by the terrain shadow can be ignored. On the other hand, the shadow caused by other instruments can be reduced and even avoided by the lunar rover structure optimization. Finally, the shadow of lunar dust is the key factor which leads to the partial shading conditions for the lunar rover under working conditions. When the lunar rover lands on the Moon surface, the lunar dust will be blown up and then float on the top of the lunar rover PV panel. On one hand, the floating dust will block the solar irradiance, and then the partial shading conditions happen. Furthermore, on the other hand, the dust will gradually drop on the PV panel and then will cause the permanent partial shading issues for the lunar rover. Apart from the lunar dust caused by the landing process, the dust also can be caused by the tire rotation while the lunar rover drives. Therefore, in the working life of lunar rover, more and more lunar dust will accumulate on the PV panel causing increasingly severe partial shading issues. Therefore, the global MPPT control is required for the lunar rover.

Therefore, this paper is organized centering two main topics, namely the lunar rover WPT system design and PV MPPT control under partial shading conditions.

1.2 Wireless Power Transfer System Developments

Due to the increasingly serious energy crisis and environment issue, the electrification has been promoted in various areas, such as the electric vehicle (EV), high-speed railway and electric aircraft (EA) **[31]**, **[32]**, **[33]**. In the conventional methods, the electricity is transferred with wire, which is extremely simple to be implemented. However, the drawbacks are also obvious. For example, the broken wire will lead to security risks and inconvenience issues. Furthermore, the conventional wire electricity transfer method can not meet the requirements of special cases, such as the underwater and oilfield areas **[34]**, **[35]**.

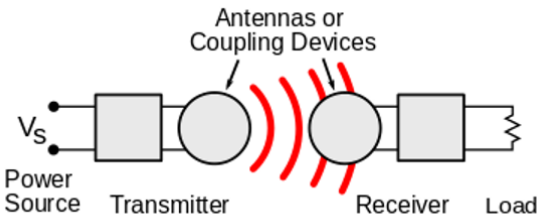

FIGURE 1.7: Wireless power transfer system structure **[36]**.

Considering these issues, the WPT system has been proposed as shown in Fig. 1.7, and the initial attempt can be traced in the late 19^{th} century by Nikola Tesla in Fig. 1.8 **[37]**. However, due to the technology limits at that time, the WPT exploration didn't achieve the designed aims. In 2007, due to the enlightening research of MIT research team **[39]**, the WPT has been focused all over the world, and the WPT system has achieved great developments in recent years. So far, the WPT system has been employed in various areas, such as the static and dynamic EV charging, electrified railway, medical implants and Internet-of-Things (IoT) **[40]**, **[41]**.

(a) (b)

FIGURE 1.8: (a) Nikola Tesla. (b) The WPT system employed in Nikola Tesla's experiment **[38]**.

1.2.1 Current Main WPT methods

Based on the implementation mechanism, the WPT can be divided into the following categories.

1.2.1.1 Laser and Microwave Long-distance WPT System

Compared with the near field power transfer area, the far field transfer has not achieved great enough progress and developments in recent years. However, it still holds tremendous potential capability to transform and revolutionize the current society power utilization and transfer system **[42]**. So far, the far field power transfer is almost conducted based on the microwave and laser **[43]**, **[44]**.

Generally speaking, microwave is a form of electromagnetic radiation whose frequency is always defined in the range of 300 MHz-300 GHz of a wavelength range of 1 mm-1 m. Since the far field power transfer is proposed, various research has been carried out to verify the feasibility. In 1975, a microwave power transfer verification experiment was conducted in the JPL Goldstone Facility and the whole system efficiency has approached approximately 84% at the power of 450 kW. The power was transferred from Klystron at 2.388 GHz and the distance until the receiver side is 1.6 km **[45]**. In Europe, a ground-to-ground microwave power transfer experiment was carried out in Reunion island with the power of 10 kW and the distance of 700 m. The employed microwave frequency was set as 2.45 GHz. Based on the established prototype, the power transfer efficiency has approached about 57% **[46]**.

Apart from the microwave, laser is another candidate which is always employed in the far field power transfer area. Compared with the microwave form, laser has possessed a great advantage that the receiver side can be implemented with PV panels. The simplicity of the laser power transfer is the main merit over other wireless power transfer systems. However, because the transform between the electricity and laser is based on the low-efficiency photovoltaic effect, the laser power transfer is less researhed compared with the microwave method **[47]**. A distributed laser power transfer experiment has been conducted to verify the laser application feasibility **[48]**. With the waveform of 1550 nm, the laser experiment has approached the efficiency of 13.5% when the distance is set as 50 m. Even though the laser facility is smaller than the microwave form, the low efficiency will unavoidably influence the power transfer efficiency.

1.2.1.2 Magnetic Coupling Induction WPT

One of the most important power transfer method in the near field area is the magnetic coupling induction (MCI) WPT method **[49]**. In general, the MCI WPT system can be divided into two sides, namely the transmitter and receiver sides. At each side, there is a coil established in the circuit and the two sides are coupled via magnetic field under working conditions **[50]**. In the MCI WPT system, the power can be transferred from the transmitter side to the receiver side based on the magnetic coupling. The magnetic coupling is generated by an AC power source, and the coupling factor between the transmitter and receiver coils is the key factor which can determine the transferred power and efficiency.

FIGURE 1.9: MCI wireless charger for smartphone.

So far the MCI WPT system is mainly employed in the low power cases, such as the wireless charge toothbrush, smartphone in Fig. 1.9 and razer. Furthermore, the coil distance between the coils should be set to be close enough to approach the high power transfer efficiency. When the system power increases, the MCI WPT system efficiency will be reduced sharply and it can not meet the system requirements **[51]**.

1.2.1.3 Magnetic Coupling Resonance WPT

Considering the disadvantages of the conventional MCI WPT system, the magnetic coupling resonance (MCR) WPT system has been developed in recent years. The MCR WPT system was first proposed in the AIP Industrial Physics Forum in 2006, and then the enlightening research was published in 2007 **[39]**. In the paper, with a distance of 2 m, a 40 % efficiency 60 W power transfer has been achieved.

FIGURE 1.10: MCR electric vehicle wireless charger.

In the MCR WPT system, in order to cancel the inductor impedance, capacitors are employed in the circuit **[52]**. With the assistance of capacitors, the circuit will

express purely resistive property under working conditions and there will be no reactive power generated, indicating the whole system efficiency can achieve the maximum value **[53]**. Compared with the MCI WPT system, the MCR WPT system can be employed in higher power cases, such as the electric vehicle charging as shown in Fig. 1.10, and furthermore, the system ability of misalignment tolerance is also higher **[54]**. In this paper, the MCR WPT is employed in the lunar rover and will be analyzed in this research. To be simple, the MCR WPT is called as WPT in the following parts in this paper.

1.2.2 Main WPT Topologies

Based on the connection methods of the capacitor and inductor, the main WPT system can be divided into the topologies in Fig. 1.11 **[55]**, **[56]**, **[57]**.

Based on Fig 1.11, when there is only one compensate device employed at each side of the WPT circuit, the main topologies include the series-series (SS), series-parallel (SP), parallel-series (PS) and parallel-parallel (PP) structures. Furthermore, when there are two compensate devices, the main topologies are the LCL and LCC structures.

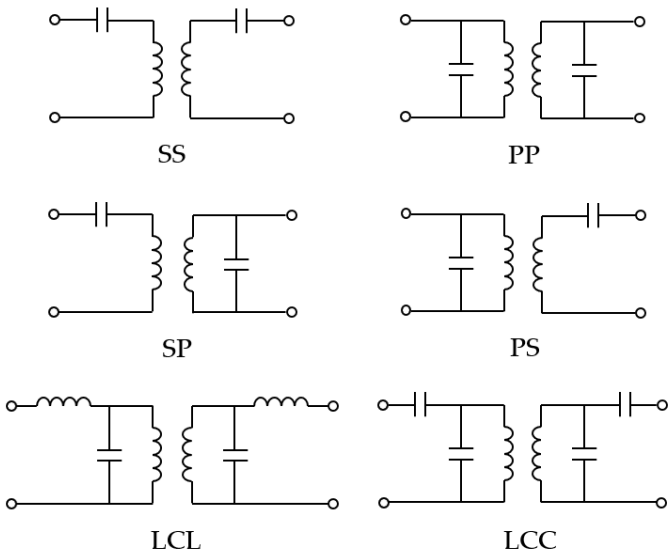

FIGURE 1.11: Main WPT system topologies.

With more compensate devices, the circuit can express more complicated functions **[58]**. For example, there is only one capacitor at both sides in the SS topology, and the capacitors can cancel the circuit impedance with accurate designs to make the circuit be purely resistive **[59]**. However, the transmitter side power is related to the coupling factor. The source output power increases with the coupling factor decreasing, generating extremely high transmitter side current which is not safe for the whole system **[60]**. For the LCL topology, when the coupling factor decreases, the transmitter side current can be kept at a steady level while the source output power is still changed. When there are 3 compensate devices in the circuit for the topology, the output power is stable against the coupling factor but too many devices seriously not only degrade the circuit simplicity but also reduce the whole system

efficiency **[61]**. Therefore, even though the topology with multiple compensate devices possesses more excellent properties, it only can be employed in the low power situations.

1.2.3 WPT Research and Applications

So far, the WPT system has been employed in various areas, such as the electric vehicle (EV), Internet-of-Things and medical instrument. A 4 kW SS WPT system is proposed to charge the EV at the efficiency of 98% and 96.6% when the coil air gap is set as 4 cm and 8 cm, respectively **[62]**. Furthermore, the CC and CV working modes can be effectively switched based on the battery charged capacity under working conditions. A novel uniform voltage gain frequency control is proposed to maintain a stable power transfer when there is some misalignment between the transmitter and receiver side coils. In this paper, the proposed method is valid to the horizontal and vertical misalignments **[63]**. An EV WPT charge system design method is proposed to consider the the influence of vehicle modules to the WPT property, such as the efficiency, EMF radiation, air gap and position misalignments. The proposed design method is verified with the Kangoo Renault experiment **[64]**. A SS design method for EVs is proposed, and the WPT coil magnetic analysis method is improved in this paper. Compared with the conventional magnetic analysis method, the proposed coil magnetic model can reduce the calculation cost **[65]**. A 60 kHz WPT system is proposed for a tram, and the system has the characteristics of low flux density and high efficiency with a large air gap. Furthermore, the system power is set as 180 kW and the efficiency is approximately 85% under working conditions **[66]**. A WPT equivalent model is proposed to further explore the WPT system property, such as the air gap, magnetic flux density and transfer efficiency. Based on the finite element analysis and experiments, the proposed model is verified of the power loss caused by the skin and proximity effects **[67]**. A 5 kW EV WPT system is proposed and the efficiency from the grid to the EV battery with various coupling conditions is approximately higher than 90%. The efficiency is improved with a vocel dual side control scheme of the whole system, and the efficiency approaches 7% increase and the loss achieves a 25% decrease **[68]**. A novel WPT system is proposed for a online EV, and the transmitter side rail is narrow, indicating a small pickup receiver coil will cover the effective magnetic coupling zone when the EV drives. When the air gap and misalignment are 20 cm and 24 cm respectively, the system efficiency achieves 74% with the power of 27 kW **[69]**. A novel omnidirectional WPT system is proposed for 3D applications, and the WPT mathematical model is focused. Because there are 3 coils employed at the transmitter side, the receiver side coil can be placed at the arbitrary positions with effective power transfer under working conditions **[70]**. A novel WPT model is proposed to focuse the system properties such as the frequency splitting when the coupling factor is too high, maximum misalignment tolerance with the precondition of effective power transfer and system behaviours when it is uncoupled **[71]**. A concrete WPT system is proposed and in order to effectively transfer power in the concrete circumstances, a novel coil design method is proposed. The employed 4-coil WPT system can effectively enhance the magnetic coupling under working conditions **[72]**. A WPT magnetic field distribution analysis method is proposed, and in this method, a detailed field-circuit coupling model is employed to investigate the coupling intensity with the consideration of near field strength and circuit constraints **[73]**. A design method for a millimeter size implantable biomedical device is proposed and the optimal operation frequency and coil structure are focused. The proposed design method is verified with a full-wave electromagnetic

field simulations and experiments. The prototype with 1 mm diameter achieves PTE of 0.56% and the transferred power is 0.244 mW at 200 MHz with a distance of 12 mm **[74]**. A wireless transcutaneous power transfer system is proposed, and the heat caused by the coil skin and proximity effect is emphasized in this paper. With the proposed method, the designed system can achieve a power transfer of 30 W with a efficiency of 95% when the coil distance is higher than 20 mm or 70 mm under working conditions **[75]**.

1.3 PV MPPT Control Analysis

PV is one of the most important modules for lunar rovers, and it can provide the required power to accomplish the preset missions. PV is a device based on the photovoltaic effect that can transform light into electricity **[76]**, **[77]**. So far, PV has been widely employed in various areas, such as the solar plant, household independent grid, and space exploration **[78]**.

In general, the PV output capability is related to the solar irradiance intensity and distribution on the panel **[79]**. Furthermore, the PV output power is a function to the output voltage, indicating that with output voltage variation, the PV output power also changes **[80]**. Therefore, in this case, in order to make the most of the solar energy, the MPPT control should be conducted. Because the PV output power is closely related to the solar irradiance distribution on the PV panel and considering different solar irradiance cases, the local and global MPPT algorithms should be conducted **[81]**.

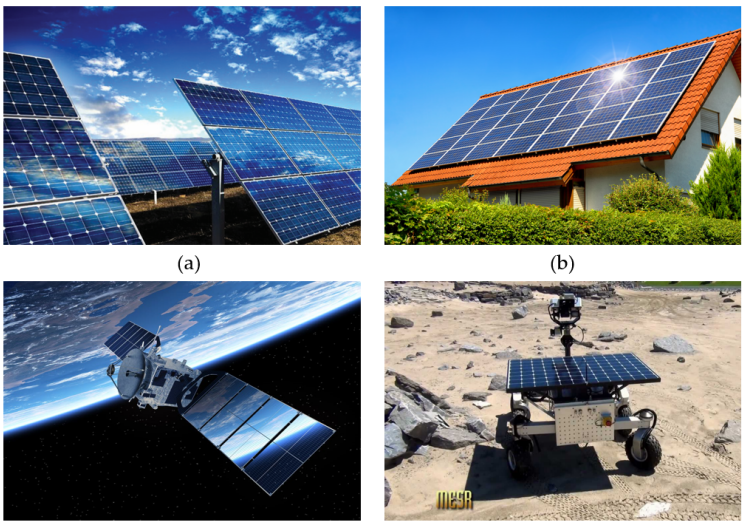

(a) (b) (c) (d)

FIGURE 1.12: (a) PV power generation plant. (b) Household PV application. (c) Satellite PV application. (d) Lunar rover PV application.

1.3.1 Local MPPT Algorithm Analysis

When the solar irradiance on the PV panel is uniform, there is only one peak at the P-V curve and the local MPPT algorithm can be employed. A novel three-point perturb&observe (P&O) method is proposed to reduce the PV output power oscillation when the maximum power point is tracked. Compared with the conventional P&O

method, the proposed method can determine the working point with higher accuracy based on the previous two steps in the tracking process **[82]**. A variant step InCon method is proposed to eliminate the division calculations in the conventional InCon method. Furthermore, when the solar irradiance change is detected, the proposed InCon method sampling time will be improved to speed the tracking stage **[83]**. A combined method of ripple correlation control and xtemum seeking control is proposed to reduce the power oscillation in the stable state and the tracking time. Based on the experiment verification, the convergence time is low and the tracking accuracy is at least approximately 97.4% **[84]**. A novel extremum seeking control method is proposed to deal with the rapidly varying solar irradiance cases. the natural inverter ripples are employed in the proposed algorithm and the tracking performance has achieved the accuracy higher than 99% **[85]**.

1.3.2 Global MPPT Algorithm Analysis

When the PV panel works under the partial shading conditions, the PV will output multiple-peak power with respect to voltage. In this case, in order to make the most of solar irradiance, the global MPPT control should be conducted under working conditions.

In order to track the maixmum power, there are mainly two kinds of global MPPT methods employed under working conditions, namely the sweep method and the stochastic metaheuristic method. In the sweep method, all the PV working points will be evaluated and the corrpesponding powers will be recorded. After the sweep process, the maximum power and the working point will be employed to control the PV working state and then the global MPPT can be achieved. Therefore, based on the working process, the sweep method can achieve the most accurate MPPT control because the all the PV working points can be exhaustively searched if the working point variation step can be set to be low enough. However, even though the sweep method can achieve the most accurate MPPT control in theory, there are two drawbacks of this method, namely the potential long tracking time and high computation cost. For example, in the sweep process, if the solar irradiance can keep constant, 1-time sweep will be enough to locate the optimal PV working point to achieve the global MPPT control under working conditions. However, under PV working conditions, the solar irradiance always varies and then in this case, the multiple-time sweep process will be required until the solar irradiance stabilizes. Therefore, in this case, the whole tracking time of the sweep process will be prolonged. On the other hand, in the sweep process, because all the PV working points will be tested and furthermore, if multiple times of sweep process are needed, the computation cost will be greatly increased. Therefore, in fact, even though the sweep method can achieve the most accurate global MPPT control, it is not widely employed in the PV applications.

Considering the drawbacks of the sweep method, the stochastic metaheuristic algorithms have been widely employed to excecute the PV global MPPT control. A stochastic metaheuristic algorithm is a heuristic procedure or process in which the optimal solution can be determined based on a series of search solutions under working conditions. Compared with the sweep method, all the system working points will not be evaluated exhaustively and the optimal solution is determined based on intelligient compuations and searches. Based on the different working principles, the stochastic metaheuristic algorithms mainly include the grey wolf optimization, firefly optimization, ant colony optimization, artificial bee colony optimization and so on. So far, the stochastic metaheuristic algorithms have been widely

employed in the PV global MPPT control. A novel fuzzy method is proposed to accelerate the tracking MPPT process and reduce the power oscillation in the steady state. The coarse and fine modes are employed in the proposed method and the PV maximum power and output power fluctuation are considered in the proposed fuzzy rules under working conditions **[86]**. A combined method of fuzzy algorithm and extreme learning machine is proposed. In the paper, the weather conditions are classified based on machine learning with the support vector machine and extreme learning machine methods. The simulation results show the proposed method can speed the tracking process when the weather abruptly changes **[87]**. A novel artificial neural network method is proposed to conduct the MPPT control with rapid weather variation. The artificial neural network is trained based on the particle swarm optimization and gravitational search algorithms based on fuzzy logic method **[88]**. A novel particle swarm optimization (PSO) algorithm is proposed for the PV MPPT control under partial shading conditions. The Lagrange Interpolation Formula is employed to guide the particle movements under working conditions. Based on the experiment results, the tracking accuracy is 97.09% and 97.97%, respectively **[89]**. A novel PSO algorithm with the particle overall distribution analysis is proposed to reduce the MPPT time. The particles are replaced based on the Cauchy distribution to achieve the fast convergence under working conditions. Compared with the conventional PSO algorithm, the MPPT time is sharply reduced and the tracking accuracy is also improved **[90]**. A combined method of ant colony optimization (ACO) and PSO algorithms is proposed to enhance the global maximum search ability. In details, the ACO and PSO algorithms conduct the global and local search under working conditions. The proposed method can reduce the tracking time and enhance the particle convergence ability **[91]**. A novel genetic algorithm (GA) is proposed and in this method, the employed GA algorithm can estimate the current voltage at the PV output power peak point based on the PV open circuit voltage and short circuit current data without the solar irradiance and panel temperature information **[92]**. A novel differential evolution algorithm is proposed to conduct the PV global MPPT control. The proposed method can possess strong robustness when the load changes and the search range for the global MPPT is wider, indicating the particle convergence ability is better **[93]**.

Based on the published papers, it can be concluded that various algorithms have been developed to conduct the global MPPT control for PV panel under partial shadings. The advantages and disadvantages are summarized in Tab 1.1 and 1.2.

The algorithms in Tab 1.1 and 1.2 can conduct the PV MPPT control under partial shading conditions.

1.3.3 Advantages and Disadvantages of Current Algorithms

Based on the summary in Tab 1.1 and 1.2, various algorithms can achieve the global MPPT control. However, due to each algorithm property, these algorithms also possess different advantages as well as disadvantages. For example, the Grey Wolf Optimiation (GWO) algorithm can achieve the global MPPT control with high tracking accuracy and robustness. Furthermore, when the global maximum is tracked, there is no stable state oscillation with further iterations and only few parameters need to be pretuned before the algorithm initialization. However, on the other hand, because the GWO algorithm traversal step is limited, there will be a great deal of iterations required to reach the stable state, indicating the long tracking time and high computation cost. Furthermore, the Artificial Bee Colony (ABC) algorithm possesses the advantages of high implementation simplicity, fewparameters to be pretuned and

high tolerance of initial parameters. However, due to the initialization parameters are not that important to drive ABC algorithm, it will take more iterations to evolute for appropriate parameters and this will lead to high computation cost as well as long tracking time.

Compared with other algorithms, the main advantages of PSO algorithm include the high implementation simplicity, few parameters to be pretuned, high robustness, high global max search capability, fast convergence capability, low computation cost and no required mathematical models. In particular the low computation cost and high implementation simplicity are the key merits. For example, in the PSO algorithm, the particle movements are achieved based on the particle velocity and position updates at each iteration. In the particle velocity and position update equations, the coefficients which should be pretuned are only the inertia weight, personal best acceleration coefficient and global best coefficient. In the PSO iteration process, with the guidance of the particle velocity and position updates, the employed PSO particles will move to the optimal position after enough iterations. Therefore, in this way, the PV MPPT control can be achieved. In the whole PSO iteration process, both the velocity and position updates are conducted with simple calculations and then the computation cost is low.

On the other hand, the PSO algorithm also possesses several disadvantages, such as the parameters which should be pretuned before the algorithm iteration and the intense fitness variation with the step-by-step particle movements. As analyzed above, there are 3 parameter should be tuned before the PSO algorithm starts. However, due to the wide applications of PSO algorithm in recent years, there have been various methods which can reduce the parameters which should be pretuned. For example, in the deterministic PSO algorithm**[94]**, the unknown parameters are set as 1 and in this way, the fast particle convergence can be achieved in some cases. Furthermore, in the Gaussian PSO algorithm**[95]**, the inertia weight is set as 1 and both the personal best acceleration coefficient and the global best acceleration coefficient are defined to follow the Gaussian distributions. In this case, the stochatisic process of particle movements will be guided with higher convergence capability. Another disadvantge of PSO algorithm is the intense fitness variation with the step-by-step particle movement. In order to solve this problem, some novel PSO algorithms have also been proposed. For example, a novel PSO algorithm is proposed and the InCon method is employed to assist the PSO algorithm to approach fast convergence**[96]**. In the algorithm, the InCon method is used to search the local PV output peaks and the PSO is employed to determine the global peak. In this way, the particle step-by-step position update can be conducted in a narrow range and then the intense fitness variation can be avoided.

Based on the above analysis, it can be concluded that the PSO algorithm possesses various advantages over other stochastic metaheuristic algorithms and the disadvantages also can be ameliorated with algorithm improvements. Therefore, in this research, the PSO algorithm is employed to conduct the PV global MPPT control under partial shading conditions.

TABLE 1.1: Summary of global MPPT algorithms 1

Algorithm	**Advantages**	Disadvantages
Grey wolf optimization	▷ High tracking accuracy ▷ No stable state oscillations ▷ High robustness ▷ Few parameters to be pretuned	▷ High calculation cost ▷ Too many iteration required for convergence ▷ Long tracking time
Firefly	▷ Fast convergence capability ▷ High tracking accuracy ▷ High escape capability from local max	▷ High calculation cost ▷ Parameters are updated at each iteration ▷ Long tracking time
Ant colony optimization	▷ High tolerance of initial parameters ▷ Fast convergence capacity ▷ High robustness	▷ High calculation cost ▷ Many parameters should be preset ▷ Complex algorithm structure
Artificial bee colony optimization	▷ Fast convergence capacity ▷ High robustness ▷ High tolerance of initial parameters	▷ High calculation cost ▷ Complex algorithm structure ▷ Low escape capability from local maxLong tracking time
Particle swarm optimization	▷ High implementation simplicity ▷ Few parameters to be pretuned ▷ High robustness ▷ High global max search capability ▷ Fast convergence capability ▷ Low computation cost	▷ Initial parameters should be pretuned ▷ Intense step-by-tep particle position updates

TABLE 1.2: Summary of global MPPT algorithms 2

Algorithm	**Advantages**	Disadvantages
Improved curve tracer	▷ High implementation simplicity ▷ No tracking limitations	▷ Low escape capability from local max ▷ Long tracking time
Extremum seeking control	▷ High implementation simplicity ▷ No mathematical models required ▷ high tracking accuracy ▷ High robustness	▷ High calculation cost ▷ Stable state oscillations ▷ Long tracking time
Simuated annealing	▷ Few parameters to be pretuned ▷ Simple implementation	▷ Low escape capability from local maxLong tracking time ▷ Stable state oscillations ▷ Parameter reinitialization when weather changes
Chaotic search	▷ High tracking capability when weather changes ▷ High robustness	▷ High calculation cost ▷ Tracking time dependence on step size
Cuckoo search	▷ Fast convergence capability ▷ Few parameters to be pretuned ▷ High robustness	▷ High calculation cost ▷ Tracking time dependence on step size
Genetic	▷ High global max search capability ▷ High robustness ▷ High solution tolerance in tracking process	▷ High calculation cost ▷ Low escape capability from local maxLong tracking time

1.4 Research Aim

As analyzed in the above sections, the most serious problem which has influenced the lunar rover developments is the heat leakage at lunar night. Therefore, considering this issue, the WPT system is expected to be employed to avoid the conventional lunar rover wire connection between the PV panel and rover body. However, due to the extremely high and low temperatures at lunar day and night, the WPT module parameters will deviate from the preset nominal values and the system efficiency will be sharply reduced. Futhermore, with the introduction of WPT module in the lunar rover system, the global PV MPPT control feasibility also should be focused.

Therefore, the research aims of this research mainly includes the following:

(1) Propose a lunar rover WPT system to avoid the heat leakage caused by the wire connection between the PV panel and rover body in the conventional structure at lunar night;

(2) Propose a method to track the lunar rover DC-to-DC efficiency when the parameter variations happen to the WPT system;

(3) Propose an improved PSO algorithm to conduct the lunar rover PV MPPT control under partial shading conditions with low computation time and faster convergence feasibility.

Chapter 2

Lunar Rover Structure and PV Property

2.1 Lunar Rover General Structure Analysis

Lunar rover is a vehicle which is designed to drive on the Moon surface to investigate the data of lunar magnetic field, water existence, Moon evolution, and so on. Because of the solar irradiance on the Moon surface, almost all of the launched lunar rovers are powered by the PV panel under working conditions. Based on the structure in chapter 1, the lunar rover mainly can be divided into two parts: the external part mainly including the PV panel and the internal part mainly including the carried instruments.

The external part is completely exposed in the lunar circumstances which is severely harsh for electronic devices. The Moon surface temperature is extremely different: on one hand, at lunar day, the temperature is higher than 150°C; on the other hand, at lunar night, the temperature is lower than -100°C, respectively. Apart from the temperature issue on the Moon surface, another problem is the radioactive rays from the universe. The radioactive rays will influence the working properties of electronic devices. Therefore, in order to improve the lunar rover system stability and reliability, the less controlled devices in the external part the better the improvement will be.

2.2 Thermal Analysis of Conventional Structure

In this section, in order to analyze the heat leakage at lunar night, a thermal simulation is conducted with ANSYS. The employed lunar rover structure parameters are shown in Tab. 2.1.

The thermal simulation is shown in Fig. 2.1. At lunar night, the outside temperature is set as -100°C, and the internal temperature is 25°C. Based on the simulation results, the following can be concluded.

(1) There is a heat leakage of 9 W along the wire connection from inside to outside at lunar night, and the PV panel acts like a radiator to enhance the heat leakage.

(2) The wire does not only cause the heat leakage, but also reduce the rover body internal temperature. Based on the simulation, the temperature of wire terminal in the rover body is approximately -70°C, which will bring about potential damages to the carried instruments.

Based on the above analysis, the lunar rover wire connection should be removed to avoid the heat leakage at lunar night while the power transfer still should be conducted at lunar day.

TABLE 2.1: Expected lunar rover structure parameters.

Item	Parameter
Body Length	150 mm
Body Width	150 mm
Body Height	150 mm
PV Length	200 mm
PV Width	150 mm
PV Height	10 mm
Wire Diameter	10 mm
Wire length	100 mm

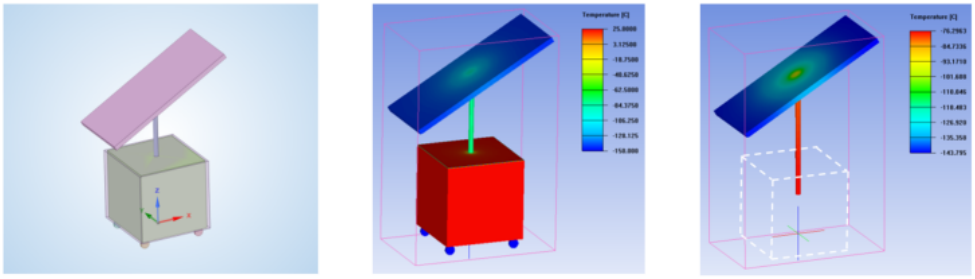

(a) (b) (c)

FIGURE 2.1: (a) Lunar rover structure design. (b) Heat leakage simulation. (c) Thermal distribution without rover body.

2.3 Proposed WPT Lunar Rover Structure

As analyzed above, the wire used to connect the PV panel and rover body is the heat leakage origin, and then in this section, the conventional wire connection is replaced with WPT system as shown in Fig. 2.2. In the proposed structure, at lunar day, the generated power can be transferred to the rover body based on the WPT system, and at lunar night, because there is no slit it can be expected that there will be no heat leakage. The thermal simulation of proposed WPT lunar rover structure is shown in Fig. 2.3.

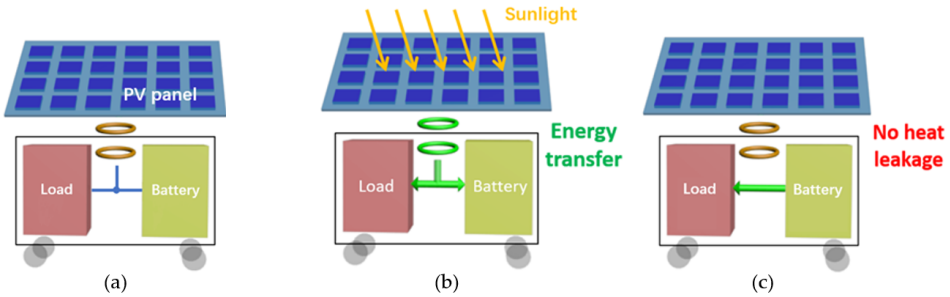

(a) (b) (c)

FIGURE 2.2: (a) Proposed lunar rover WPT structure. (b) Power generation at lunar day. (c) No heat leakage at lunar night.

Based on the thermal simulation, because there is no slit on the MLI materials, there will be no heat leakage from the lunar rover at lunar night as expected. Furthermore, the internal temperature also will not be influenced.

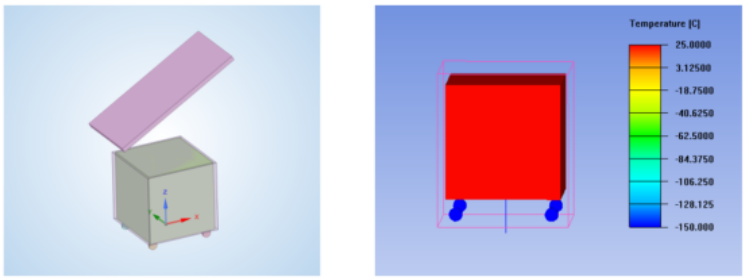

FIGURE 2.3: (a) Lunar rover WPT system structure. (b) Thermal simulation of WPT structure.

2.4 PV output property

In applications, each PV panel consists of a great deal of PV cells connected in series and parallel to enhance the output capability under working conditions. The PV cell model can be established based on the photovoltaic effect.

2.4.1 1-diode PV Cell Model

The 1-diode PV cell model **[97]** is shown in Fig. 2.4.

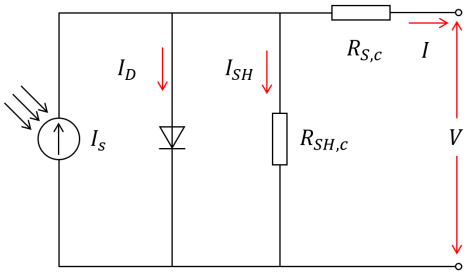

FIGURE 2.4: 1-diode PV cell model.

Based on the model, the PV cell output current I can be obtained as follows.

$$I = I_s - I_0 \cdot \left(e^{\frac{V + R \cdot I}{n \cdot V_t}} - 1 \right) - \frac{V + R_s \cdot I}{R_{sh}} \tag{2.1}$$

In the equation, I_s is the light generated current; I_0 is the leakage or reverse saturation current; n is the diode quality factor; R_s is the series resistance; R_{sh} is the shunt resistance. Furthermore, the light generated current I_s can be obtained as follows.

$$I_s = I_{ref} \cdot \frac{G}{G_{ref}} \cdot \frac{S_0}{S_{cell}} \cdot \left(1 + \alpha_{Isc} \cdot \left(T_C - T_{ref}\right)\right) \tag{2.2}$$

In the equation, ref stands for the reference conditions; G is the irradiance; T_c is the cell temperature; α_{Isc} is the temperature coefficient for short circuit current.

In addition, the diode reverse saturation current can be obtained as follows.

$$I_0 = I_{0,ref} \cdot \left(\frac{T_C}{T_{ref}}\right)^3 \cdot e^{\frac{E_g(T_{RES})}{n+k\cdot T_{ref}} - \frac{E_g(T_C)}{n\cdot k\cdot T_C}} \tag{2.3}$$

In the equation, k is the Boltzmann constant and E_g is the bandgap energy of the silicon.

Based on the above equations, it can be concluded that when the solar irradiance changes, the PV cell output current will also change, indicating the PV cell output power capability has been changed.

2.4.2 2-diode PV Cell Model

Apart from the 1-diode model, the 2-diode PV model **[98]** has also been focused in recent years because it can simulate the PV cell property with higher accuracy. The 2-diode model is shown in Fig. 2.5.

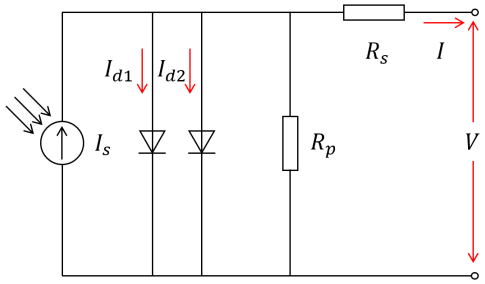

FIGURE 2.5: 2-diode PV cell model.

Based on the model, the PV cell output current I_s can be obtained in the following.

$$I = I_s N_p - \sum_{i=1}^{2} I_{di} N_p exp\left(\frac{V + \frac{N_s}{N_p} I R_S}{\alpha_1 V_{T1} N_s}\right) - \frac{V + \frac{N_s}{N_p} I R_S}{\frac{N_s}{N_p} R_p} \tag{2.4}$$

In the equation, I is the PV output current and V is the PV output voltage. R_s and R_p are the series and parallel resistance, respectively. V_T is the thermal voltage of the diodes. I_s can be obtained in Equ. 2.5. I_{d1} and I_{d2} can be obtained in Equ. 2.6.

$$I_s = \left(I_{STC} + K_1 \left(T - T_{STC}\right)\right) \frac{G}{G_{STC}} \tag{2.5}$$

In the equation, K_1 is the short circuit current coefficient. I_{STC} is the measured PV output current in the standard test condition.

$$I_{d1} = I_{d2} = \frac{I_{SC\_STC} + K_1 \left(T - T_{STC}\right)}{exp\left(\frac{V_{OC\_STC} + K_V \left(T - T_{STC}\right)}{V_T}\right) - 1} \tag{2.6}$$

In the equation, I_{SC_STC} and V_{OC_STC} are the short circuit current and the open circuit voltage under the standard test condition, respectively.

Based on the above equations, it also can be concluded that the PV cell output current changes with the solar irradiance variation under working conditions.

2.4.3 PV Panel Hot-Spot Issue under Partial Shading Conditions

Because the PV cell output is really weak and can not be employed solely, a large amount of PV cells will be firstly connected in series and parallel to obtain the PV module in Fig. 2.6, and then the PV modules will be further connected in network to get the PV panel in Fig. 2.7.

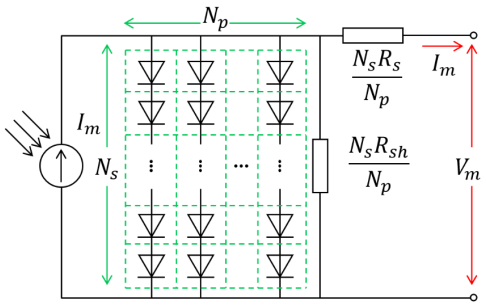

FIGURE 2.6: PV module network structure.

As shown in Fig. 2.7, when the solar irradiance of module M_1, M_2 and M_3 is uniform, the output of each branch is equal and then all the branches can output power to the outside circuit. In this case, the PV output power will possess only one peak with respect to voltage.

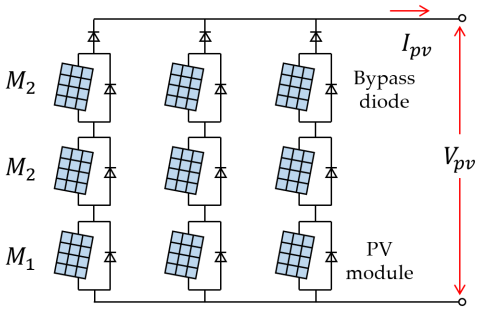

FIGURE 2.7: PV panel structure.

However, when the solar irradiance is not uniform indicating the PV panel is under partial shading conditions, for example, the module M_1 is shaded, the output of M_1 will be reduced. In this case, the PV output power curve will possess multiple peaks with respect to voltage.

For example, suppose the PV in Fig. 2.7 possesses the parameters: $V_{oc} = 37.92V$, $I_{sc} = 8.62A$, $V_{opt} = 30.96V$, $I_{opt} = 8.07A$ and $P_{max} = 250W$. When the solar irradiance of M_1, M_2 and M_3 are 1000, 1000 and 1000 respectively, the PV property is shown in Fig. 2.8. When the solar irradiance is 1000, 1000 and 600 respectively, the PV property is shown in Fig. 2.9. When the solar irradiance is 1000, 600 and 300 respectively, the PV property is shown in Fig. 2.10.

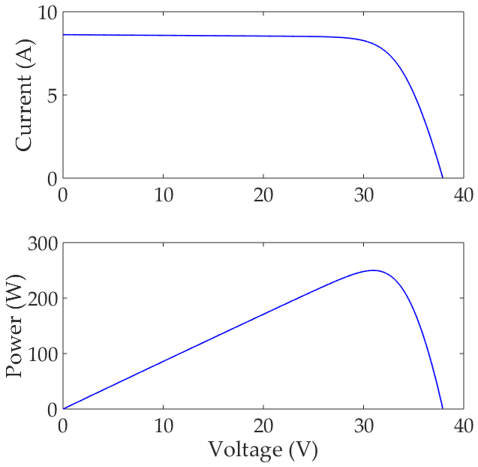

FIGURE 2.8: 1-peak PV output property.

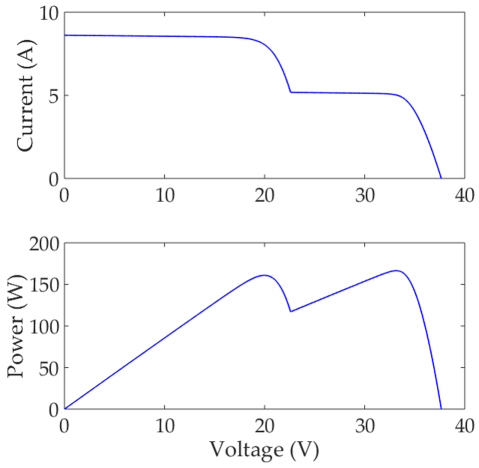

FIGURE 2.9: 2-peak PV output property.

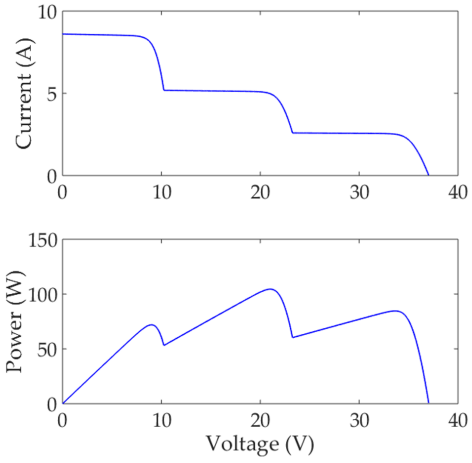

FIGURE 2.10: 3-peak PV output property.

Therefore, under working conditions, no matter the PV panel is partially shaded or not, the MPPT control should be conducted to make the most of the solar irradiance.

TABLE 2.2: Employed converter parameters.

Item	L/mH	$C_1/\mu F$	$C_2/\mu F$	f/kHz
Parameter	1	1000	1000	20

2.4.4 PV MPPT System Topology

As shown in Fig. 2.11, with the voltage and current of PV output property, the PV equivalent resistance R_{pv} can be obtained.

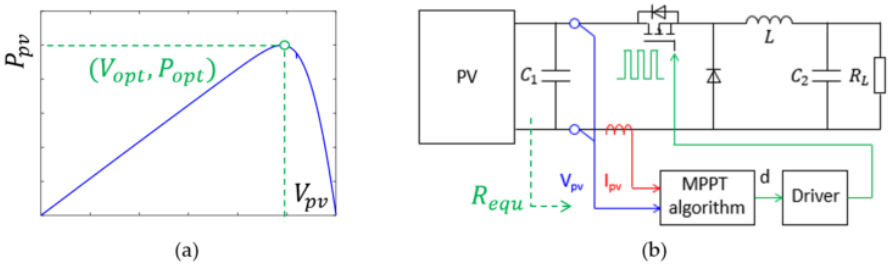

FIGURE 2.11: (a) Employed PV output property. (b) PV MPPT circuit of buck converter.

$$R_{pv} = \frac{V_{pv}}{I_{pv}} \tag{2.7}$$

Therefore, when the MPPT is achieved, the system should work at the peak point. In this case, the optimal PV equivalent resistance R_{pv_opt} will be obtained as follows.

$$R_{pv\_opt} = \frac{V_{pv\_opt}}{I_{pv\_opt}} \tag{2.8}$$

Therefore, if the outside circuit resistance is equal to R_{pv_opt}, the peak point can be approached. In other words, the MPPT control can be conducted.

In this paper, a buck converter is employed to conduct the resistance transform as shown in Fig. 2.11, and the parameters are in Tab. 2.2. The buck converter resistance transform is shown in the following.

$$R_{equ} = \frac{1}{d^2} R_L \tag{2.9}$$

In the equation, d is the converter duty. Therefore, when $R_{equ} = R_{pv\_opt}$, the MPPT control can be conducted.

2.5 Summary

In this chapter, the proposed lunar rover WPT system structure has been verified with thermal simulation. Based on the simulation results, the heat leakage caused

by the conventional wire connection has been effectively avoided at lunar night, indicating the proposed WPT system feasibility has been verified. Furthermore, the PV output property is analyzed based on the photovoltaic effect 1-diode and 2-diode models, and it is concluded that when the solar irradiance on the PV is not uniform, namely the PV works in the partial shading conditions, the PV will output multiple-peak P-V curve and in this case, the global MPPT control should be conducted to make the most of the solar energy. Furthermore, in this paper, a buck converter employed to tune the system equivalent resistance to conduct the MPPT control.

Chapter 3

Lunar Rover WPT System Topology

3.1 SS WPT Topology and Property Analysis

In this paper, because the resonance frequency is independent to the coupling factor and the circuit can be simply to be conducted, the SS topology is employed in the lunar rover WPT system and it is shown in Fig. 3.1.

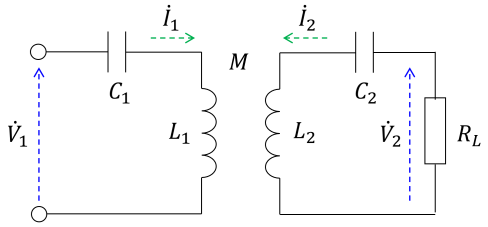

FIGURE 3.1: Employed SS topology.

Therefore, the system state equation can be obtained in the following.

$$\begin{cases} \left(R_1 + j\omega L_1 + \dfrac{1}{j\omega C_1}\right)\dot{I}_1 + j\omega M\dot{I}_2 = \dot{V}_1 \\ j\omega M\dot{I}_1 + \left(R_2 + R_{\mathrm{L}} + j\omega L_2 + \dfrac{1}{j\omega C_2}\right)\dot{I}_2 = 0 \end{cases} \tag{3.1}$$

Under working conditions, in the transmitter and receiver side circuits, the inductance and capacitance will be cancelled at the resonance frequency f.

$$f = \frac{1}{\sqrt{L_1 C_1}} = \frac{1}{\sqrt{L_2 C_2}} \tag{3.2}$$

Therefore, the following simplified state equations can be obtained.

$$\begin{cases} R_1\dot{I}_1 + j\omega M\dot{I}_2 = \dot{V}_1 \\ j\omega M\dot{I}_1 + (R_2 + R_{\mathrm{L}})\,\dot{I}_2 = 0 \end{cases} \tag{3.3}$$

Based on the simplified state equations, the circuit currents and voltages can be obtained as follows.

$$\dot{I}_1 = \frac{(R_2 + R_L)\,\dot{V}_1}{\omega^2 M^2 + R_1\,(R_2 + R_L)} \tag{3.4}$$

$$\dot{I}_2 = \frac{-j\omega M \dot{V}_1}{\omega^2 M^2 + R_1 (R_2 + R_L)} \tag{3.5}$$

Therefore, the WPT efficiency can be obtained in the following.

$$\eta_{wpt} = \frac{\omega^2 M^2 R_L}{(R_2 + R_L)(R_1 R_2 + R_1 R_L + \omega^2 M^2)} \tag{3.6}$$

Calculate the derivative of η with respect to R_L, the maximum WPT efficiency η_{wpt_max} and the optimal resistance R_{L_opt} can be obtained in the following.

$$R_{L\eta max} = \sqrt{R_2 \left(\frac{\omega^2 M^2}{R_1} + R_2 \right)} \tag{3.7}$$

$$\eta_{wpt\_max} = \frac{\omega^2 M^2 R_{L\eta max}}{(R_2 + R_{L\eta max})(R_1 R_2 + R_1 R_{L\eta max} + \omega^2 M^2)} \tag{3.8}$$

Furthermore, the WPT transferred power also can be obtained.

$$P_{wpt} = \frac{\omega^2 M^2 V_1^2}{R_1^2 R_L + \frac{(R_1 R_2 + \omega^2 M^2)^2}{R_L} + (R_1 R_2 + \omega^2 M^2) 2R_1} \tag{3.9}$$

Calculate the derivative with respect to R_L, the optimal resistance R_{LPmax} and maximum transferred power P_{wpt_max} can be obtained as follows.

$$R_{LPmax} = \frac{(\omega M)^2}{R_1} + R_2 \tag{3.10}$$

$$P_{wpt\_max} = \frac{1}{4R_1 \left(1 + \frac{R_1 R_2}{(\omega M)^2} \right)} V_1^2 \tag{3.11}$$

Therefore, under working conditions, it can be concluded that the maximum transfer efficiency and power can be approached with tuned resistance.

3.2 WPT Circuit Device Parameter Design

In this paper, the WPT system should be designed based on the lunar rover requirement. Due to the lunar rover space limit, the valid space for the coil setup is a cylinder area as shown in Fig. 3.2. With 1 cm margin, the max coil diameter is set as 13 cm and the max distance between transmitter and receiver coils is 3 cm.

In general, the ferrite materials are always employed in WPT systems because it can enhance the magnetic coupling between the coils. With stronger magnetic coupling, the power transfer can be conducted with higher magnitude, which is benifitial for the lunar rover. However, because the ferrite materials weight can not be omitted, the employment feasibility in lunar rover should be analyzed.

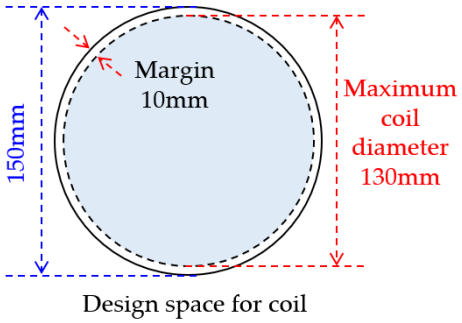

FIGURE 3.2: Lunar rover available space for WPT module.

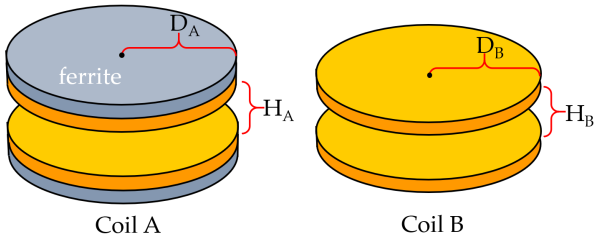

FIGURE 3.3: Employed coil structure of A and B.

3.2.1 Coil and Ferrite Module Weight Simulation and Analysis

Due to the space limit, the circular coil is employed in this paper and the coil diameter is set as D. Furthermore, in order to analyze the magnetic saturation caused by the ferrite materials, the thickness of investigated ferrite modules are set as 1 mm, 2 mm, 3 mm, 4 mm and 5 mm, respectively. The coils with/without ferrite modules are shown in Fig. 3.3. Based on the structure of coils and ferrite modules, the weight simulations of coil A and B can be obtained in Fig. 3.4.

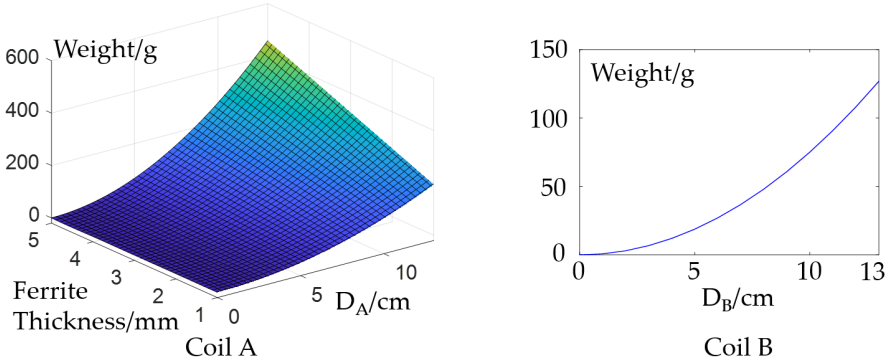

FIGURE 3.4: Weight simulation of coil A and B.

3.2.2 Coil and Ferrite Module Magnetic Simulation and Analysis

Furthermore, the investigated coil inductance is analyzed with JMAG. The ferrite on one hand can enhance the coil magnetic field, and on the other hand, the magnetic field leakage outside of the coil coupling space between the transmitter and receiver coils. Based on the JMAG simulation, the inductance of coil A and B can be obtained in Fig. 3.5.

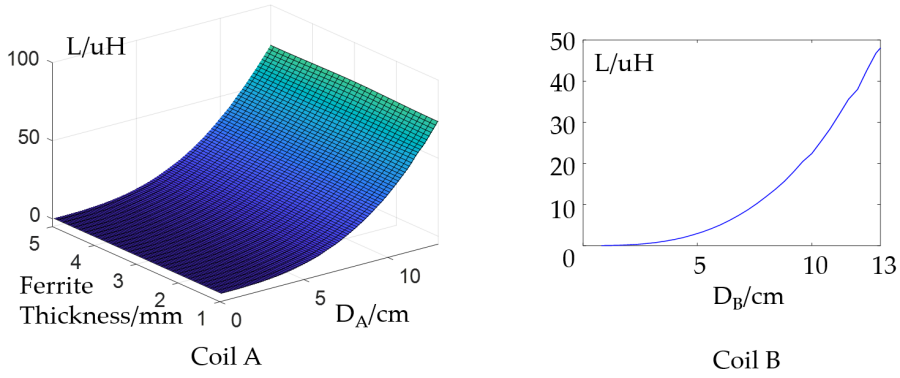

FIGURE 3.5: Inductance simulation of coil A and B.

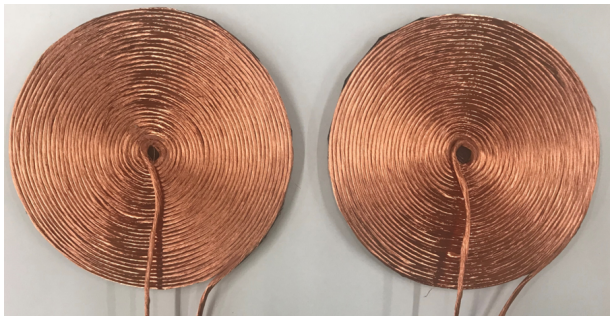

FIGURE 3.6: Manufactured coils

Because in order to obtain a strong magnetic coupling, the coil diameter is set as 13 cm, namely $D = 13cm$. Based on the weight and inductance parameters in Fig. 3.4 and 3.5, the ratio of L/w between the coil (with ferrite modules) inductance and weight is employed to assess the ferrite enhancement. In this case, the weight, inductance and ratio L/w with ferrite thickness variations can be obtained in Fig. 3.6 and Tab. 3.1.

TABLE 3.1: Ferrite enhancement property simulations.

Thickness/mm	**0**	**1**	**2**	**3**	**4**	**5**
Weight/g	125	196	260	328	393	458
$L/\mu H$	51.2	75.3	77.6	78.1	78.3	78.5
L/w	0.41	0.38	0.29	0.23	0.19	0.17

Based on Tab. 3.1, the ferrite module enhancement is saturated when the ferrite module thickness is 3 mm. Furthermore, because the ratio L/w with 1 mm thickness ferrite module is 0.38 while the ratio without ferrite materials is 0.41, the ferrite module magnetic enhancement is less than the caused weight burden. Therefore, in this paper, the coil B without ferrite modules is employed.

With the designed coil structure, the coils are manufactured in Fig. 3.7, and with coil distance variations, the coupling factor can be obtained in Fig. 3.8. Therefore, when the distance is 3 cm, the coupling factor is 0.28.

Based on the coil design, the WPT part module can be obtained and the parameters are obtained in Tab. 3.2.

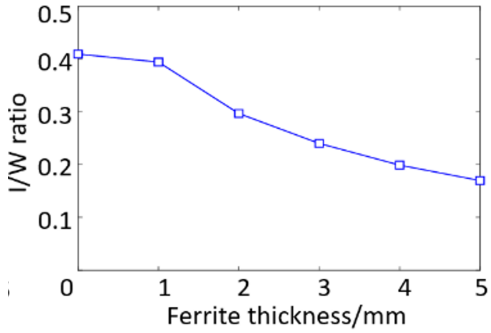

FIGURE 3.7: Ratio simulation of coil A and B.

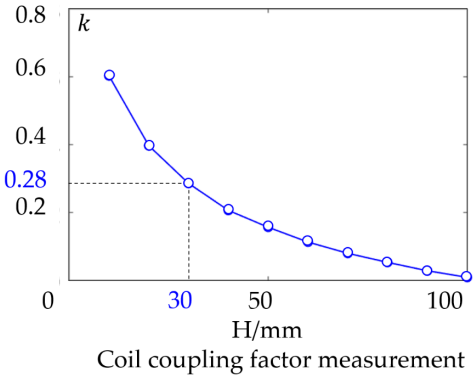

FIGURE 3.8: Coupling factor variation with distance changing.

TABLE 3.2: WPT circuit device parameters.

Symbol	Quantity	Symbol	Quantity
f/kHz	85	$R_2/m\Omega$	345.9
$R_1/m\Omega$	352.1	$L_2/\mu H$	50.2
$L_1/\mu H$	50.1	C_2/nF	71.1
C_1/nF	71.3	k	0.28
r_{wire}/mm	1	turns	32

Based on Equ. 3.7 and 3.8, with the above parameters, the maximum efficiency is $\eta_{max} = 91.11\%$ when the load meets the condition of $R_{L\eta max} = 7.42\Omega$.

3.3 Lunar Rover WPT System with Transmitter Side Converter

3.3.1 Circuit Topology and MPPT Feasibility Analysis

As analyzed in chapter. 2, the lunar rover WPT system structure is designed in Fig. 2.2. The transmitter side is placed outside of the rover body, which is connected to the PV panel. On the other hand, the receiver side is placed in the rover body, which is connected to the rover instruments. In general, the transmitter side should be powered by the inverter to transform the electricity to magnetic field, and then the inverter should be placed at the transmitter side which is outside of the rover body. As analyzed above, due to the PV output property, the MPPT control should

be conducted under working conditions. Therefore, in this section, the transmitter side converter (TC) WPT system has been proposed in Fig. 3.9 and the detailed circuit is shown in Fig. 3.10.

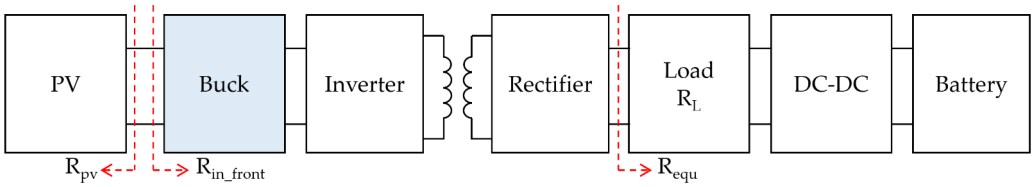

FIGURE 3.9: Proposed TC topology WPT system.

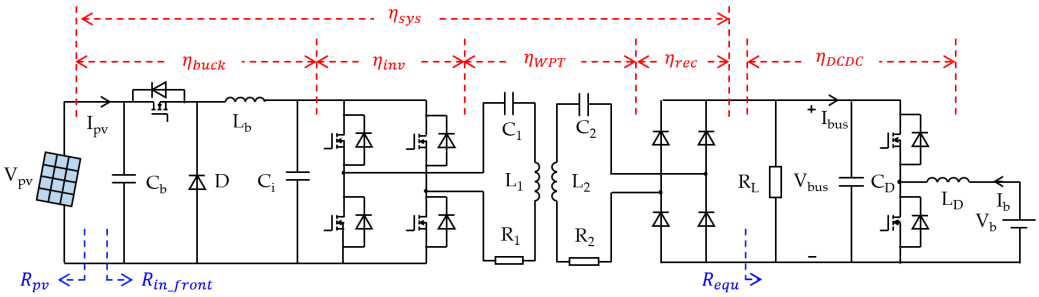

FIGURE 3.10: TC topology WPT system circuit.

Based on the Fig. 3.10, it can be concluded that: the external part mainly consists of the PV, buck converter, inverter and WPT transmitter side; the buck converter which is used to conduct the PV MPPT control is directly connected to the PV; the internal part is mainly composed of the rectifier and load.

Because the lunar rover is powered by the PV panel, the proposed TC topology MPPT feasibility is one of the most important factors determining the applicability. In chapter 2, it has been concluded that if the system equivalent resistance is equal to the optimal value the MPPT control implementation will be feasible. Based on this analysis, the system resistance transform can be obtained in the following.

$$R_{in\_front} = \frac{\pi^2}{8d^2}\left(R_1 + \frac{\omega^2 M^2}{R_2 + \frac{8}{\pi^2}R_{equ}}\right) \tag{3.12}$$

Therefore, when the system equivalent resistance R_{in_front} for TC topology is equal to the optimal value:

$$R_{pv\_opt} = R_{in\_front} \tag{3.13}$$

The system MPPT control can be achieved.

3.3.2 TC Topology MPPT Experiment Verification

Based on the topology in Fig. 3.10, the experiment platform is established in Fig. 3.11, and the system parameters are set in Tab. 3.3.

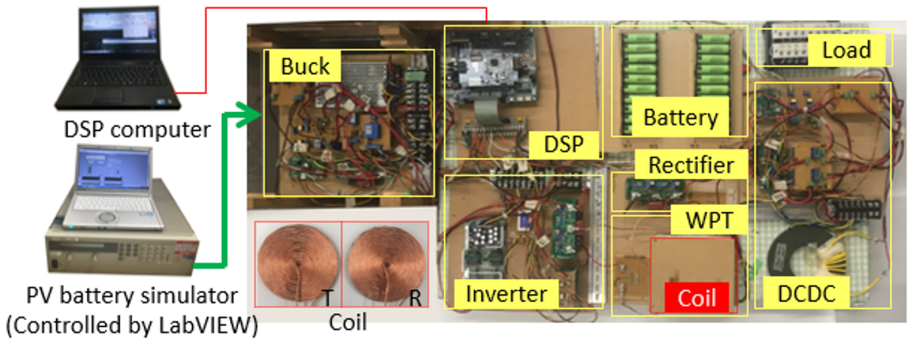

FIGURE 3.11: Established experiment platform.

TABLE 3.3: Experiment platform parameters.

Symbol	Quantity	Symbol	Quantity
$C_i/\mu F$	1000	L_D/mH	1
$C_b/\mu F$	1000	f/kHz	85
$C_D/\mu F$	1000	f_{buck}/kHz	20
L_b/mH	1	f_{DC-DC}/kHz	20

In this section, the TC topology MPPT feasibility is verified with 1-peak PV output property as shown in Fig. 3.12 and the parameters are shown in Tab. 3.4. Furthermore, the local MPPT algorithm can conduct the MPPT control. In this section, the InCon method has been employed and the parameters are set in chapter 6.

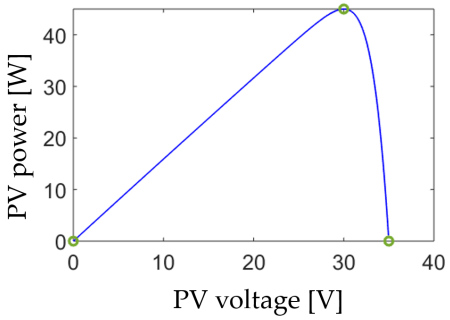

FIGURE 3.12: Employed single-peak PV output property.95

Furthermore, because there is only one peak of PV power with respect to voltage, the local MPPT algorithm can conduct the MPPT control. In this section, the InCon method has been employed and the parameters are set in chapter 6.

The MPPT experiment result is shown in Fig. 3.13. Based on the experiment results, it can be concluded that the tracking time is approximately 3 s under working conditions, and when the MPPT control is achieved, the PV output power can be stabilized at the maximum value, indicating the proposed lunar rover WPT topology and MPPT algorithm can meet the system requirements.

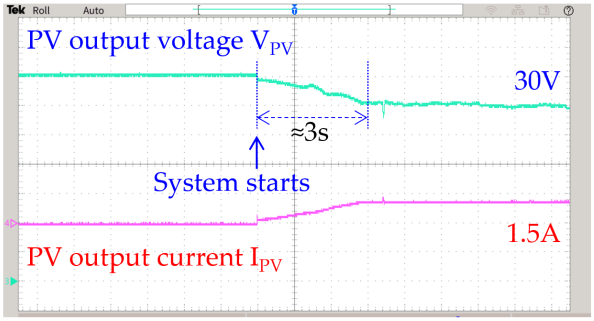

MPPT experiment

FIGURE 3.13: Employed PV property in TC topology.

TABLE 3.4: Employed 1-peak 45 W PV output property.

Item	V_{oc}/V	I_{sc}/A	V_{opt}/V	I_{opt}/A	P_{max}/W
Parameter	35	1.6	30	1.5	45

3.4 Lunar Rover WPT System with Receiver Side Converter

3.4.1 Circuit Topology and MPPT Feasibility Analysis

In the TC topology, the converter used to conduct the PV MPPT control is placed at the transmitter side, and the PV output voltage and current data can be directly to be employed by the converter. However, in this section, a lunar rover WPT system with a receiver side converter is proposed as shown in Fig. 3.14 and the detailed circuit is shown in Fig. 3.15.

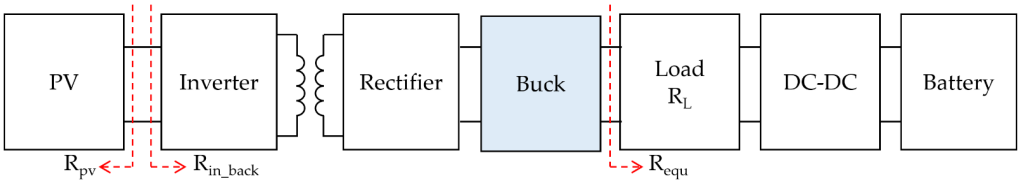

FIGURE 3.14: Proposed RC topology WPT system.

Based on Fig 3.14, it can be concluded that: the external part mainly consists of the PV, inverter and WPT transmitter side; the internal part is mainly composed of the rectifier, converter and load; the buck converter which is used to conduct the PV MPPT control is connected to the rectifier. In this paper, the receiver side converter WPT system is named as RC (receiver converter) topology.

Similar to the TC topology, when the RC topology system equivalent resistance is equal to the optimal value, the maximum power point will be approachable. Therefore, based on the circuit property, the following equations can be obtained.

$$R_{in\_back} = \frac{\pi^2}{8}\left(R_1 + \frac{\omega^2 M^2}{R_2 + \frac{8}{\pi^2 d^2} R_{equ}}\right) \tag{3.14}$$

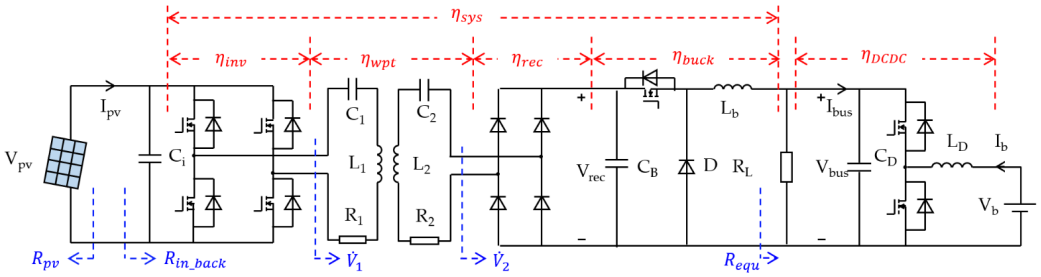

FIGURE 3.15: RC topology WPT system circuit.

Therefore, when the system equivalent resistance is equal to:

$$R_{pv\_opt} = R_{in\_back} \tag{3.15}$$

The system MPPT control can be achieved.

However, the MPPT control is conducted indirectly based on the rectifier output voltage and current data. In order to verify the MPPT feasibility, not only should the maximum power point approachability be investigated, but the system equivalent resistance monotonicity also should be focused. Therefore, based on this analysis, the system voltage can be obtained as follows.

$$\left|\dot{V}_1\right| = \frac{2\sqrt{2}}{\pi} V_{pv} \tag{3.16}$$

$$\left|\dot{V}_2\right| = \frac{2\sqrt{2}}{\pi} V_{rec} \tag{3.17}$$

$$V_{bus} = \frac{d\omega M R_L V_{pv}}{R_1 (R_2 + R_L) + \omega^2 M^2} = d_{total} V_{pv} \tag{3.18}$$

Therefore, based on Equ. 3.18, it can be concluded that the WPT module is linear part and the whole system voltage can be transformed into a total duty d_{total}, and the equivalent system is shown in Fig. 3.16. Therefore, the modules of the inverter, WPT, rectifier and converter can be regarded as a equivalent converter and then the RC topology system resistance monotonicity has been verified.

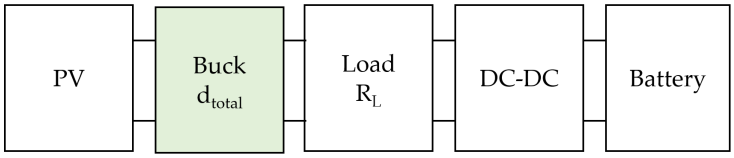

FIGURE 3.16: Equivalent RC topology WPT system.

TABLE 3.5: Employed PV output properties of 45 W, 29 W and 22 W.

Case	V_{oc}/V	I_{sc}/A	V_{opt}/V	I_{opt}/A	P_{max}
1	23.0	3.8	20.3	2.22	45
2	19.0	3.05	16.0	1.81	29
3	17.1	2.64	14.4	1.53	22

3.4.2 RC Topology MPPT Experiment Verification

In this section, the RC topology MPPT feasibility is verified with multiple-peak PV output property as shown in Fig. 3.17 and the parameters are shown in Tab. 3.5.

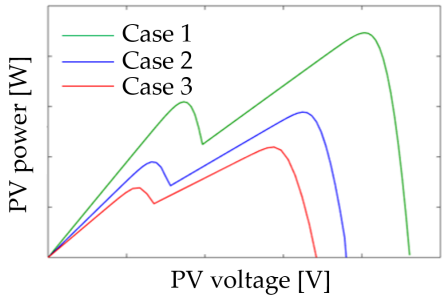

FIGURE 3.17: Employed 2-peak PV output property.

Furthermore, because there are 2 peaks of PV power with respect to voltage, the global MPPT algorithm should be conducted. In this section, the SA-PR-GPSO method has been employed and the parameters are set in chapter 6. The MPPT experiment results are shown in Fig. 3.18-20.

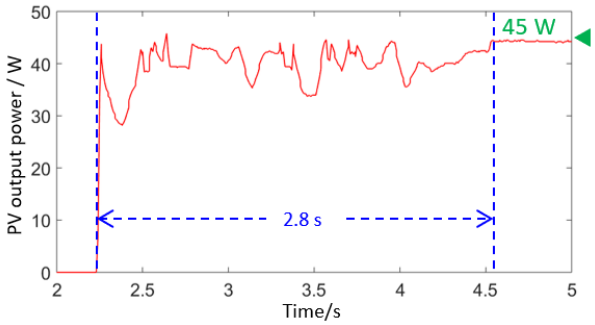

FIGURE 3.18: PV MPPT experiment of case 1.

Based on the experiment results, it can be concluded that for all the 3 cases, the global MPPT control has been achieved. The tracking time for case 1, 2 and 3 are 2.8 s, 1.8 s and 1.9 s, respectively. The reason that with higher PV output power the tracking time will be increased is that when the PV output power is increased, the flyback current flowing between the rectifer and buck converter will also be increased. The PV current I_{pv} fluctuation will be enhanced and then there will be higher error measured by the sensors input to the MPPT algorithm and then the tracking time will be increased. Furthermore, based on the lunar rover power requirement, the MPPT time upper limit is 10 s, indicating both the proposed lunar rover structure and algorithm can achieve the preset aims.

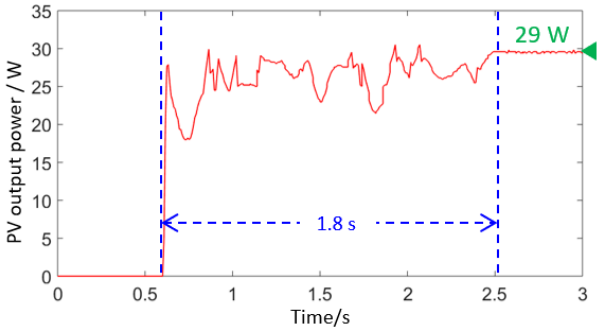

FIGURE 3.19: PV MPPT experiment of case 2.

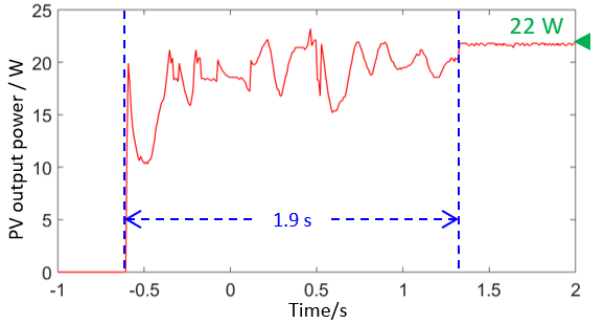

FIGURE 3.20: PV MPPT experiment of case 3.

3.5 Comparison between TC and RC WPT Topologies

In the above analysis, the TC and RC topology lunar rover WPT systems are proposed. However, because of the unique lunar circumstances, the advantages and disadvantages of the proposed two topologies are analyzed in this section.

3.5.1 TC Topology structure and working modes analysis

3.5.1.1 TC Topology Lunar Rover Structure

The proposed TC topology lunar rover structure is shown in Fig. 3.21.

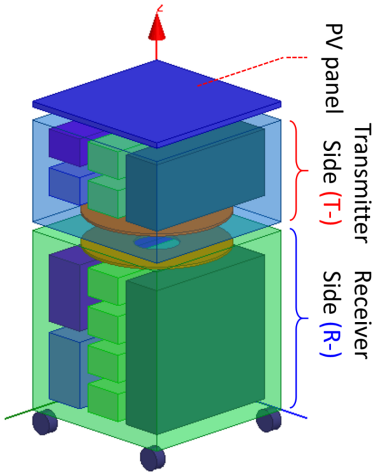

FIGURE 3.21: Lunar rover structure with TC topology WPT system.

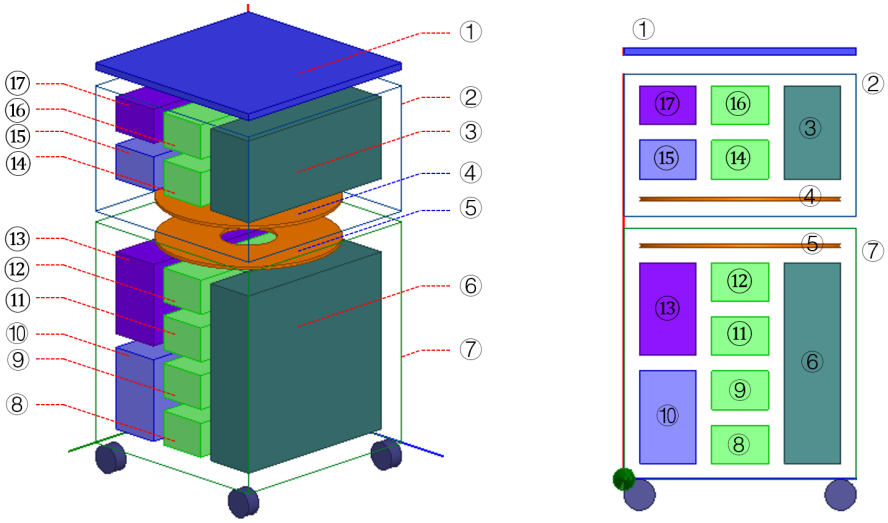

(a) (b)

FIGURE 3.22: (a) Lunar rover structure and modules. (b) Front view of lunar rover structure.

As shown in Fig. 3.22, the lunar rover with the TC topology WPT system mainly consists of three parts, namely the PV panel, transmitter side and receiver side. As shown in Fig. 3.22, in the transmitter side, the buck converter is employed to control the PV output power and the inverter is employed to transform DC to AC to power the WPT module. Because for the buck converter, no matter in the MPPT mode or buck mode, the PV output power control should be conducted in digital control, the transmitter side CPU and driver should be required. Furthermore, in order to protect the CPU, the thermal system is also required in the transmitter side.

On the other hand, in the receiver side, the rectifier is employed to transform AC to DC and both the DC-DC converter and battery are employed to balance the system power supply and requirement. Due to the required digital control in the receiver side, the CPU, driver and thermal system are required. Furthermore, because both the transmitter side and receiver side need the thermal assistance, the two parts should be covered by the thermal insulation MLI materials and then the WPT coils are also placed within the MLI cover.

Based on the above analysis, the lunar rover modules mainly include: (1) PV; (2) Transmitter side shell; (3) Thermal control system; (4) Transmitter coil; (5) Receiver coil; (6) Thermal control system; (7) Receiver side shell; (8) Battery; (9) DC-DC converter; (10) Driver; (11) Load; (12) Rectifier; (13) CPU; (14) Inverter; (15) Driver; (16) Buck converter; (17) CPU.

3.5.1.2 Working Mode Analysis at Lunar Day

At lunar day, as shown in Fig. 3.23, the generated power from PV will be transferred to the receiver side to charge the load and battery. The buck converter will control the PV in the MPPT/buck mode to output the appropriate amount power to the load and battery. As shown in Fig. 3.24, because the outside temperature is higher than 150°C, the thermal control systems will working in the cooling mode to control the temperature of transmitter and receiver side as the required 25°C room temperature, respectively. All the transmitter/ receiver side control is achieved based on the transmitter/receiver CPU, respectively. Furthermore, because the buck converter

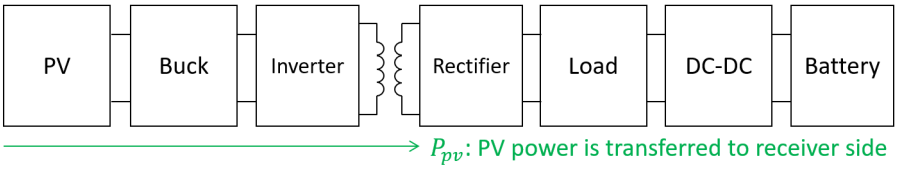

FIGURE 3.23: Power transfer direction at lunar day.

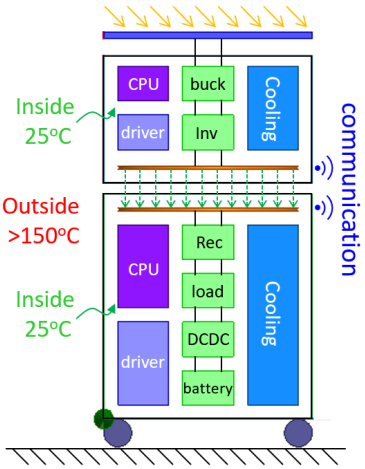

FIGURE 3.24: Lunar rover working mode analysis at lunar day.

control mode should be determined based on the PV power supply and load power requirement, the wireless communication between two sides are required at lunar day. In this way, the PV generated power can be transferred from the transmitter coil to the receiver coil via magnetic coupling. However, due to the MLI coverage, the magnetic field should penetrate two layers of MLI materials, indicating the WPT efficiency will be influenced.

3.5.1.3 Working Mode Analysis at Lunar Night

At lunar night, because there is no solar irradiance, the PV will stop working and in this mode, the battery is the only power source to drive the load as shown in Fig. 3.25. However, in order to protect the lunar rover devices, the transmitter and receiver side temperature should be controlled as the room temperature by the thermal assistance system as shown in Fig. 3.26.

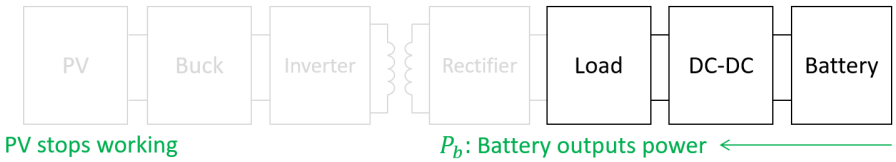

FIGURE 3.25: Power transfer direction at lunar night.

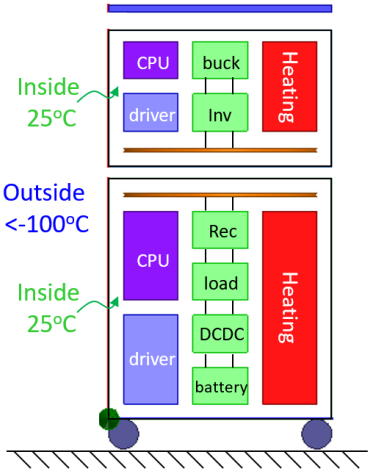

FIGURE 3.26: Lunar rover working mode analysis at lunar night.

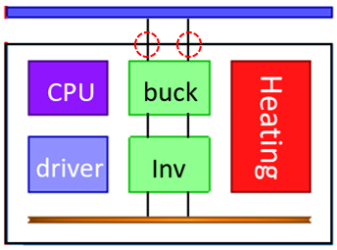

FIGURE 3.27: Heat leakage of TC topology lunar rover at lunar night.

However, as shown in Fig. 3.27, if we focus on the connection between the PV and transmitter side, the wire connection which has penetrated the MLI coverage can be found. Therefore, the slit on the transmitter side MLI coverage will cancell the proposed WPT system in the thermal insulation property.

3.5.2 RC Topology Advantage and Disadvantage Analysis

3.5.2.1 RC Topology Lunar Rover Structure

The proposed RC topology lunar rover structure is shown in Fig. 3.28.

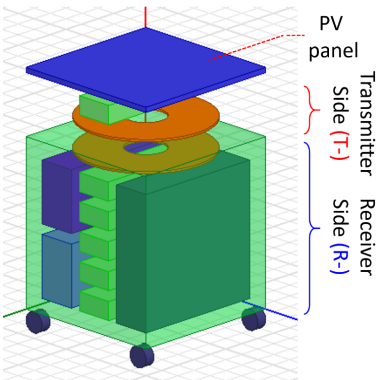

FIGURE 3.28: Lunar rover structure with RC topology WPT system.

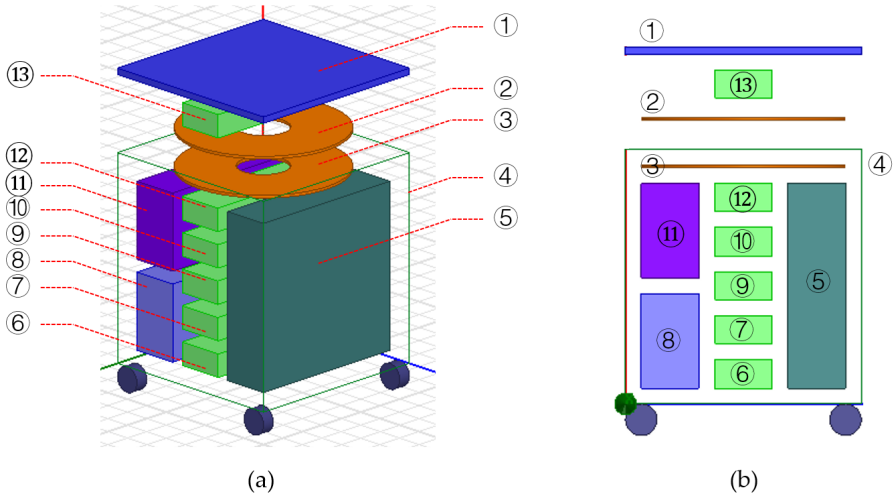

FIGURE 3.29: (a) Lunar rover structure and modules. (b) Front view of lunar rover structure.

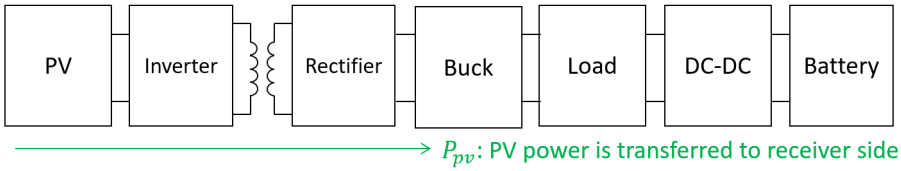

FIGURE 3.30: Power transfer direction at lunar day.

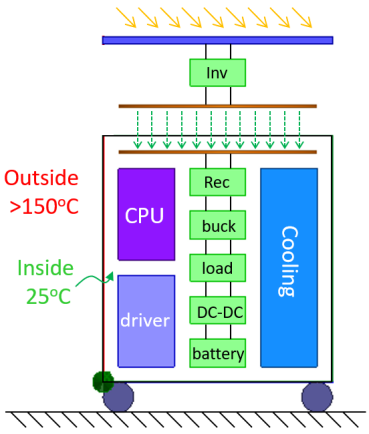

FIGURE 3.31: Lunar rover working mode analysis at lunar day.

As shown in Fig. 3.29, the lunar rover with the RC topology WPT system also mainly consists of three parts, namely the PV panel, transmitter side and receiver side. As shown in Fig. 3.29, in the transmitter side, there is only an inverter employed and it transforms DC to AC to drive the WPT module. Under working conditions, the inverter frequency is fixed at 85 kHz, and then it can be controlled in a open-loop analog way. Therefore, there is no CPU required in the transmitter side and then the other modules of driver and thermal control system can be avoided.

On the other hand, in the receiver side, the rectifier is employed to transform AC to DC and the buck converter is employed to control the PV output power. Furthermore, both the DC-DC converter and battery are employed to balance the system power supply and requirement. Due to the required digital control in the receiver

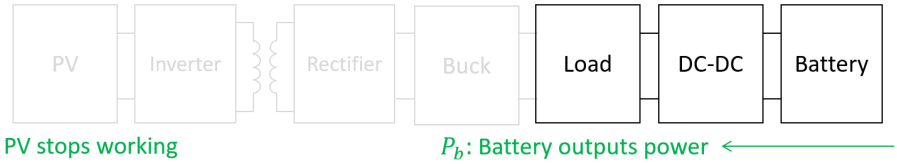

FIGURE 3.32: Power transfer direction at lunar night.

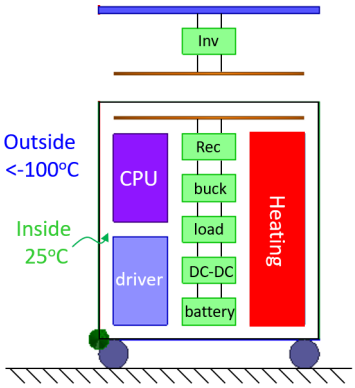

FIGURE 3.33: Lunar rover working mode analysis at lunar night.

side, the CPU, driver and thermal system are required. Because only the receiver side should be protected with thermal insulation, the only the receiver coil is placed with the MLI materials and the transmitter coil is completely exposed to the outside circumstances.

Based on the above analysis, the lunar rover modules mainly include: (1) PV; (2) Transmitter coil; (3) Receiver coil; (4) Receiver side shell; (5) Thermal control system; (6) Battery; (7) DC-DC converter; (8) Driver; (9) Load; (10) Driver; (11) CPU; (12) Rectifier; (13) Inverter.

3.5.2.2 Working Mode Analysis at Lunar Day

At luanr day, as shown in Fig. 3.30, the generated power from PV will be transferred to the receiver side to charge the load and battery. The buck converter will control the PV in the MPPT/buck mode to output the appropriate amount power to the load and battery. As shown in Fig. 3.31, because the outside temperature is higher than 150°C, the thermal control system will working in the cooling mode to control the temperature of receiver side as the required 25°C room temperature. Therefore, based on the working mode, the PV generated power can be transferred from the transmitter side to the receiver side via magnetic coupling. Because only the receiver coil is placed under the MLI coverage, it can be expected that the WPT efficiency will be less influenced compared with the TC topology WPT system.

3.5.2.3 Working Mode Analysis at Lunar Night

At lunar night, because there is no solar irradiance, the PV will stop working and in this mode, the battery is the only power source to drive the load as shown in Fig. 3.32. However, in order to protect the lunar rover devices, the receiver side temperature should be controlled as the room temperature by the thermal assistance system as shown in Fig. 3.33.

TABLE 3.6: Expected to be exploed JAXA R 2SK4048 parameters.

V_{DS}/V	I_D/A	$I_{D(pulse)}$/A	V_{GS}/V	$P_{D\|T_c=25^\circ C}$/W	T_{stg}/°C	$R_{th(ch-c)}$/°CW^{-1}
100	42	168	±20	250	(-55,150)	0.5

3.5.2.4 Comparison between TC and RC Topologies

As analyzed above, in the TC topology lunar rover structure, both the transmitter side and receiver side instruments are protected by the thermal insulation MLI materials. No matter it is the lunar day or night, the internal temperature of the lunar rover transmitter and receiver sides is kepted at 25°C. However, in the RC topology lunar rover, only the receiver side is protected in with the MLI materials coverage while the transmitter side is completely exposed to the Moon surface circumstances. In this case, the inverter MOSFET should resist the extremely intense temperature variation and radioactive rays. In our research, the expected to be employed MOSFET is JAXA R 2SK4048 and the parameters are shown in Tab. 3.6

TABLE 3.7: Comparison between lunar rover TC and RC topologies.

Item	**T-Topology**	**R-Topology**
Structure		
Transmitter CPU	1	0
Transmitter Driver	1	0
Transmitter Thermal System	1	0
Transmitter Buck	1	0
Transmitter Inverter	1	1
Receiver CPU	1	1
Receiver Driver	1	1
Receiver Thermal System	1	1
Receiver Rectifier	1	1
Receiver Buck	0	1
Receiver Load	1	1
Rectifier DC-DC Converter	1	1
Rectifier Battery	1	1
At Lunar Day		
Transmitter Shell Penetration	1	0
Receiver Shell Penetration	1	1
Transmitter Side Temperature Control	1	0
Receiver Side Temperature Control	1	1
Communication	1	0
At Lunar Night		
Transmitter Side Temperature Control	1	0
Receiver Side Temperature Control	1	1
Heat Leakage	1	0

With Tab. 3.6, the MOSFET JAXA R 2SK4048 can work normally within the temperature range of (-55°C,150°C). Therefore, at lunar day, it can switch OFF/ON normally and at lunar night it will stop working.

Furthermore, based on the above analysis on the TC and RC topology lunar rover WPT systems, Tab. 3.7 can be obtained. In Tab. 3.7, 0 and 1 stand for no requirement and requirement, respectively. Compared with the TC topology lunar rover WPT system, the advantages of the RC topology can be obtained as follows.

(1) There are no requirements of CPU, driver and thermal assistance system in the transmitter side;

(2) No matter the lunar day and night, the transmitter side is completely exposed to the outside circumstances and no thermal control system is required;

(3) At lunar day, the WPT magnetic coupling only needs to penertrate one layer of MLI thermal insulation materials and in this way, the WPT efficiency will be less influenced;

(4) At lunar night, because there is no thermal assistance required in the transmitter side, there is no heat leakage caused by the wire connection;

(5) Less instruments requirement of the RC topology will reduce the whole project weight and then improve the rocket performance.

Therefore, the RC topology is more appropriate for the lunar rover under working conditions.

3.6 Summary

In chapter 3, the lunar rover WPT circuit devices are designed, and based on the WPT circuit parameters, the TC and RC topology WPT systems have been proposed. In the TC topology, the converter used to conduct the PV MPPT control is connected to the PV at the transmitter side while in the RC topology, the converter is connected to the rectifier at the receiver side. Both the TC and RC topology WPT systems are verified the MPPT control implementation feasibility with experiments. Furthermore, because the PV output data can be directly employed by the converter in the TC topology, the TC topology possesses the tracking accuracy advantage over the RC topology in theory. However, because the MPPT control should be conducted in digital way, the extra thermal management system should be added at the transmitter side in the TC topology, indicating the employment of the lunar rover WPT system will be meaningless based on the current research aims. Therefore, the RC topology is more appropriate for the lunar rover application.

Chapter 4

Lunar Rover WPT System Power Management Strategy

4.1 Lunar Rover WPT System Power Source

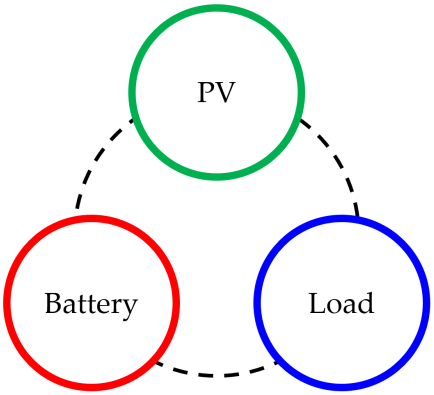

FIGURE 4.1: Employed PV, load and battery in the proposed system.

In this paper, the lunar rover WPT system mainly consists of 3 parts, and they are the PV, load and battery as shown in Fig. 4.1. In general, at lunar day, the load and battery will be powered by the PV; at lunar night, the battery will drive the thermal assistance system to protect the rover side instruments. Therefore, based on the above analysis, the battery will work as a buffer to balance the lunar rover WPT system power supply and request.

Under working conditions, the PV, battery and load will cooperate together to approach the power balance: at lunar day, on the precondition that the lunar rover should accomplish the required missions, the energy should be stored in the battery as much as possible for the upcoming lunar night; at lunar night, the battery is the sole power source to drive the thermal assistance system to keep the internal temperature at 25^{o}C. Therefore, an appropriate power management strategy can not only guarantee the required missions achieved, but also can prolong the lunar rover working life.

4.2 Power Management Strategy Design

Based on the above analysis, a 6-mode power management strategy has been proposed.

4.2.1 Mode A

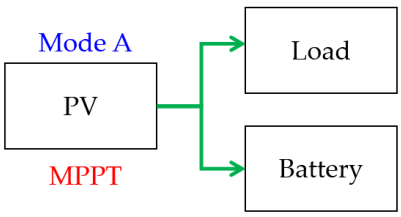

FIGURE 4.2: Mode A.

As shown in Fig. 4.2, At lunar day, when the solar irradiance is not too intense, the whole system will work in mode A. In this mode, the PV works in the MPPT mode to output the maximum power to the load and battery simultaneously. In this paper, the load works with the constant DC bus voltage under working conditions. In order to protect the battery, the battery charge current is monitored. Because the DC bus voltage is constant, when the PV output power increases, the battery charge current will be increased. In this mode, the battery charge current should be kept lower than the preset upper limit. Furthermore, in order to avoid the battery to be overcharged, the battery voltage is also monitored: when the battery voltage is higher than the upper limit, the battery will be switched off from the DC bus.

Therefore, Equ. 4.1 can be obtained.

$$\begin{cases} P_{MPPT} = P_{\text{load}} + P_{\text{battery}} \\ I_{\text{battery}} < I_{\text{limit}} \\ V_{\text{battery}} < V_{\text{limit}} \end{cases} \tag{4.1}$$

4.2.2 Mode B

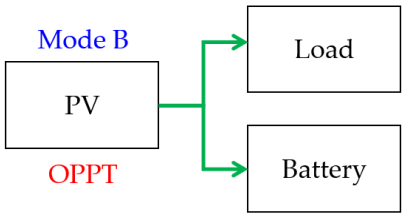

FIGURE 4.3: Mode B.

As shown in Fig. 4.3, at lunar day, when the solar irradiance is too intense, the PV output power will be excess for the receiver side because the battery charge current will exceed the upper limit. In this case, the PV should exit the MPPT mode and output the required amount power. In this paper, this PV control is called optimal power point tracking (OPPT). Therefore, in mode B, the PV works in the OPPT mode, and the battery charge current is right equal to the preset upper limit as shown in Equ. 4.2.

$$\begin{cases} P_{OPPT} = P_{\text{load}} + P_{\text{battery}} \\ I_{\text{battery}} < I_{\text{limit}} \\ V_{\text{battery}} < V_{\text{limit}} \end{cases} \tag{4.2}$$

4.2.3 Mode C

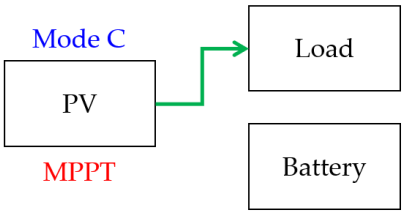

FIGURE 4.4: Mode C.

As shown in Fig. 4.4, when the battery is fully charged, it will be switched off from the DC bus to avoid the overcharge. If the solar irradiance is at the exact intensity with which the PV output power in the MPPT mode lead to the DC bus voltage to be the required constant value, the system will work in mode C in Equ. 4.3.

$$\begin{cases} P_{MPPT} = P_{\text{load}} \\ V_{\text{battery}} = V_{\text{limit}} \end{cases} \tag{4.3}$$

4.2.4 Mode D

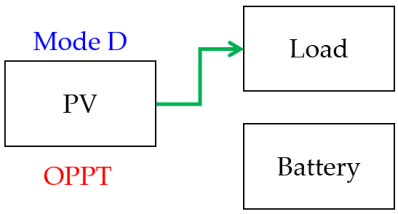

FIGURE 4.5: Mode D.

As shown in Fig. 4.5, when the battery is switched off from the DC bus and the solar irradiance is too intense, the PV should work in the OPPT mode to output appropriate amount power to stabilize the DC bus voltage to be equal to the reference in Equ. 4.4.

$$\begin{cases} P_{OPPT} = P_{\text{load}} \\ V_{\text{battery}} = V_{\text{limit}} \end{cases} \tag{4.4}$$

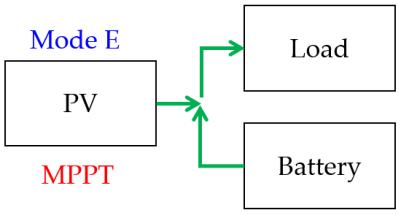

FIGURE 4.6: Mode E.

4.2.5 Mode E

As shown in Fig. 4.6, at lunar day, when the solar irradiance is not strong enough, the PV output power in the MPPT mode still can not meet the power request of load. In this case, the battery will cover the difference in Equ. 4.5. Therefore, in mode E, the PV and battery output power together to the load.

$$\begin{cases} P_{MPTT} + P_{\text{battery}} = P_{\text{load}} \\ \mathrm{I}_{battery} < I_{\text{limit}} \\ V_{\text{battery}} < V_{\text{limit}} \end{cases} \tag{4.5}$$

4.2.6 Mode F

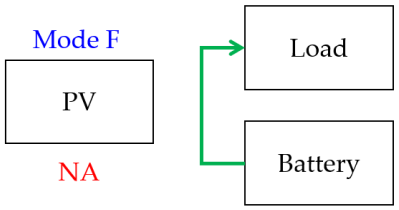

FIGURE 4.7: Mode F.

As shown in Fig. 4.7, at lunar night, the PV will stop working and the battery is the sole energy source which can output power to the load in Equ. 4.6.

$$\begin{cases} P_{\text{battery}} = P_{\text{load}} \\ I_{\text{battery}} < I_{\text{limit}} \\ V_{\text{battery}} < V_{\text{limit}} \end{cases} \tag{4.6}$$

4.3 TC Topology Power Management Control and Experiment

In the TC topology WPT system, there are several system uncertain variables, such as the PV MPPT/OPPT modes and the battery switch on/off states. All the mentioned function realizations of 6 working modes should be conducted with the converter control. Therefore, the system control structures are analyzed in the following parts.

4.3.1 System Control Structure in TC topology WPT System

4.3.1.1 When PV Works in MPPT Mode

When the PV works in MPPT mode, the system control structure is shown in Fig. 4.8.

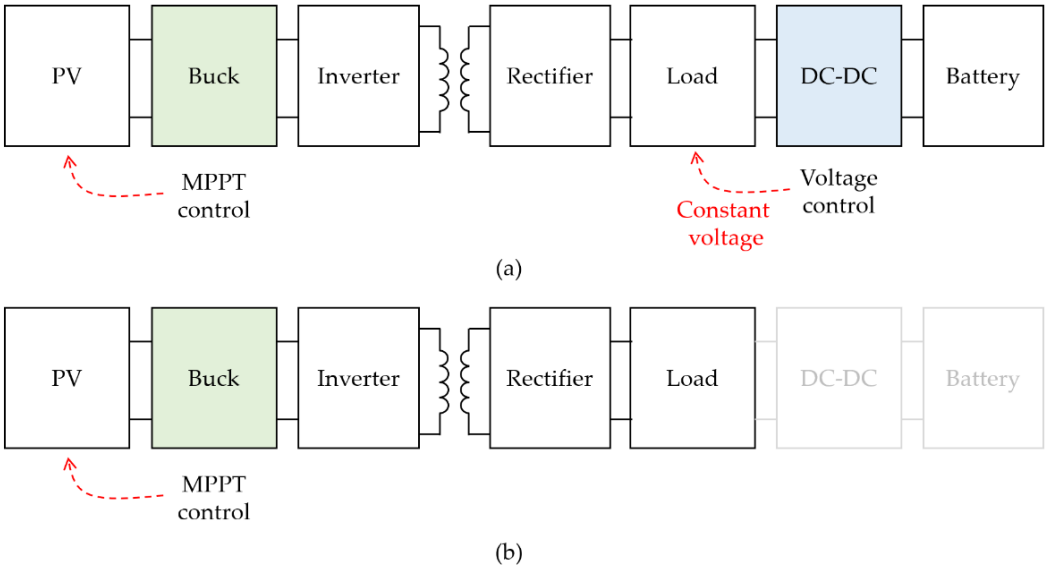

FIGURE 4.8: MPPT control method in TC topology.

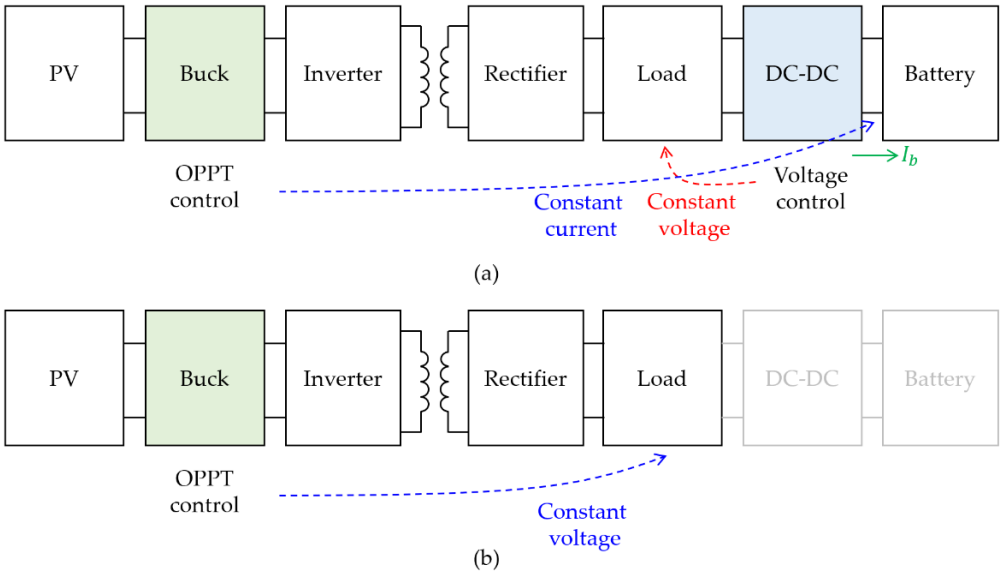

FIGURE 4.9: OPPT control method in TC topology with battery.

As shown in Fig. 4.8(a), the transmitter side converter will conduct the PV MPPT control and the receiver side DC bus voltage will be stabilized by the DC-DC converter. Therefore, the mode A and E will follow this control structure.

When the battery is fully charged and switched off from the DC bus, as shown in Fig. 4.8(b). The DC bus voltage should be stabilized with the buck converter. In this case, the solar irradiance is the exactly appropriate intensity to make the DC bus voltage to be equal to the reference. This control method is employed in mode C.

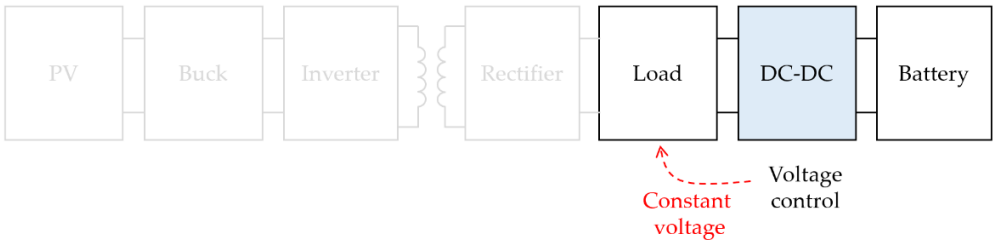

FIGURE 4.10: OPPT control method in TC topology without battery.

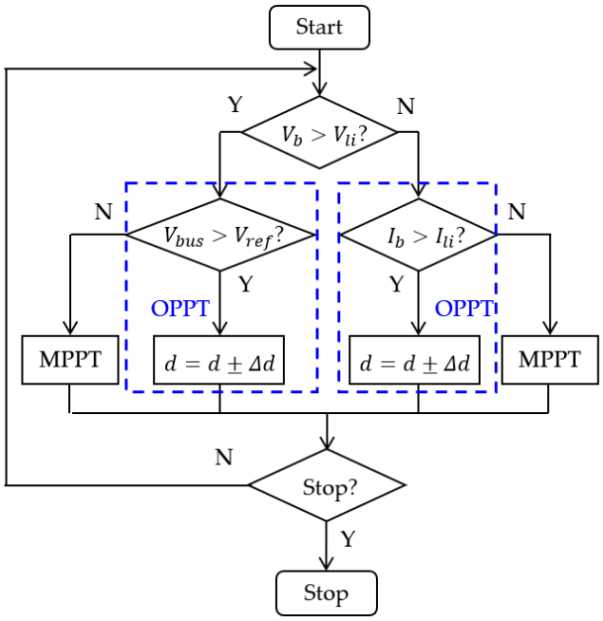

FIGURE 4.11: OPPT control flowchart.

4.3.1.2 When PV Works in OPPT Mode

When the battery is connected to the DC bus in Fig. 4.9, the DC-DC converter is still employed to stabilize the DC bus voltage, the buck converter should conduct the OPPT control to search for the appropriate duty with which the PV can output the required amount power of receiver side. In this case, the duty tracking process is controlled by the battery charge current. Therefore, this control structure is for mode B.

When the battery is switched off, the buck converter will conduct the PV OPPT control but the duty tracking process is conducted based on the DC bus voltage, and this control structure is for mode D.

4.3.1.3 When PV Stops Working

As shown in Fig. 4.10, at lunar night, the PV stops working and in this case, the battery is the only power source to the lunar.

4.3.2 OPPT Control in TC Topology

In the OPPT control, the PV output power should be controlled as the required amount to stabilize the battery charge current or DC bus voltage. In the TC topology, because no matter the battery charge current nor the DC bus voltage can not be

directly controlled by the transmitter side buck converter. Therefore, inspired by the MPPT mode, in this paper the OPPT control is also conducted with a duty tracking process. The OPPT control flowchart is shown in Fig. 4.11.

In Fig. 4.11, the MPPT control is required in system mode A, C and E. In mode B, the battery charge current should be controlled as the preset upper limit. Therefore, in Fig. 4.11, the right side OPPT control block should be employed. In mode D, similarly, the DC bus voltage is the key factor which determines the working point of the buck converter, and then the left side OPPT block should be employed.

4.3.3 Working Mode Switching with Solar Irradiance Variation

When the solar irradiance changes under working conditions, the buck converter working point should be traversed at the PV power curve to switch the PV MPPT/OPPT control. The traversal process of mode switching is analyzed in the following.

4.3.3.1 When Solar Irradiance Increases

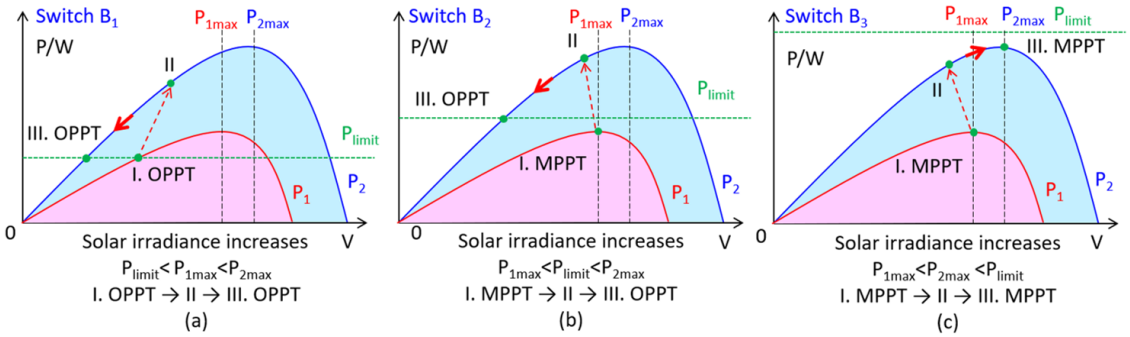

FIGURE 4.12: Working point movement when solar irradiance increases.

In Fig. 4.12(a), in the initial state, the system works at the position I under the OPPT control. When the solar irradiance increases, because the converter duty can not be changed abruptly, the system working point will be moved to the position II. Because at position II the PV output power is higher than the required amount, the system working point should move downside to search for the appropriate position. Therefore, with enough steps, the system working point will be moved to the position III under the OPPT control.

In Fig. 4.12(b), in the initial state, the system works at the position I in the MPPT mode. When the solar irradiance increases, the system working point will be moved to the position II. Because at position II the PV output power is higher than the required amount, with enough steps, the system working point will be moved to the position III under the OPPT control.

In Fig. 4.12(c), in the initial state, the system works at the position I in the MPPT mode. When the solar irradiance increases, the system working point will be moved to the position II. Because at position II the PV output power is lower than the required amount, the system working point should move upside to search for the appropriate position. Therefore, with enough steps, the system working point will be moved to the position III under the MPPT control.

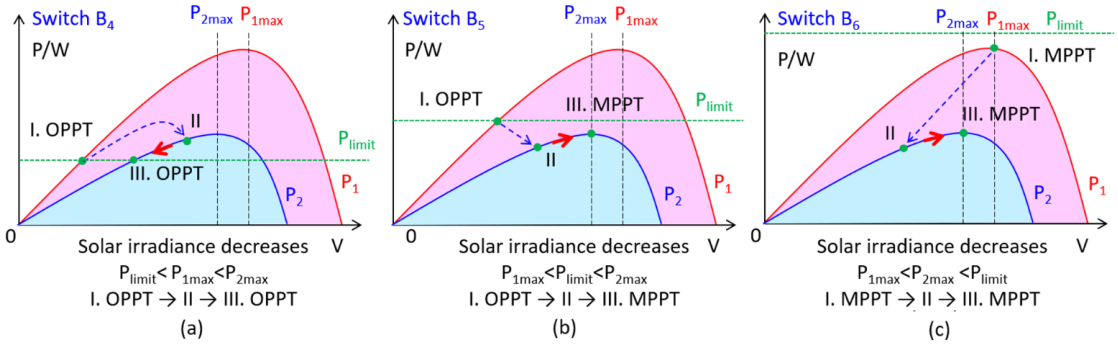

FIGURE 4.13: Working point movement when solar irradiance decreases.

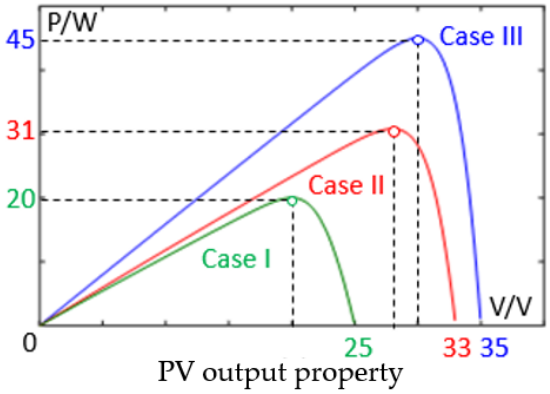

FIGURE 4.14: Employed PV output properties.

4.3.3.2 When Solar Irradiance Decreases

In Fig. 4.13(a), in the initial state, the system works at the position I under the OPPT control. When the solar irradiance decreases, because the converter duty can not be changed abruptly, the system working point will be moved to the position II. Because at position II the PV output power is higher than the required amount, the system working point should move downside to search for the appropriate position. Therefore, with enough steps, the system working point will be moved to the position III under the OPPT control.

In Fig. 4.13(b), in the initial state, the system works at the position I under the OPPT control. When the solar irradiance decreases, the system working point will be moved to the position II. Because at position II the PV output power is lower than the required amount, the system working point should move upside to search for the appropriate position. Therefore, with enough steps, the system working point will be moved to the position III under the MPPT control.

In Fig. 4.13(c), in the initial state, the system works at the position I under the MPPT control. When the solar irradiance decreases, the system working point will be moved to the position II. Because at position II the PV output power is lower than the required amount, with enough steps, the system working point will be moved to the position III under the MPPT control.

4.3.4 DC-DC Converter Controller Design

In the proposed lunar rover WPT system, the battery is employed to balance the system power supply and requirement, and the power flow is controlled by the DC-DC converter. The employed DC-DC convereter is shown in Fig. 4.15.

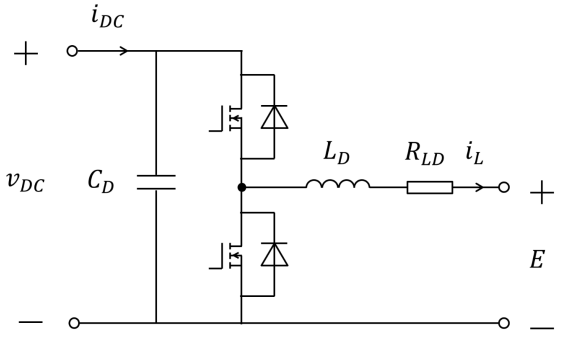

FIGURE 4.15: DC-DC topology.

With the DC-DC converter topology, the space state equations can be obtained.

$$\begin{cases} \dot{x}(t) = \mathbf{A}x(t) + \mathbf{B}u(t) \\ y(t) = \mathbf{C}x(t) + \mathbf{D}u(t) \end{cases} \tag{4.7}$$

In the equation, the following equations can be obtained.

$$x(t) = \begin{bmatrix} i_L(t) \\ v_{dc}(t) \end{bmatrix} \qquad u(t) = \begin{bmatrix} E \\ \overline{i_{dc}}(t) \end{bmatrix} \qquad y(t) = v_{dc}(t) \tag{4.8}$$

$$\mathbf{A} = \begin{bmatrix} -\dfrac{R_{LD}}{L_D} & \dfrac{d(t)}{L_D} \\ -\dfrac{d(t)}{C_D} & 0 \end{bmatrix} \qquad \mathbf{B} = \begin{bmatrix} -\dfrac{1}{L_D} & 0 \\ 0 & \dfrac{1}{C_D} \end{bmatrix} \qquad \mathbf{C} = \begin{bmatrix} 0 & 1 \end{bmatrix} \tag{4.9}$$

Expand the above model at the system working point, $d(t)$, $i_L(t)$, $v_{dc}(t)$ and $\overline{i_{dc}}(t)$ can be expressed as follows.

$$d(t) = D + \Delta d(t) \qquad i_L(t) = I_L + \Delta i_L(t) \tag{4.10}$$

$$v_{dc}(t) = V_{dc} + \Delta v_{dc} \qquad \overline{i_{dc}}(t) = I_{dc} + \Delta\overline{i_{dc}}(t) \tag{4.11}$$

$$x(t) = X + \Delta x(t) \qquad X = \begin{bmatrix} I_L \\ V_{dc} \end{bmatrix} \qquad \Delta x(t) = \begin{bmatrix} \Delta i_L(t) \\ \Delta v_{dc}(t) \end{bmatrix} \tag{4.12}$$

$$u(t) = U + \Delta u(t) \qquad U = \begin{bmatrix} D \\ \overline{I_{dc}} \end{bmatrix} \qquad \Delta u(t) = \begin{bmatrix} \Delta d(t) \\ \Delta\overline{i_{dc}}(t) \end{bmatrix} \tag{4.13}$$

With the expansion, the following equations can be obtained.

$$\Delta\dot{x}(t) = \Delta\mathbf{A}\Delta x(t) + \Delta\mathbf{B}\Delta u(t) \tag{4.14}$$

$$\Delta v_{dc}(t) = \mathbf{C}\Delta x\,(t) \tag{4.15}$$

$$\Delta\mathbf{A} = \begin{bmatrix} -\dfrac{R_{LD}}{L_D} & \dfrac{D}{L_D} \\ -\dfrac{D}{C} & 0 \end{bmatrix} \qquad \Delta\mathbf{B} = \begin{bmatrix} \dfrac{V_{dc}}{L} & 0 \\ -\dfrac{I_L}{C} & \dfrac{1}{C} \end{bmatrix} \tag{4.16}$$

Based on the DC-DC converter topology, in the steady state, the following equation can be obtained.

$$V_{dc} = \frac{ED + R_D\overline{I_{dc}}}{D^2} \qquad I_L = \frac{\overline{I_{dc}}}{D} \tag{4.17}$$

Furthermore, the following can be obtained.

$$\overline{I_{dc}} = \frac{8}{\pi^2}\frac{\omega_0 k\sqrt{L_1L_2}V_s - R_1V_{dc}}{R_1R_2 + \omega_0^2k^2L_1L_2} \tag{4.18}$$

Therefore, $\Delta\mathbf{A}$ and $\Delta\mathbf{B}$ can be transformed into the following equations.

$$\Delta\mathbf{A} = \begin{bmatrix} -\dfrac{R_D}{L_D} & \dfrac{D}{L_D} \\ -\dfrac{D}{C_D} & -\dfrac{8}{\pi^2}\dfrac{R_1}{C\left[R_1R_2 + \omega_0^2k^2L_1L_2\right]} \end{bmatrix} \qquad \Delta\mathbf{B} = \begin{bmatrix} \dfrac{V_{dc}}{L_D} \\ -\dfrac{I_L}{C_D} \end{bmatrix} \tag{4.19}$$

$$\Delta x(t) = \begin{bmatrix} \Delta i_L(t) \\ \Delta v_{dc}(t) \end{bmatrix} \qquad \Delta u(t) = \Delta d(t) \tag{4.20}$$

Based on Equ. 4.17 and 18, the following equation can be obtained.

$$D = \frac{E + \sqrt{E^2 - 4R_DV_{dc\eta max}\overline{I_{dc}}\,|\,V_{dc} = V_{dc\eta max}}}{2V_{dc\eta max}} \tag{4.21}$$

In Equ. 4.21, $D \in (0, 1)$.

Therefore, the PID controller as shown in Fig. 4.16 can be obtained based on the pole placement method.

The transfer function P can be obtained as follows.

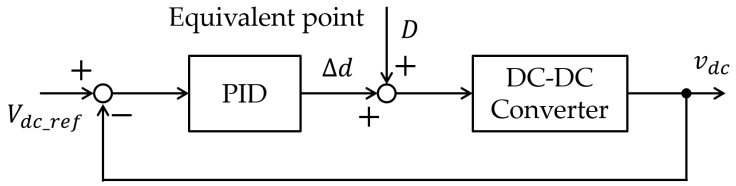

FIGURE 4.16: Employed PID controller.

$$P = \frac{\Delta d_{dc}}{\Delta d} = \frac{b_1 s + b_0}{s^2 + a_1 s + a_0} \tag{4.22}$$

In Equ. 4.22, the following equations can be obtained.

$$a_1 = \frac{R_D}{L_D} + \frac{8}{\pi^2} \frac{R_1}{C_D \left(R_1 R_2 + \omega_0^2 k^2 L_1 L_2\right)} \tag{4.23}$$

$$a_0 = \frac{1}{L_D C_D} \left(D^2 + \frac{8}{\pi^2} \frac{R_D R_1}{R_1 R_2 + \omega_0^2 k^2 L_1 L_2} \right) \tag{4.24}$$

$$b_1 = -\frac{I_L}{C_D} \tag{4.25}$$

$$b_0 = -\frac{R_D I_L + D V_{dc}}{L_D C_D} \tag{4.26}$$

With the above plant P, the PID controller can be obtained based on the pole placement method.

$$C_{pid} = K_P + \frac{K_I}{s} + \frac{K_D s}{\tau s + 1} \tag{4.27}$$

4.3.5 Experiment verification

In order to verify the proposed power management strategy, 3 cases of PV output property are employed in Fig. 4.14 and Tab. 4.1. When the PV output property changes, the system working mode should be switched automatically. Furthermore, the DC bus refence voltage and battery voltage are $V_{bus\_ref} = 15V$ and $V_{battery} = 10V$.

4.3.5.1 Experiment Results of Mode A

In mode A, PV should work under the MPPT control to charge the battery and load in case 1. The battery charge current upper limit is $I_{upper} = -2A$. The experiment result is shown in Fig. 4.17. The PV working point is controlled at the optimal position, namely $V_{pv} = 30V$, indicating the MPPT control is achieved. The DC bus voltage is controlled as the reference, namely $V_{bus} = 15V$, and the battery is charged at the current of $I_{battery} = -1A$.

TABLE 4.1: Employed PV output properties of 45 W, 31 W and 20 W.

Case	V_{oc}/V	I_{sc}/A	V_{opt}/V	I_{opt}/A	P_{max}
1	35	1.6	30	1.5	45
2	33	1.2	28	1.1	31
3	25	1.1	20	1.0	20

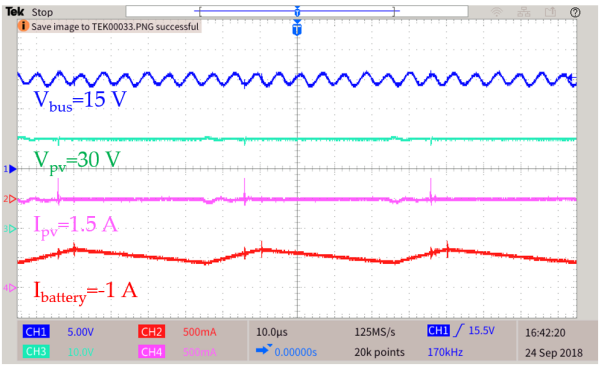

FIGURE 4.17: Experiment result of mode A.

4.3.5.2 Experiment Results of Mode B

In mode B, PV should work under the OPPT control to charge the battery and load in case 1. The battery charge current upper limit is $I_{upper} = -0.5A$. The experiment result is shown in Fig. 4.18. The PV working point is controlled at the optimal position, namely $V_{pv} = 32V$, indicating the OPPT control is achieved. The DC bus voltage is controlled as the reference, namely $V_{bus} = 15V$, and the battery is charged at the current of $I_{battery} = -0.5A$.

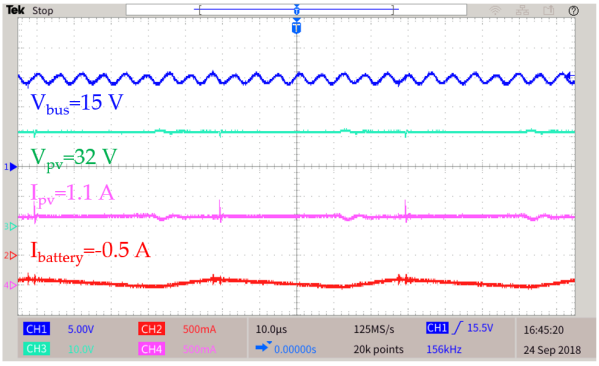

FIGURE 4.18: Experiment result of mode B.

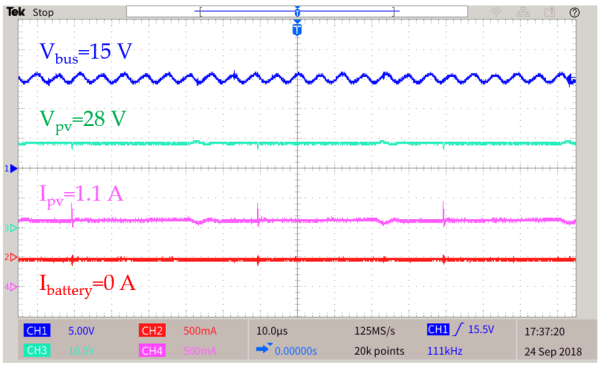

FIGURE 4.19: Experiment result of mode C.

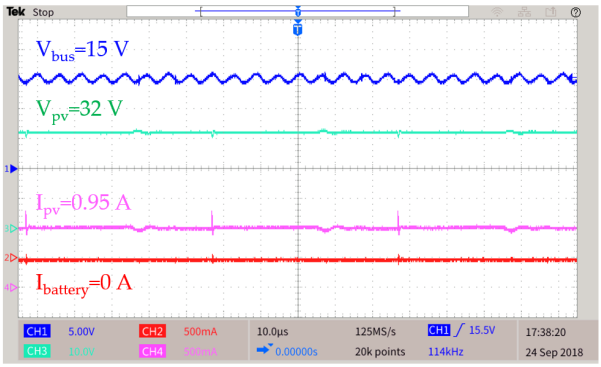

FIGURE 4.20: Experiment result of mode D.

4.3.5.3 Experiment Results of Mode C

In mode C, the battery is fully charged and is switched off from the DC bus. The PV should work under the MPPT control to power the load in case 2. The experiment result is shown in Fig. 4.19. The PV working point is controlled at the optimal position, namely $V_{pv} = 28V$, indicating the MPPT control is achieved. The DC bus voltage is controlled as the reference, namely $V_{bus} = 15V$.

4.3.5.4 Experiment Results of Mode D

In mode D, the battery is fully charged and is switched off from the DC bus. The PV should work under the OPPT control to charge the load in case 1. The experiment result is shown in Fig. 4.20. The PV working point is controlled at the optimal position, namely $V_{pv} = 32V$, indicating the OPPT control is achieved. The DC bus voltage is controlled as the reference, namely $V_{bus} = 15V$.

4.3.5.5 Experiment Results of Mode E

In mode E, the solar irradiance is not strong enough, and then the PV should work under the MPPT control to power the load in case 3 with the battery. The experiment result is shown in Fig. 4.21. The PV working point is controlled at the optimal position, namely $V_{pv} = 20V$, indicating the MPPT control is achieved. The DC bus voltage is controlled as the reference, namely $V_{bus} = 15V$. The battery discharges at the current of $I_{battery} = 0.8A$.

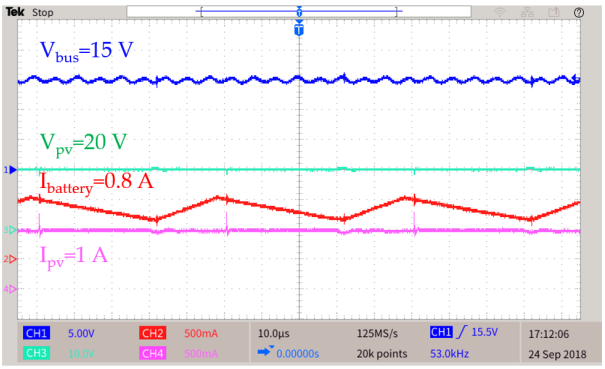

FIGURE 4.21: Experiment result of mode E.

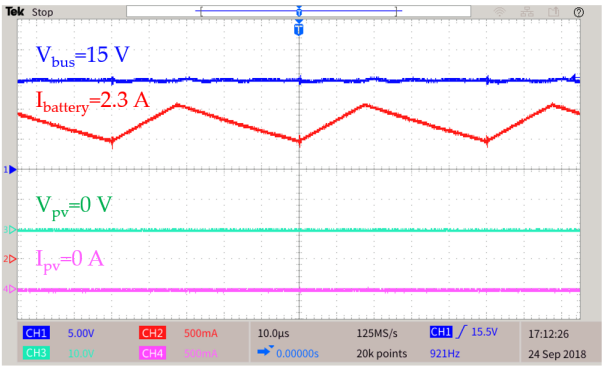

FIGURE 4.22: Experiment result of mode F.

4.3.5.6 Experiment Results of Mode F

In mode F, at lunar night the PV stops working and the only the battery outputs power to the load. The experiment result is shown in Fig. 4.22. The DC bus voltage is controlled as the reference, namely $V_{bus} = 15V$. The battery discharges at the current of $I_{battery} = 2.3A$.

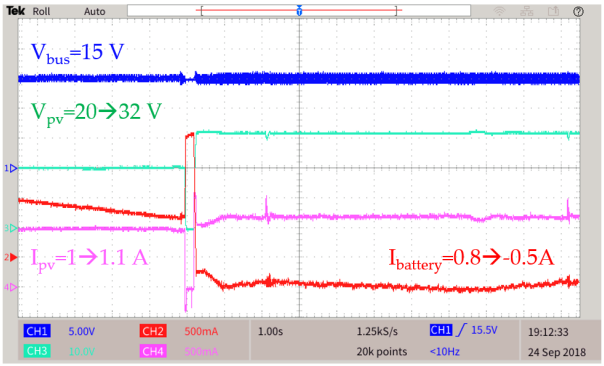

FIGURE 4.23: Experiment result of mode switch D → B.

4.3.5.7 Mode Switch: E → B

In the initial state, the solar irradiance is not strong enough in case 3 and the system works in the mode E. Furthermore, the battery charge current upper limit is $I_{upper} = -0.5A$. When the solar irradiance abruptly changes from case 3 to 1, the system

should change from mode E to B. Based on the experiment result in Fig. 4.23, the PV output voltage changes from 20 V to 32 V and the battery charge current also changes from 0.8 A to -0.5 A, respectively, indicating the mode switch is effectively achieved.

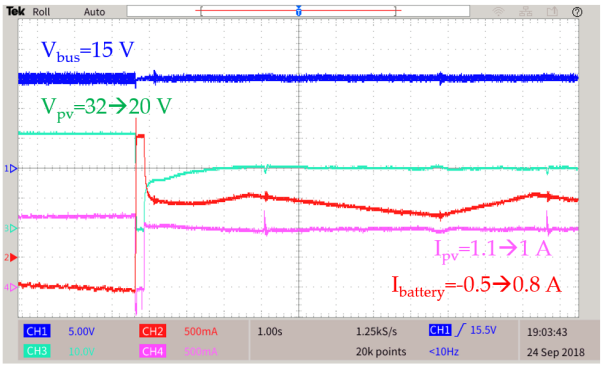

FIGURE 4.24: Experiment result of mode switch B → D.

4.3.5.8 Mode Switch: B → E

In the initial state, the solar irradiance is strong enough in case 1 and the system works in the mode B. Furthermore, the battery charge current upper limit is $I_{upper} = -0.5A$. When the solar irradiance abruptly changes from case 1 to 3, the system should change from mode B to E. Based on the experiment result in Fig. 4.24, the PV output voltage changes from 32 V to 20 V and the battery charge current also changes from -0.5 A to 0.8 A, respectively, indicating the mode switch is effectively achieved.

Furthermore, in mode A of 45 W, the system efficiency is shown in Fig. 4.25.

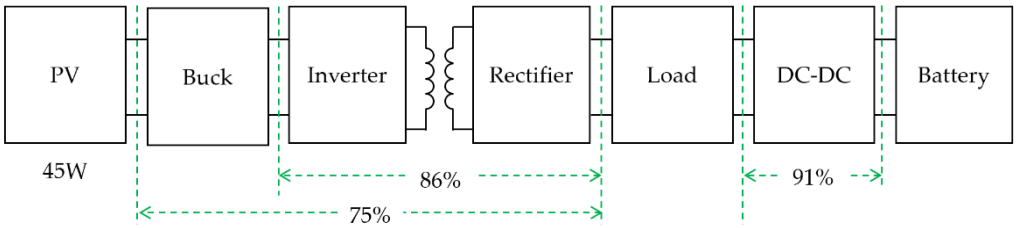

FIGURE 4.25: Flyback current at the transmitter and receiver side.

However, in the experiment results, it can be found that there is a ripple at the DC bus voltage V_{bus}. By analyzing the ripple frequency of 170 kHz, it can be conluded that the ripple is generated by the flyback current from the rectifier to the DC bus under working conditions as shown. Furthermore, with the same analysis, it also can be concluded that there is a ripple at the transmitter side caused by the flyback current from the inverter as shown in Fig. 4.26.

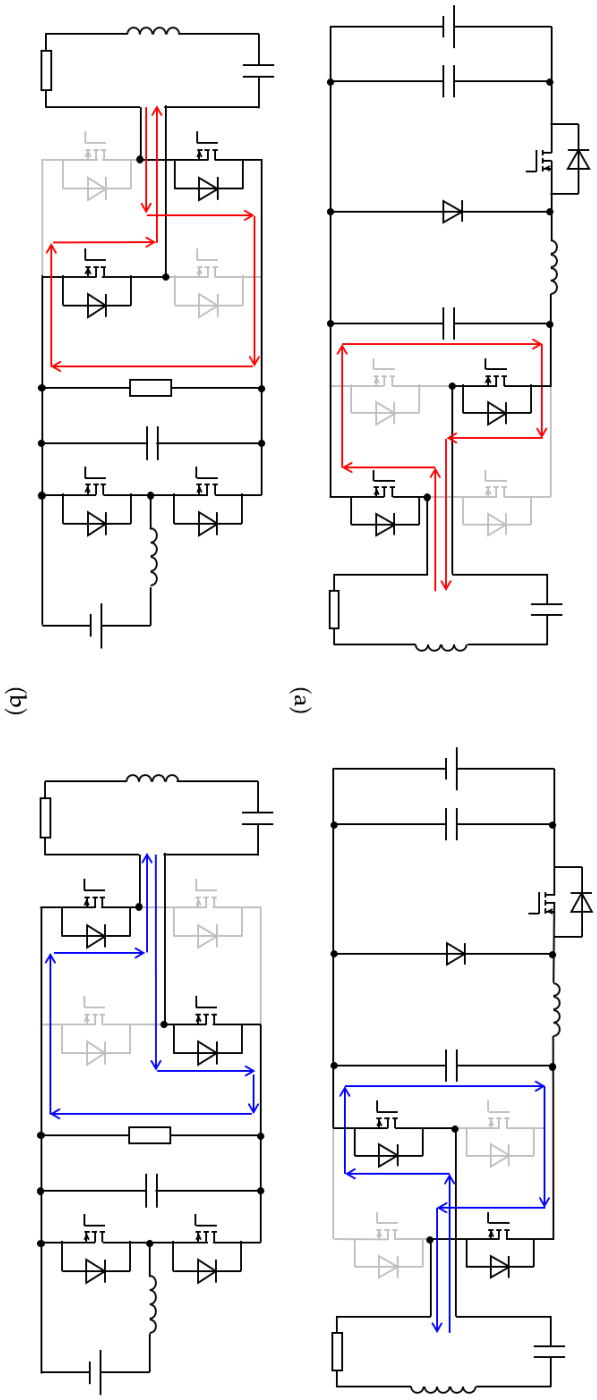

FIGURE 4.26: System efficiency in mode A

4.4 RC Topology Power Management Control and Experiment

Same to the TC topology, the system working state of RC topology is also influenced by the variables of PV MPPT/OPPT modes and battery switch on/off states. Therefore, the system control structure is analyzed in the following parts.

4.4.1 System Control Structure in RC Topology WPT System

4.4.1.1 When PV Works in MPPT Mode

When the PV works under the MPPT control, the system control structure is shown in Fig. 4.27.

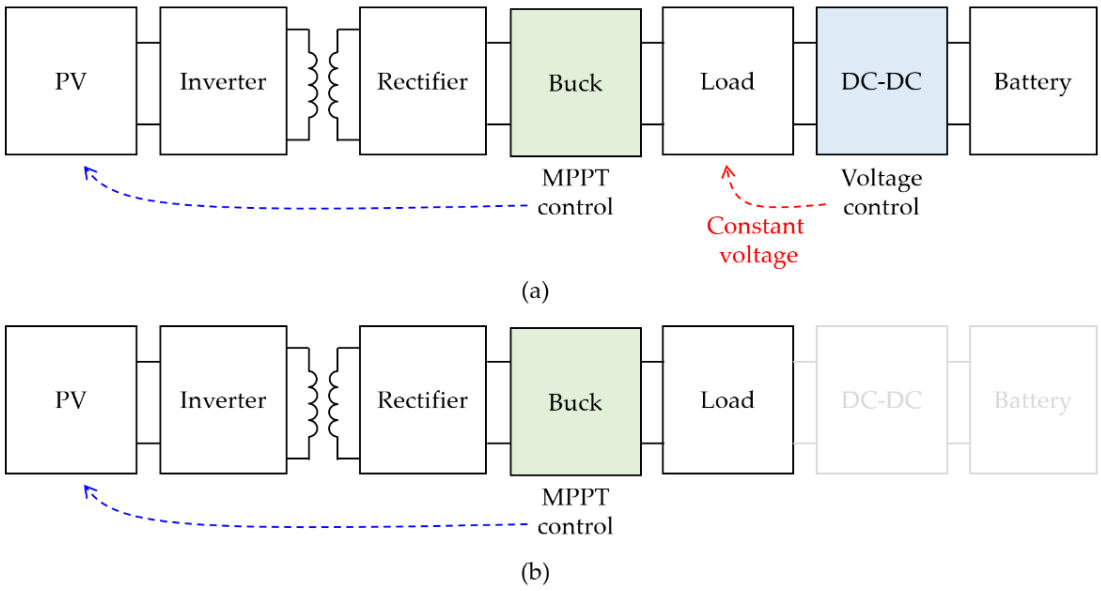

FIGURE 4.27: MPPT control method in RC topology.

The receiver side converter will conduct the PV MPPT control and the receiver side DC bus voltage will be stabilized by the DC-DC converter. Therefore, the mode A and E will follow this control structure.

When the battery is fully charged and switched off from the DC bus, as shown in Fig. The DC bus voltage should be stabilized with the buck converter. In this case, the solar irradiance is the exactly appropriate intensity to make the DC bus voltage to be equal to the reference. This control method is employed in mode C.

4.4.1.2 When PV Works in OPPT Mode

When the PV works under the OPPT control, the system control structure is shown in Fig. 4.28.

When the battery is connected to the DC bus, the DC-DC converter is employed to stabilize the battery charge current, and the buck converter should control the DC bus voltage. Therefore, this control structure is for mode B.

When the battery is switched off, the buck converter will control the DC bus voltage as shown, and this control structure is for mode D.

Because the DC bus voltage and battery charge current can be directly controlled by the buck converter and DC-DC converter respectively, the system working point can be directly determined by the converter operations. In this way, in the RC topology OPPT control, there is no working point tracking process.

4.4.1.3 When PV Stops Working

As shown in Fig. 4.29, at lunar night, the PV stops working and in this case, the battery is the only power source to the lunar.

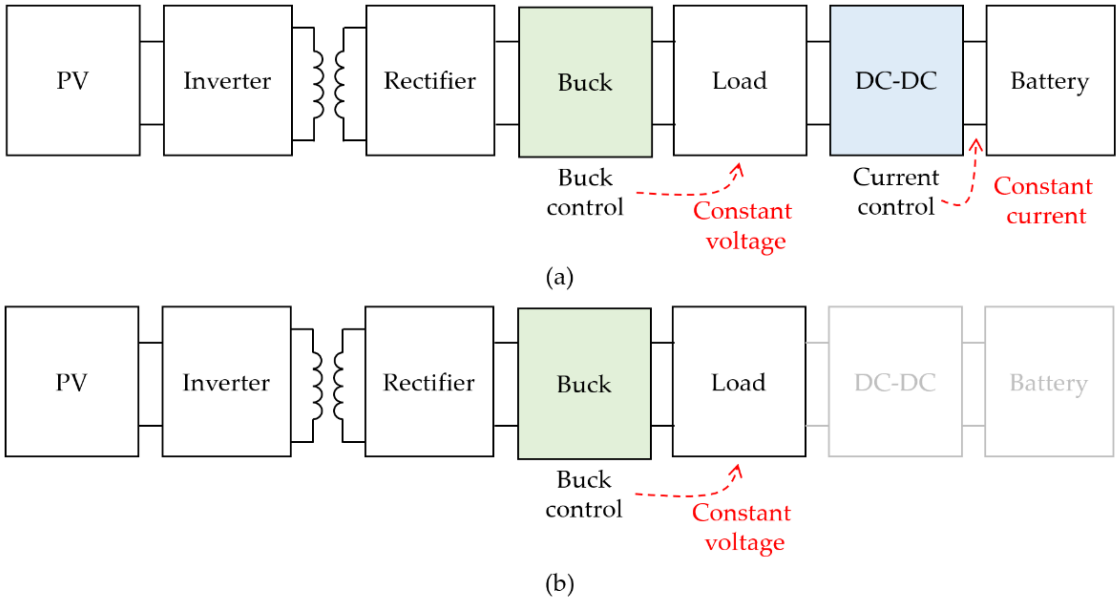

FIGURE 4.28: OPPT control method in RC topology with battery.

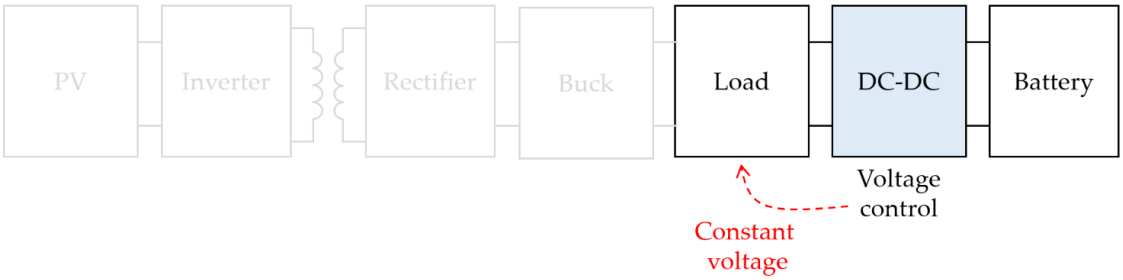

FIGURE 4.29: OPPT control method in RC topology without battery.

4.4.2 DC-DC Converter Controller Design

4.4.2.1 DC-DC Converter Transfer Function

Based on the DC-DC converter topology as shown in Fig. 4.30, the following equations can be obtained.

$$G_{v0} = \frac{v_{in}}{(1-D)^2} \tag{4.28}$$

$$\omega_{zv1} = \frac{1}{R_{CD}C_D} \tag{4.29}$$

$$\omega_{zv2} = \frac{(1-D)^2\,(R_D - R_{LD})}{L_D} \tag{4.30}$$

$$\Delta(s) = \frac{s^2}{\omega_o^2} + \frac{s}{Q\omega_o} + 1 \tag{4.31}$$

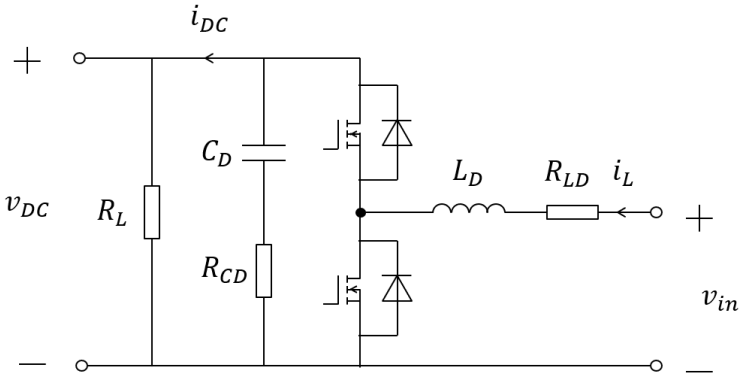

FIGURE 4.30: Employed DC-DC converter topology.

$$\omega_o = \frac{1}{\sqrt{L_D C_D}} \sqrt{\frac{R_{LD} + R_L(1-D)^2}{R_L}} \tag{4.32}$$

$$Q = \frac{\omega_o}{R_{LD}/L_D} + \frac{1}{C_D\left(R_L + R_{CD}\right)} \tag{4.33}$$

$$G_{i0} = \frac{2v_{in}}{(1-D)^3} \tag{4.34}$$

$$\omega_{zi} = \frac{1}{C_D\left(R_L/2 + R_{CD}\right)} \tag{4.35}$$

In the equation, G_{v0}, G_{i0}, R_{CD}, C_D, L_D, v_{in}, D, ω_0 and Q are the DC voltage gain, DC current gain, capacitor resistance, inductor resistance, DC bus capacitor, input voltage, steady stage duty, angular corner frequency and quality power factor, respectively.

Therefore, the DC-DC converter transfer functions can be obtained as follows.

$$G_{id}(s) = \frac{\hat{i}_L(s)}{\hat{d}(s)} = G_{i0}\frac{(1 + s/\omega_{zi})}{\Delta(s)} \tag{4.36}$$

$$G_{vd}(s) = \frac{\hat{v}_{DC}(s)}{\hat{d}(s)} = G_{v0}\frac{(1 + s/\omega_{zv1})\,(1 - s/\omega_{zv2})}{\Delta(s)} \tag{4.37}$$

If the capacitor resistance R_{CD} and inductor resistance R_{LD} can be omitted, the transfer functions can be transformed as follows.

$$G_{id}(s) = \frac{\hat{i}_L(s)}{\hat{d}(s)} = \frac{V_{in2}\left(2 + C_D R_L s\right)}{(1-D)\left[(1-D)^2 + \dfrac{L_D}{R_L}s + L_D C_D s^2\right]} \tag{4.38}$$

$$G_{vd}(s) = \frac{\hat{v}_{DC}(s)}{\hat{d}_2(s)} = V_{in2}\frac{(1-D)^2R_L - L_{Ds}}{(1-D)^2R_L + L_Ds + L_DC_Ds^2} \tag{4.39}$$

4.4.2.2 Single-loop Current Controller

When the DC-DC converter stabilizes the battery charge current I_L in Fig. 4.30, the single-loop current controller can be employed as shown in Fig. 4.31.

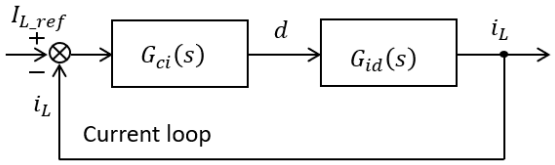

FIGURE 4.31: Employed single-loop current controller.

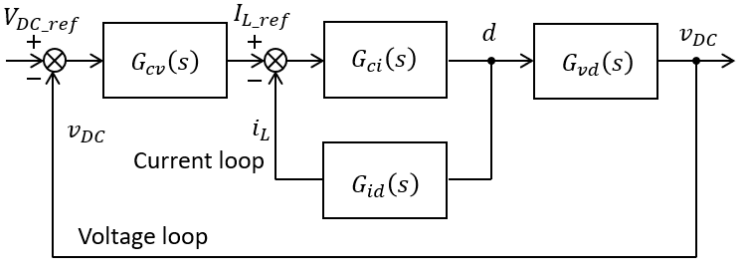

FIGURE 4.32: Employed double-loop voltage controller.

The PI controller in Equ. 4.40 should be employed.

$$G_{ci}(s) = k_{pi} + \frac{k_{ii}}{s} \tag{4.40}$$

The controller can be designed based on the required phase margin φ_{m1} and crossover frequency f_{cz1} as follows.

$$k_{pi} = \frac{\cos\theta_1}{|G_{id}(s)|} \tag{4.41}$$

$$k_{ii} = \frac{\sin\theta_1 f_{cz1}}{|G_{id}(s)|} \tag{4.42}$$

$$\theta_i = 180^\circ + \varphi_{mi} - \angle G_{id}(s) \tag{4.43}$$

In this way, the DC-DC converter single-loop current controller can be obtained.

4.4.2.3 Double-loop Voltage Controller

When the DC bus voltage is stabilized by the DC-DC converter, the double-loop voltage controller is employed as shown in Fig. 4.32.

The PI controller in Equ. 4.44 can be employed, and it also can be designed based on Equ. 4.41-43.

$$G_{cv}(s) = k_{pv} + \frac{k_{iv}}{s} \tag{4.44}$$

Therefore, in this way, the DC-DC controller current and voltage controllers can be designed.

4.4.3 Experiment Verification

In order to verify the proposed power management strategy, 3 cases of PV output property are employed in Fig. 4.33 and Tab. 3.5. When the PV output property changes, the system working mode should be switched automatically. Furthermore, the experiment parameters are set as $V_{bus\_ref} = 10V$, $R_L = 5\Omega$ and $V_{battery} = 7.2V$.

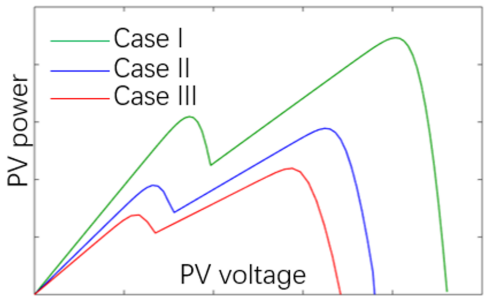

FIGURE 4.33: Employed PV output properties.

4.4.3.1 Experiment Results of Mode A

In mode A, PV should work under the MPPT control to charge the battery and load in case 1. The battery charge current upper limit is $I_{upper} = -2A$. The experiment result is shown in Fig. 4.34. The PV working point is controlled at the optimal position, namely $V_{pv} = 20.5V$, indicating the MPPT control is achieved. The DC bus voltage is controlled as the reference, namely $V_{bus} = 10V$, and the battery is charged at the current of $I_{battery} = -1.1A$.

4.4.3.2 Experiment Results of Mode B

In mode B, PV should work under the OPPT control to charge the battery and load in case 1. The battery charge current upper limit is $I_{upper} = -0.5A$. The experiment result is shown in Fig. 4.35. The PV working point is controlled at the optimal position, namely $V_{pv} = 17.5V$, indicating the OPPT control is achieved. The DC bus voltage is controlled as the reference, namely $V_{bus} = 10V$, and the battery is charged at the current of $I_{battery} = -0.5A$.

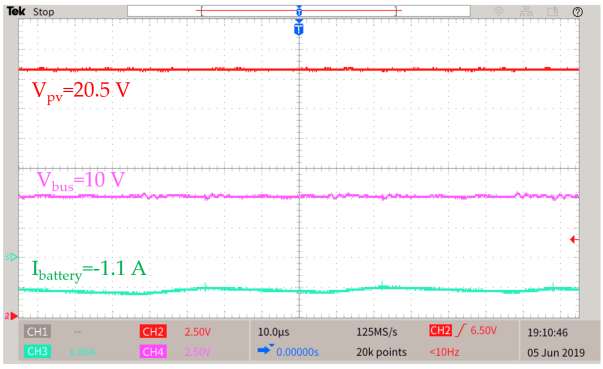

FIGURE 4.34: Experiment result of mode A.

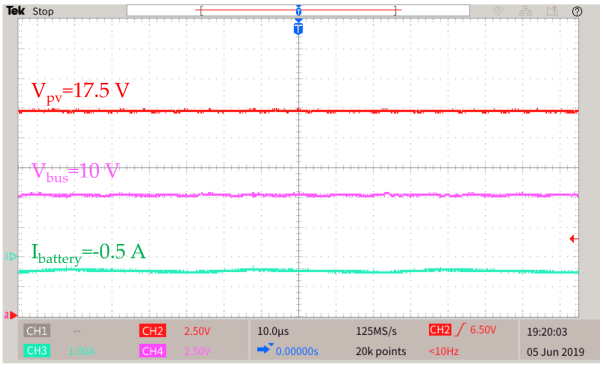

FIGURE 4.35: Experiment result of mode B.

4.4.3.3 Experiment Results of Mode C

In mode C, the battery is fully charged and is switched off from the DC bus. The PV should work under the MPPT control to power the load in case 2. The experiment result is shown in Fig. 4.36. The PV working point is controlled at the optimal position, namely $V_{pv} = 16.1V$, indicating the MPPT control is achieved. The DC bus voltage is controlled as the reference, namely $V_{bus} = 10V$.

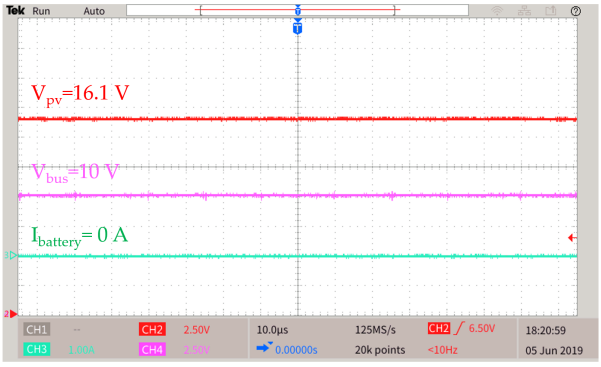

FIGURE 4.36: Experiment result of mode C.

4.4.3.4 Experiment Results of Mode D

In mode D, the battery is fully charged and is switched off from the DC bus. The PV should work under the OPPT control to power the load in case 1. The experiment

result is shown in Fig. 4.37. The PV working point is controlled at the optimal position, namely $V_{pv} = 14.9V$, indicating the OPPT control is achieved. The DC bus voltage is controlled as the reference, namely $V_{bus} = 10V$.

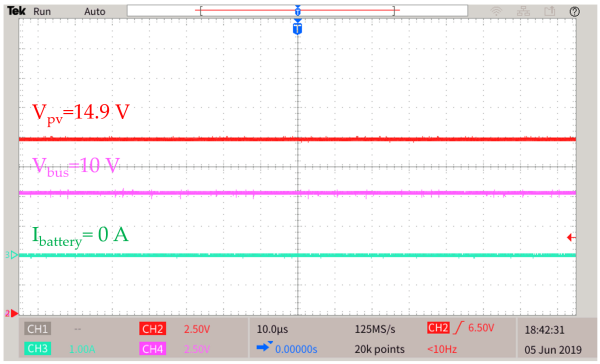

FIGURE 4.37: Experiment result of mode D.

4.4.3.5 Experiment Results of Mode E

In mode E, the solar irradiance is not strong enough, and then the PV should work under the MPPT control to power the load in case 3 with the battery. The experiment result is shown in Fig. 4.38. The PV working point is controlled at the optimal position, namely $V_{pv} = 14.8V$, indicating the MPPT control is achieved. The DC bus voltage is controlled as the reference, namely $V_{bus} = 10V$. The battery discharges at the current of $I_{battery} = 0.9A$.

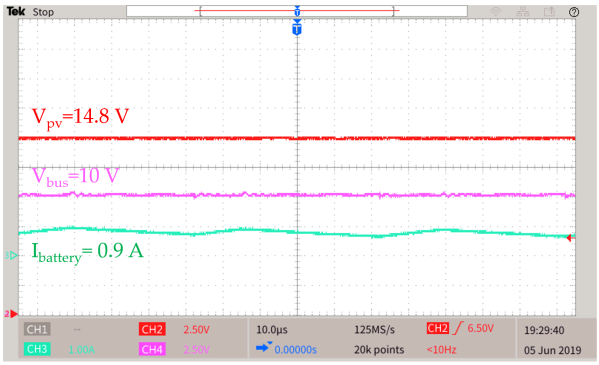

FIGURE 4.38: Experiment result of mode E.

4.4.3.6 Experiment Results of Mode F

In mode F, at lunar night the PV stops working and the only the battery outputs power to the load. The experiment result is shown in Fig. 4.39. The DC bus voltage is controlled as the reference, namely $V_{bus} = 10V$. The battery discharges at the current of $I_{battery} = 3.2A$.

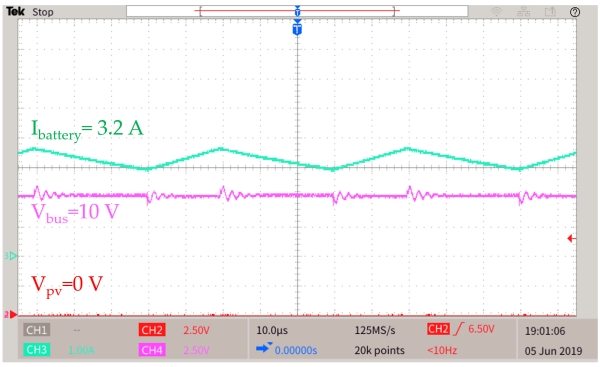

FIGURE 4.39: Experiment result of mode F.

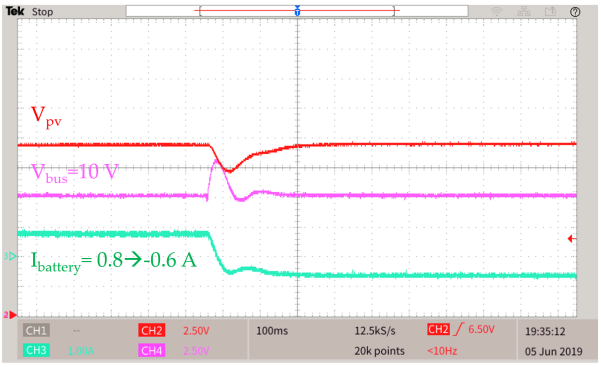

FIGURE 4.40: Experiment result of mode switch E → A.

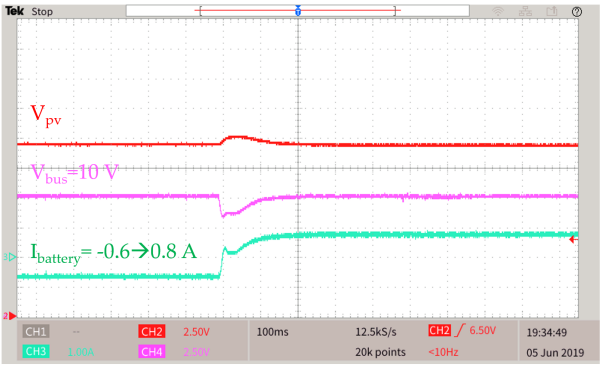

FIGURE 4.41: Experiment result of mode switch A → E.

4.4.3.7 Mode Switch: E → A

In the initial state, the load is $R_L = 5\Omega$ and the system works in the mode E. When the load R_L abruptly changes from 5Ω to 10Ω, the system encounters a brief transient state and then switches to the mode A, as shown in Fig. 4.40. The battery discharge current changes from $0.8A$ to $-0.6A$, indicating the mode switch is effectively achieved.

4.4.3.8 Mode Switch: A $\rightarrow$ E

In the initial state, the load is $R_L = 10\Omega$ and the system works in the mode A. When the load R_L abruptly changes from 10Ω to 5Ω, the system encounters a brief transient state and then switches to the mode E, as shown in Fig. 4.41. The battery discharge current changes from -0.6 to $0.8A$, indicating the mode switch is effectively achieved.

Furthermore, in mode A of 45 W, the system efficiency is shown in Fig. 4.42.

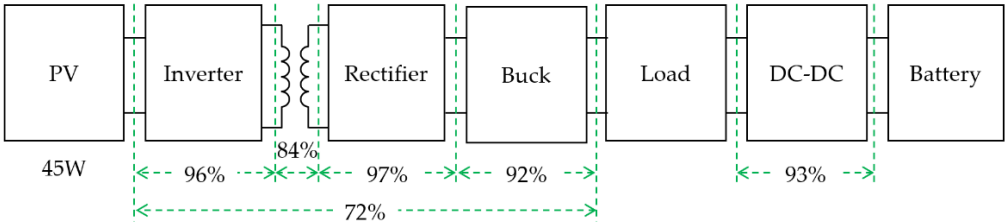

FIGURE 4.42: System efficiency in mode A.

4.5 Summary

In this chapter, based on the power supply and request relation of the PV, load and battery, a 6-mode power management strategy is proposed. The working modes are determined based on the solar irradiance intensity and rover side power requirements. In general, the system working state can be analyzed based on the PV modes, namely the MPPT and OPPT state. Due to the different positions of the converter used to conduct the PV MPPT control in the TC and RC topologies, the system control methods of OPPT state are also different. Based on the experiment results, the proposed 6-mode power management strategy is valid for both the TC and RC topology WPT systems, and when the working condition parameters change, such as the solar irradiance and load variations, the working mode can be switched automatically.

Chapter 5

Lunar Rover WPT System DC-to-DC Efficiency Tracking with Parameter Variation

The temperature of Moon surface varies intensely between the lunar day and night. In the lunar rover WPT system, the transmitter side is completely exposed to the lunar circumstances. So far, due to the material limit, the inductance and capacitance of the WPT devices will deviate from the nominal values with temperature variations.

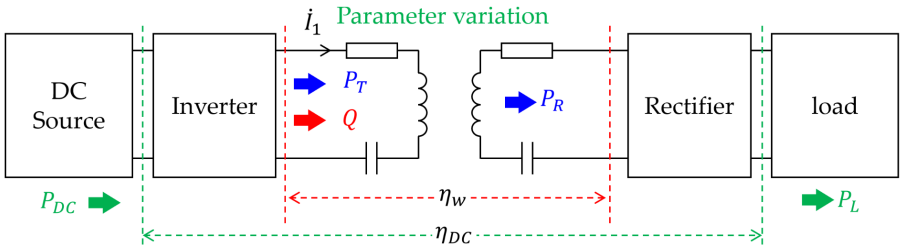

FIGURE 5.1: Employed WPT system with parameter variations.

Based on the Fig. 5.1. it can be concluded that with temperature variations, the inductance and capacitance will deviate from the nominal values, indicating the WPT system can not be resonated at the preset inverter frequency based on the device nominal values. In this case, the inverter will output reactive power to the transmitter, and not only the WPT module efficiency η_w will be influenced, but also the DC-to-DC efficiency η_{DC} will be reduced. However, based on the lunar rover design expectations, even though there is parameter variation, the whole system DC-to-DC efficiency should be kept at the maximum. Therefore, the WPT system with parameter variation DC-to-DC efficiency property should be analyzed.

5.1 WPT Module with Parameter Variation Property

With parameter variations the SS topology can be transformed in Fig. 5.2.

Based on the equivalent circuit, the following impedance analysis can be obtained.

$$Z_a = R_2 + R_L + jX_a \tag{5.1}$$

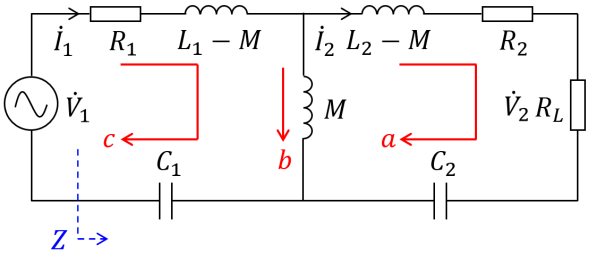

FIGURE 5.2: Eequivalent SS topology circuit.

$$Z_b = \frac{1}{\frac{1}{a} + \frac{1}{jX_b}} \tag{5.2}$$

$$Z_c = R_1 + Z_b + jX_c \tag{5.3}$$

$$Z_a = X_a = \omega\left(L_2 - M\right) - \frac{1}{\omega C_2} \tag{5.4}$$

$$X_b = \omega M \tag{5.5}$$

$$X_c = \omega\left(L_1 - M\right) - \frac{1}{\omega C_1} \tag{5.6}$$

Therefore, the WPT module currents and voltages can be obtained as follows.

$$\dot{V}_1 = V_1 \tag{5.7}$$

$$\begin{aligned} \dot{I}_1 &= I_{1-\text{real}} + jI_{1\_i\,\text{mag}} \\ &= V_1\left[\frac{\left(X_a + X_b\right)\alpha + \left(R_2 + R_L\right)\beta}{\alpha^2 + \beta^2} + j\frac{\left(X_a + X_b\right)\beta - \left(R_2 + R_L\right)\alpha}{\alpha^2 + \beta^2}\right] \end{aligned} \tag{5.8}$$

$$\dot{V}_2 = V_{2-real} + jV_{2\_imag} = R_L V_1 X_b\left(\frac{\alpha}{\alpha^2 + \beta^2} + j\frac{\beta}{\alpha^2 + \beta^2}\right) \tag{5.9}$$

$$\dot{I}_2 = I_{2-\text{real}} + jI_{2\_i\,\text{mag}} = V_1 X_b\left(\frac{\alpha}{\alpha^2 + \beta^2} + j\frac{\beta}{\alpha^2 + \beta^2}\right) \tag{5.10}$$

In the equations, the α and β can be obtained in the following.

$$\alpha = R_1 X_a + \left(R_1 + R_2 + R_L\right) X_b + \left(R_2 + R_L\right) X_c \tag{5.11}$$

$$\beta = R_1\left(R_2 + R_L\right) - X_a X_b - X_a X_c - X_b X_c \tag{5.12}$$

Based on the above equations, the WPT module efficiency η_w can be obtained as follows.

$$\eta_w = \frac{P_{out}}{P_{in}} = \frac{R_L X_b^2}{R_1\left[(R_2+R_L)^2+(X_a+X_b)^2\right]+(X_a+X_b)X_b^2} = f(\omega, R_L) \tag{5.13}$$

Based on Equ. 5.13, it can be concluded that the WPT module efficiency η_w is a binary function of ω and R_L, and in order to track the η_w maximum, the simultaneous tuning of ω and R_L should be conducted.

Furthermore, the whole system DC-to-DC efficiency is not only influenced by the WPT module efficiency but also the power factor PF. Therefore, with parameter variations, the system PF can be obtained as follows.

$$PF = \frac{P}{S} = \frac{V_1 I_{1\_real}}{V_1\sqrt{I_{1\_real}^2 + I_{1\_imag}^2}} \tag{5.14}$$

$$\Rightarrow PF = g(\omega, R_L) = \frac{A_1}{\sqrt{A_2 A_3}} \tag{5.15}$$

In the equation, the following can be obtained.

$$A_1 = R_1\left[(R_2+R_L)^2+(X_a+X_b)^2\right]+X_b^2(R_2+R_L) \tag{5.16}$$

$$A_2 = (R_2+R_L)^2+(X_a+X_b)^2 \tag{5.17}$$

$$\begin{aligned} A_3 =& R_1^2\left[(R_2+R_L)^2+(X_a+X_b)^2\right]+(R_2+R_L)^2(X_b+X_c)^2+2R_1X_b^2(R_2+R_L) \\ &+X_a^2(X_b+X_c)^2+X_bX_c(2X_aX_b+2X_aX_c+X_bX_c) \end{aligned} \tag{5.18}$$

Therefore, similar to the efficiency η_w, PF is also a binary function of ω and R_L, and in order to track the η_w maximum, the simultaneous tuning of ω and R_L should be conducted.

In order to track the maximum DC-to-DC efficiency η_{DC_max}, the η_{DC} monotonicity should be analyzed: on one hand, if η_{DC} only possesses single peak, the conventional hillclimbing method can track the maximum; on the other hand, if there are multiple peaks of η_{DC}, the global maximum tracking method should be employed. The η_{DC} monotonicity will be analyzed based on η_w and PF.

5.2 WPT Module Efficiency Monotonicity Analysis

Based on the above analysis, the WPT module efficiency η_w can be expressed in Equ. 5.13. Because it is a binary function of ω and R_L, the η_w surface monotonicity will be analyzed in two aspects.

5.2.1 WPT Efficiency Derivative with Respect to Angular Velocity

Based on the Equ. 5.13, the derivative can be obtained as follows.

$$\frac{\partial \eta_w}{\partial \omega} = 0 \quad \Rightarrow f_1(x) = a_1\omega^5 + c_1\omega^3 = 0 \tag{5.19}$$

In the equation, the following can be obtained.

$$c_1 = 2 \tag{5.20}$$

$$a_1 = C_2\left(C_2R_2^2 + 2C_2R_2R_L + C_2R_L^2 - 2L_2\right) < 0 \tag{5.21}$$

Therefore, the zero solution of ω can be obtained in the following.

$$\omega = 0, \sqrt{-\frac{c_1}{a_1}}, -\sqrt{-\frac{c_1}{a_1}} \tag{5.22}$$

The function $f_1(x)$ rough curve can be obtained in Fig. 5.3.

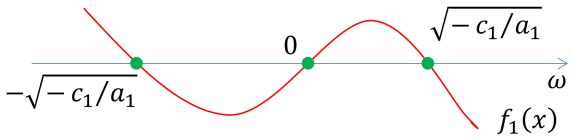

FIGURE 5.3: Derivative $f_1(x)$ zero solution distribution.

Based on Fig. 5.3, it can be concluded that with ω increasing from 0, $f_1(x)$ changes from positive to negative, and therefore, η_w monotonically increases and then decreases with respect to ω.

5.2.2 WPT Efficiency Derivative with Respect to Load

Based on the Equ. 5.13, the derivative can be obtained as follows.

$$\frac{\partial \eta_w}{\partial R_L} = 0 \quad \Rightarrow f_2(x) = a_2R_L^2 + c_2 = 0 \tag{5.23}$$

In the equation, the following can be obtained.

$$c_2 = C_2^2\omega^4\left(R_1L_2^2 + R_2M^2\right) + R_1C_2\omega^2\left(R_2^2C_2 - 2L_2\right) + R_1 > 0 \tag{5.24}$$

$$a_2 = -C_2^4M^2\left(R_1L_2^2 + R_2M^2\right) < 0 \tag{5.25}$$

Therefore, the zero solution of ω can be obtained in the following.

$$R_L = \sqrt{-\frac{c_2}{a_2}}, -\sqrt{-\frac{c_2}{a_2}} \tag{5.26}$$

The function $f_2(x)$ rough curve can be obtained in Fig. 5.4.

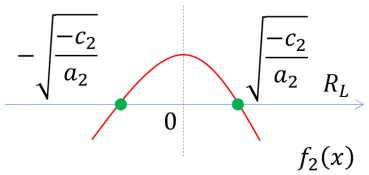

FIGURE 5.4: Derivative $f_2(x)$ zero solution distribution.

TABLE 5.1: Employed WPT Parameters Parameter Variation Case.

Symbol	Quantity	Symbol	Quantity
L_1	0.616 mH	L_2	0.616 mH
C_1	5.69e-9 F	C_2	5.69e-9 F
R_1	1.4 Ω	R_2	1.4 Ω
f_{nom}	85 kHz	k	0.15

Based on Fig. 5.4, it can be concluded that with ω increasing from 0, $f_1(x)$ changes from positive to negative, and therefore, η_w monotonically increases and then decreases with respect to R_L.

5.2.3 WPT Efficiency Surface Property

With the monotonicity analysis of ω and R_L, the following η_w surface property can be obtained.

$$\exists!\left(\omega_\xi, R_{L\xi}\right) \in \{\omega, R_L | \omega > 0, R_L > 0\}, \left(\frac{\partial \eta_w}{\partial \omega}, \frac{\partial \eta_w}{\partial R_L}\right) | \omega = \omega_{\xi,R_L} = R_{L\xi} = (0,0) \tag{5.27}$$

There is only one position $\left(\omega_\xi, R_{L\xi}\right)$ at which the derivatives of η_w respect to ω and R_L are equal to zero.

$$\exists \varepsilon > 0, \forall \left(\omega_\delta, R_{L\delta}\right) \in U_o\left[\left(\omega_\xi, R_{L\xi}\right), \varepsilon\right], \eta_w|_{\omega=\omega_\delta,R_L} = R_{L\xi} < \eta_w|_{\omega=\omega_\xi,R_L} = R_{L\xi} \tag{5.28}$$

In the deleted neighborhood of $\left(\omega_\xi, R_{L\xi}\right)$, all the points are lower than $\left(\omega_\xi, R_{L\xi}\right)$. Therefore, there is only one peak of η_w with simultaneous variations of ω and R_L.

In order to verify the analyzed property, a WPT simulation is conducted. The WPT parameters are shown in Tab. 5.1. Based on the simulation results in Fig. 5.5-7, the WPT efficiency η_w possesses only 1 peak with the variations of inverter frequency f and load R_L, indicating the employed η_w monotonicity analysis is verified.

5.3 Power Factor Monotonicity Analysis

The power factor is shown in Equ. 5.15, and it is also a binary function of ω and R_L. However, PF is a complex equation and the algebra solution can not be obtained. Considering the phase difference is caused by the circuit impedance, in this paper, the system impedance is employed to analyze the system power factor. Therefore,

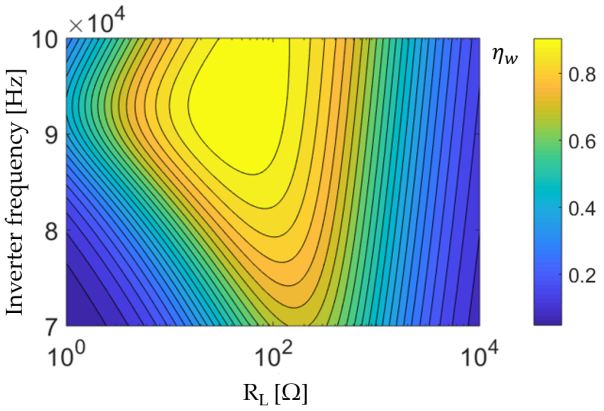

FIGURE 5.5: WPT efficiency η_ω surface distribution when $L_1 < L_2$.

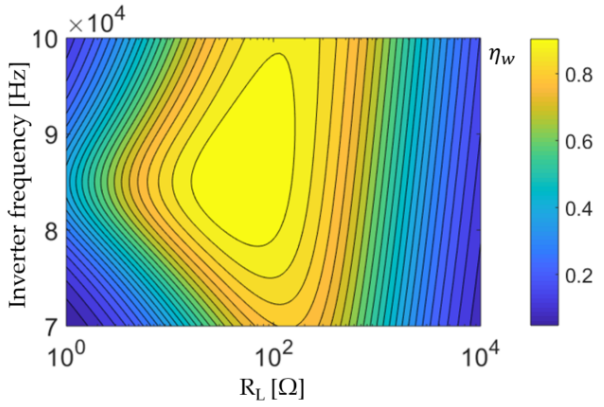

FIGURE 5.6: WPT efficiency η_ω surface distribution when $L_1 = L_2$.

it can be concluded that if impedance is purely resistive, $PF = 1$; if it is not purely resistive, $PF < 1$.

To simplify the analysis, suppose the transmitter and receiver side parameters are equal: $L_1 = L_2 = L$ and $C_1 = C_2 = C$. Then the system impedance imaginary part $\mathrm{Im}\{Z\}$ can be obtained.

$$\mathrm{Im}\{Z\} = \frac{C^3L^3\omega^6 - 3C^2L^2\omega^4 + \left[3CL - C^2\left(R + R_L\right)^2\right]\omega^2 - 1}{C\omega\left\{C^2L^2\omega^4 + \left[C^2\left(R + R_L\right)^2 - 2CL\right]\omega^2 + 1\right\}} \tag{5.29}$$

Then when $\mathrm{Im}\{Z\} = 0$, system power factor is $PF = 1$.
Suppose

$$\mathrm{Im}\{Z\} = 0 \quad \Rightarrow f_z(x) = a_z x^3 + b_z x^2 + c_z x + d_z = 0, x = \omega^2 \tag{5.30}$$

Then the derivative $f_z'(x)$ can be obtained.

$$f_z'(x) = 3a_z x^2 + 2b_z x + c_z = 0 \tag{5.31}$$

The zero solution can be obtained.

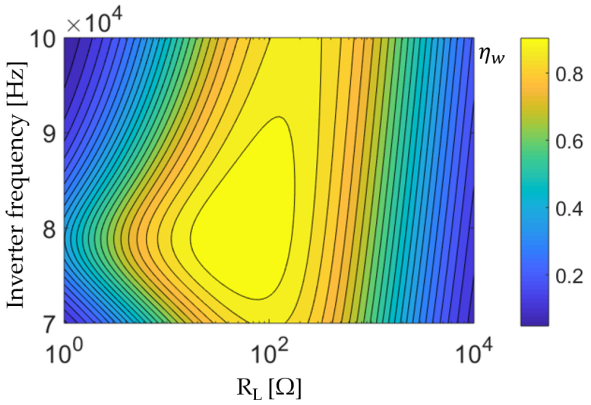

FIGURE 5.7: WPT efficiency η_ω surface distribution when $L_1 > L_2$.

$$x = \frac{\pm\sqrt{B_1} + B_2}{B_3} \tag{5.32}$$

In the equation, the following can be obtained.

$$\begin{aligned} B_1 =& C^2R_L^4 + 4C^2RR_L^3 + \left(6C^2R^2 + CLk^2 - 3CL\right)R_L^2 + \left(4C^2R^3 + 2CLRk^2 - 6CLk\right)R_L \\ &+ C^2R^4 + CLR^2k^2 - 3CLR^2 + 2CLR + L^2k^4 - 3L^2k^2 \\ =& C^2R_L^4 + 4C^2RR_L^3 - 3CLR_L^2 - 6CLRR_L - 3CLR^2 + L^2k^2 \end{aligned} \tag{5.33}$$

$$B_2 = 2CRR_L + CR^2 - 3L + CRL^2 + Lk^2 \tag{5.34}$$

$$B_3 = 3CL^2 - CL^2k^2 \tag{5.35}$$

Then the following can be conluded:

$$R_L \text{ low} \rightarrow B_1 > 0 \tag{5.36}$$

$$R_L \text{ high } \rightarrow B_1 < 0 \tag{5.37}$$

$$R_L \text{ extremely high } \rightarrow B_1 > 0 \tag{5.38}$$

When the R_L is extremely high, it is mot applicable to the WPT system and then in this research, the case of extremely hig R_L is omitted.

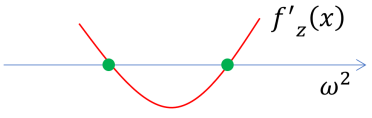

FIGURE 5.8: Derivative $f'(x)$ zero solution distribution.

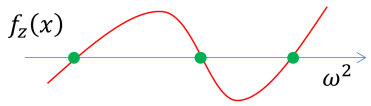

FIGURE 5.9: Derivative $f_z(x)$ zero solution distribution.

Therefore, the zero solution $f_z'(x)$ can be analyzed.
(1) When $R_L \gg R$

$$f'(x) > 0 \Rightarrow \exists \omega_0 \in (0, \infty), \text{Im}\{Z\}\big|_{\omega=\omega_0} = 0 \tag{5.39}$$

In this case, $f_z(x)$ monotonically increases and there is only one zero solution of $f_z(x) = 0$ with ω variation.
(2) When $R_L! \gg R$

$$\exists x_1, x_2 \in (0, \infty), f'(x)\big|_{x=x_1 \| x=x_2} = 0 \tag{5.40}$$

$$\Rightarrow \exists \omega_1, \omega_2, \omega_3 \in (0, \infty), Im\{Z\}\big|_{\omega=\omega_1 \| \omega_2 \| \omega_3} = 0 \tag{5.41}$$

In this case, there are 3 zero solutions of $f_z(x) = 0$ with ω variation as shown in Fig. 5.8 and 5.9.

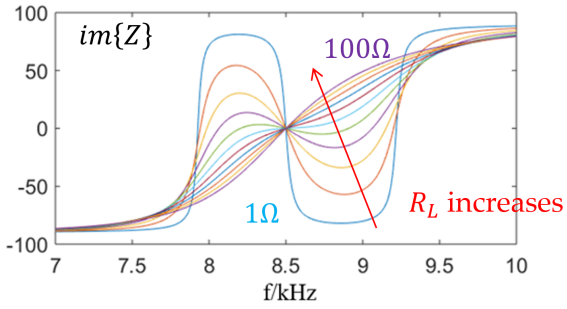

FIGURE 5.10: Im $\{z\}$ variation when frequency f and load R_L change simultaneously.

Based on the above analysis, with the parameters in Tab. 5.1, the system impedance Z is simulated in Fig. 5.10. It can be concluded that when R_L increases from 1Ω to $10^4\Omega$, the zero solution number decreases from 3 to 1, indicating the employed $Im\{Z\}$ analysis is verified.

The system power factor PF is simulated in Fig. 5.11-13, it also can be concluded that with R_L increasing, the PF peak number changes from 3 to 1, indicating the above analysis is verified.

5.4 WPT System DC-to-DC Efficiency Simulation

In order to analyze the WPT system DC-to-DC efficiency η_{DC}, a simulation with the parameters in Tab. 5.1 is conducted with matlab and η_{DC} is shown in Fig. 5.14.

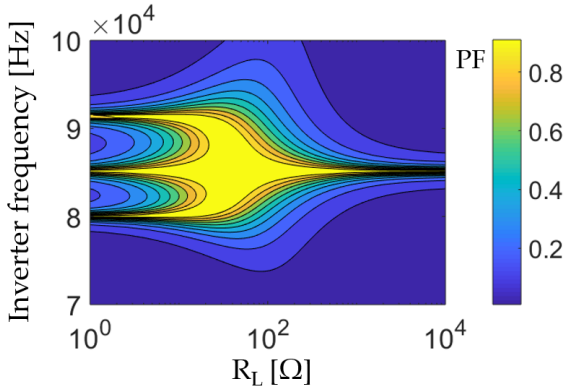

FIGURE 5.11: Power factor PF surface distribution when $L_1 = L_2$.

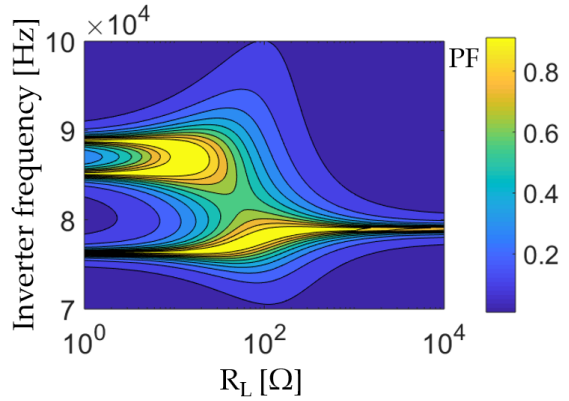

FIGURE 5.12: Power factor PF surface distribution when $L_1 < L_2$.

Based on Fig. 5.14, the following can be concluded: (1) η_{DC} is more influenced by PF compared with η_w; (2) with R_L increasing, the η_{DC} peak number decreases from 3 to 1; (3) the global maximum tracking method should be required to track the η_{DC} maximum.

5.5 DC-to-DC Efficiency Maximum Tracking with Simulated Annealing Method

5.5.1 Simulated Annealing Algorithm General Principle

SA algorithm is a probabilistic method for tracking the global maximum and it is conducted based on the annealing process in metallurgy as shown in Fig. 5.15. In the annealing process, when the metal temperature is high, the internal particles distributed without order; when the temperature is low, the internal particles are in uniform pattern. Then the system temperature can effectively express the current system disorder degree as shown in Fig. 5.15.

In the SA algorithm, when the system encounters some perturb, if the energy state is higher than the current value, the perturb will be accepted by the system and the system temperature will be reduced with one step down. If the energy state is not higher than the current value, the probability of accepting the perturb will be calculated as shown in Fig. 5.16. The probability is calculated based on the current system energy state and temperature in Equ. 5.42.

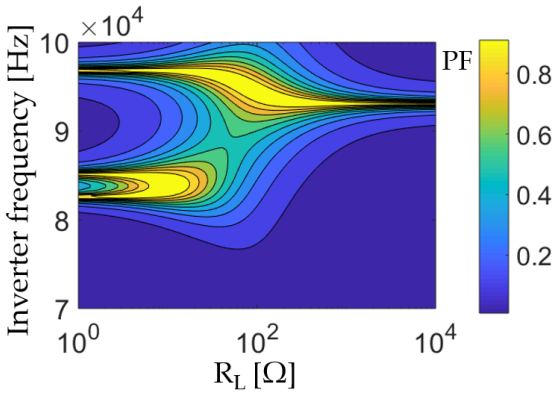

FIGURE 5.13: Power factor PF surface distribution when $L_1 > L_2$.

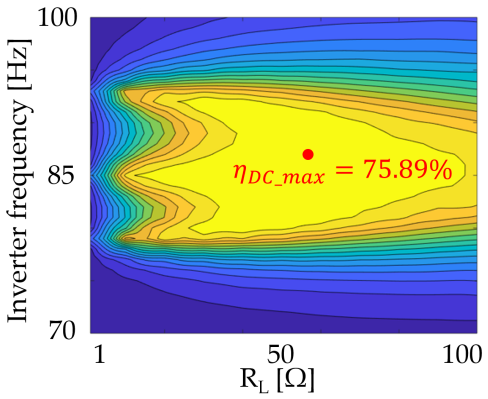

FIGURE 5.14: System DC-to-DC efficiency η_{DC} simulation.

$$P_{sa} = e^{\frac{E_{cu} - E_{pre}}{T_{cu} - T_{pre}}} \tag{5.42}$$

In the equation, E_{cu} and E_{pre} are the system previous and current energy state; T_{cu} and T_{pre} are the system current and previous temperature; P_{sa} is the acceptance probability. In the algorithm, the obtained acceptance probability P_{sa} will be compared with random value P_{rand}.

$$P_{sa} > P_{rand} \Rightarrow \text{ Perturb accepted} \tag{5.43}$$

$$P_{sa} < P_{rand} \Rightarrow \text{Perturb not accepted} \tag{5.44}$$

Based on Equ. 5.42, it can be concluded that with the system temperature decreasing, the acceptance probability P_{sa} will be reduced continuously and with enough iterations, th P_{sa} will be low enough. At this time, the SA algorithm will be ended and the global maximum will be tracked.

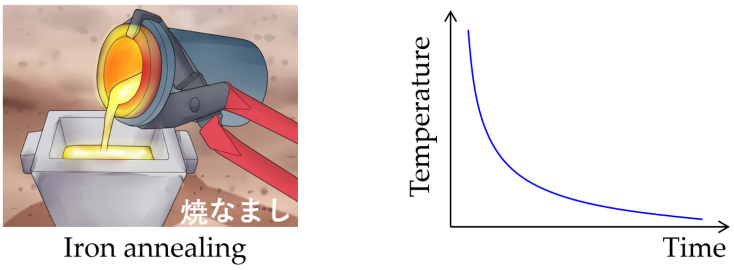

FIGURE 5.15: (a) Iron annealing. (b) Temperature variation in inron annealing process.

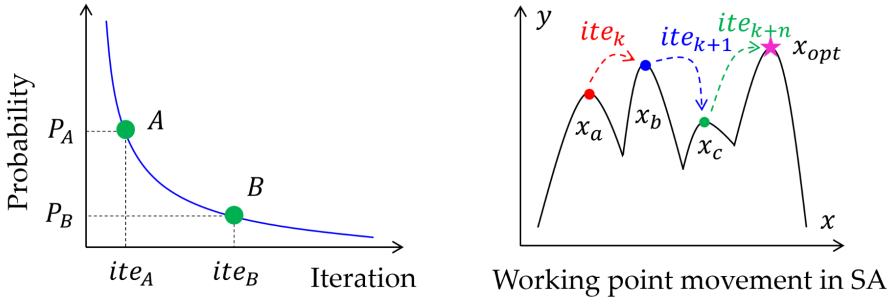

FIGURE 5.16: (a) Probability variation in simulated annealing algorithm. (b) Global maximum tracking process in simulated annealing algorithm.

5.5.2 SA Algorithm Design for DC-to-DC Efficiency Tracking

In this paper, the DC-to-DC efficiency η_{DC} is taken as the system energy state. Therefore, the acceptance probability P_{sa} can be calculated as follows.

$$P_{sa} = e^{\frac{\eta_{DC\_cu} - \eta_{DC\_pre}}{T_{cu} - T_{pre}}} \tag{5.45}$$

In this paper, the system perturb is conducted with simultaneous ω and R_L variations. In the implementation, ω and R_L variations are achieved with inverter frequency and converter duty changes, respectively. The proposed SA method flowchart is shown in Fig. 5.17.

5.6 Simulation Verification

In this research, in order to simplify the tracking simulation, the system parameter variation is achieved based on the inductance variation. Furthermore, 6 cases of simulation parameter variations are employed in this section. The parameters of 6 cases are shown in Tab. 5.2.

In this paper, in order to assess the algorithm MPPT performance, the following parameters are defined. The algorithm MPPT time T_{tra} is defined as the time from the moment when the system starts to the moment when the steady PV output power P_{sta} error is limited within 5% compared with the theory maximum power

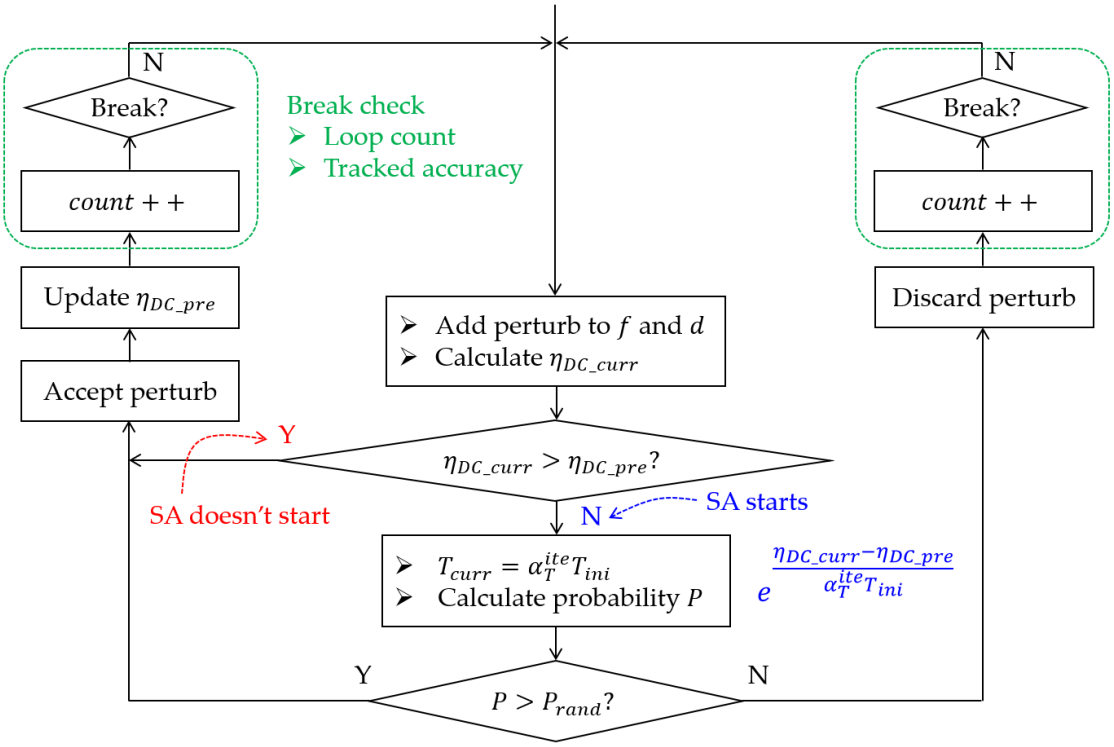

FIGURE 5.17: Proposed η_{DC} maximum tracking simulated annealing method flowchart.

P_{max}. Furthermore, the algorithm MPPT tracking accuracy A_{tra} is defined as the ratio between the PV output power P_{sta} in the stable state and P_{max}. The parameters of T_{tra} and A_{tra} can assess the algorithm MPPT performance of accuracy.

Based on Tab. 5.2, the preset nominal inductance L_{nom} of 6 cases are invalid and all the inductors deviate to the real inductance, namely $L_{real} = 0.616mH$. The preset nominal inverter frequencies f_{nom} are set as 75, 77, 81, 90, 95 and 101 kHz, respectively. With parameter variations, the real resonance frequency of 6 cases is $f_{real} = 85kHz$. Furthermore, with the initial circuit properties, the nominal optimal resistance R_{L_nom} is also preset based on Equ. 3.8, and they are 43, 45, 47, 52, 55 and 60 Ω, respectively. However, Based on real circuit parameters, the real optimal resistance of 6 cases is $R_{L\_real} = 49\Omega$.

The simulated annealing algorithm parameters are: $T_{in} = 1000$, $T_{fi} = 1e^{-10}$ and $\alpha_T = 0.7$. The algorithm frequency is set as 20 Hz. The tracking results of 6

TABLE 5.2: 6 cases of employed parameter variations.

Case	L_{nom}/mH	**Offset**	L_{real}/mH	$R_{L\_nom}\Omega$	R_{L_real}/Ω	f_{nom}/kHz	f_{real}/kHz
1	0.791	-22.12%	0.616	43	49	75	85
2	0.751	-17.98%	0.616	45	49	77	85
3	0.679	-9.28%	0.616	47	49	81	85
4	0.550	+12.00%	0.616	52	49	90	85
5	0.493	+24.95%	0.616	55	49	95	85
6	0.436	+41.28%	0.616	60	49	101	85

TABLE 5.3: Tracking efficiency and accuracy of 6 parameter variation cases.

Case	η_{sta}	A_{tra}	**Iteration**	T_{tra}
1	75.25%	99.16%	6	0.30
2	75.39%	99.34%	8	0.40
3	75.32%	99.25%	8	0.40
4	75.42%	99.38%	18	0.90
5	75.41%	99.37%	11	0.90
6	75.42%	99.38%	13	0.65

simulation cases are shown in Fig. 5.18-22.

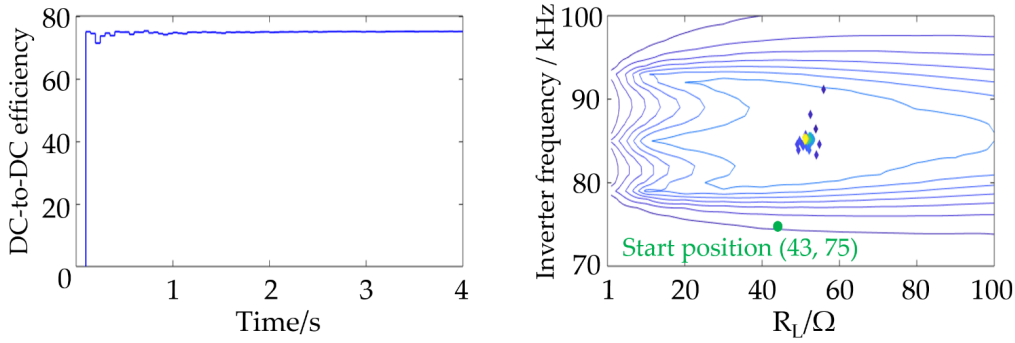

FIGURE 5.18: Simulation results of case 1.

In case 1, the initial inverter frequency and optimal load are set as $f_{nom} = 75kHz$ and $R_{L\_nom} = 43\Omega$, respectively. Due to the parameter variations in Tab. 5.2, the real circuit parameters should be set: $f_{real} = 85kHz$ and $R_{L\_real} = 49\Omega$.

In Fig. 5.18, with the start position of (43, 75), the system working point gradually moves toward the optimal position at which the DC-to-DC efficiency can approach the maximum of η_{DC_max} (the system working point changes from blue to yellow with time). Furthermore, after 0.30 s (6 iterations), the system enters the steady state and the tracked system stable efficiency is $\eta_{sta} = 75.25\%$ demonstrating the proposed SA method has achieved $A_{tra} = 99.16\%$ tracking accuracy.

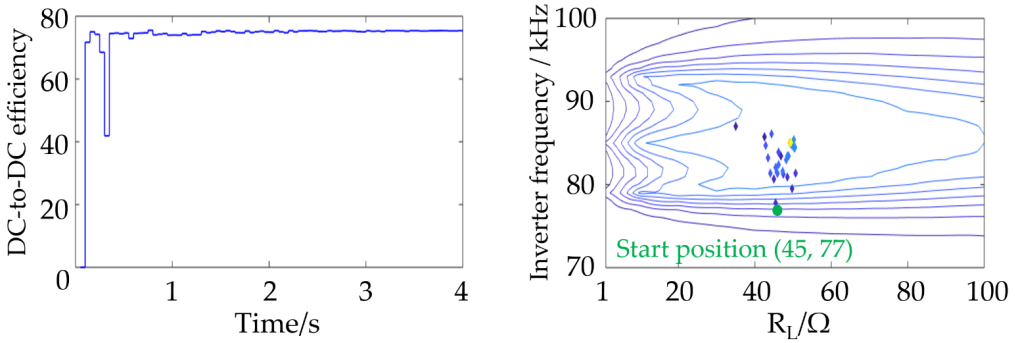

FIGURE 5.19: Simulation results of case 2.

In case 2, in the initial state: $f_{nom} = 77kHz$ and $R_{L\_nom} = 45\Omega$. In Fig. 5.19, the

system starts at the position of (45, 77), and the working point gradually moves toward the maximum efficiency point. After 0.40 s (8 iterations), the system enters the steady state, and the tracked efficiency is $\eta_{sta} = 75.39\%$ with the tracking accuracy as $A_{tra} = 99.34\%$.

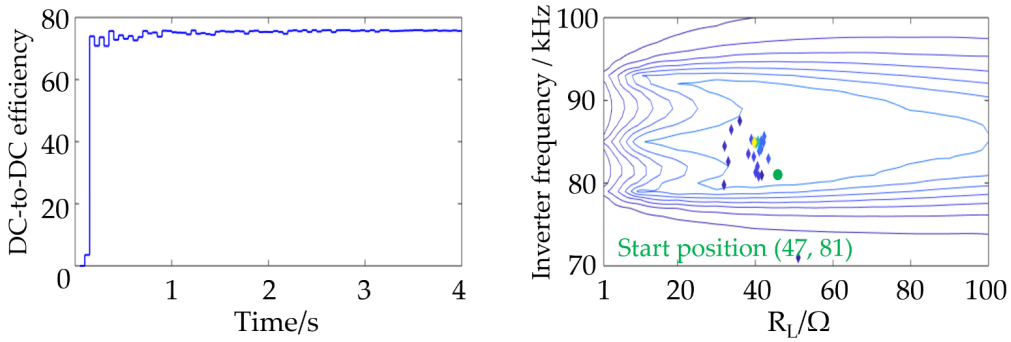

FIGURE 5.20: Simulation results of case 3.

In case 3, in the initial state: $f_{nom} = 81kHz$ and $R_{L\_nom} = 47\Omega$. In Fig. 5.20, the system starts at the position of (47, 81), and the working point gradually moves toward the maximum efficiency point. After 0.40 s (8 iterations), the system enters the steady state, and the tracked efficiency is $\eta_{sta} = 75.32\%$ with the tracking accuracy as $A_{tra} = 99.25\%$.

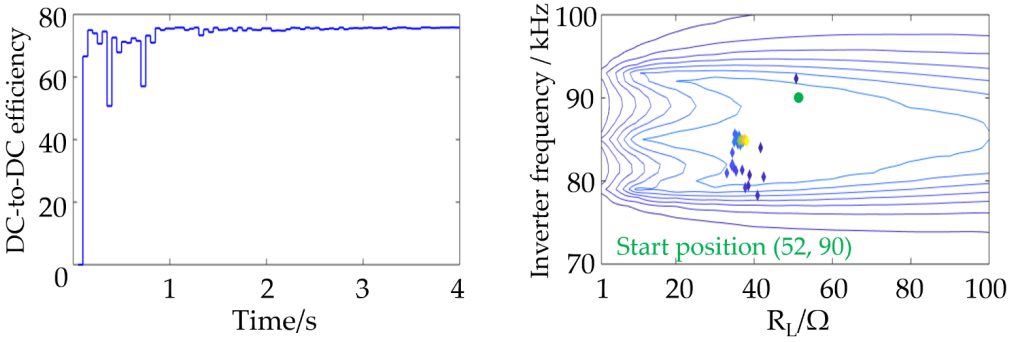

FIGURE 5.21: Simulation results of case 4.

In case 4, in the initial state: $f_{nom} = 90kHz$ and $R_{L\_nom} = 52\Omega$. In Fig. 5.21, the system starts at the position of (52, 90), and the working point gradually moves toward the maximum efficiency point. After 0.90 s (18 iterations), the system enters the steady state, and the tracked efficiency is $\eta_{sta} = 75.42\%$ with the tracking accuracy as $A_{tra} = 99.38\%$.

In case 5, in the initial state: $f_{nom} = 95kHz$ and $R_{L\_nom} = 55\Omega$. In Fig. 5.22, the system starts at the position of (55, 95), and the working point gradually moves toward the maximum efficiency point. After 0.50 s (11 iterations), the system enters the steady state, and the tracked efficiency is $\eta_{sta} = 75.41\%$ with the tracking accuracy as $A_{tra} = 99.37\%$.

In case 6, in the initial state: $f_{nom} = 101kHz$ and $R_{L\_nom} = 60\Omega$. In Fig. 5.23, the system starts at the position of (60, 101), and the working point gradually moves toward the maximum efficiency point. After 0.65 s (13 iterations), the system enters the steady state, and the tracked efficiency is $\eta_{sta} = 75.42\%$ with the tracking accuracy as $A_{tra} = 99.38\%$.

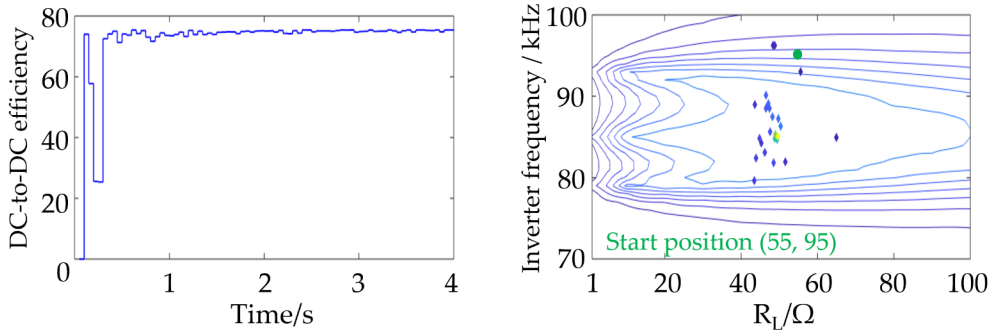

FIGURE 5.22: Simulation results of case 5.

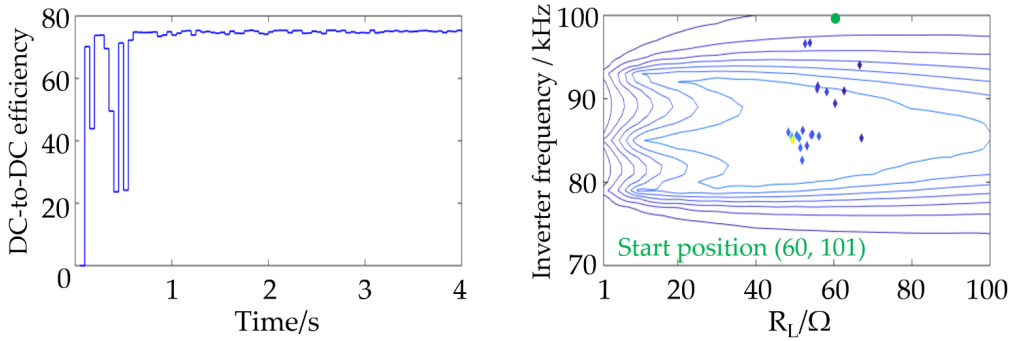

FIGURE 5.23: Simulation results of case 6.

TABLE 5.4: Tracking efficiency and accuracy of each 100 times.

Item	Case 1	Case 2	Case 3	Case 4	Case 5	Case 6
η_{sta}	75.26%	75.16%	75.29%	75.17%	75.01%	75.03%
A_{tra}	99.16%	99.04%	99.21%	99.06%	98.85%	98.87%

Furthermore, in order to verify the proposed simulated annealing method feasibility, each case is conducted for each 100 times, and the results are shown in Tab. 5.4. The average steady state efficiency η_{sta} of each case is higher than 75 % and the tracking accuracy A_{tra} is also approximately equal to 99 %. The simulation results verifies the proposed SA method feasibility.

5.7 Summary

In this chapter, a WPT system DC-to-DC efficiency maximum tracking SA method is proposed. When the parameter variations happen to the WPT circuit transmitter side devices, the DC-to-DC efficiency is demonstrated to be a multiple-peak surface with the simultaneous inverter frequency and load variations. In the proposed method, the system DC-to-DC efficiency is employed as the state energy, and both the inverter frequency and load are adopted as the system perturb. In order to verify the proposed SA method, 6 cases of parameter variations with different preset nominal parameters are employed. Based on the simulation results, all the DC-to-DC efficiency maximums are tracked within 1 s, indicating the proposed SA method feasibility.

Chapter 6

Lunar Rover PV MPPT Algorithm

Based on the photovoltaic effect, the PV output power with respect to voltage possesses 1 peak with uniform solar irradiance and multiple peaks under partial shading conditions. Under working conditions, in order to make the most of the solar energy, the PV MPPT control should be conducted. In this section, the MPPT algorithms designed for the lunar rover will be analyzed based on the solar irradiance conditions. In section 6.1, the uniform solar irradiance case will be investigated and in section 6.2 and 6.3, the partial shading conditions will be explored.

6.1 Variant Step Incremental Conductance Method

When the solar irradiance on the PV panel is uniform, the PV output power only possesses 1 peak and in this case, the local MPPT method can track the maximum power. The one-peak PV output property is shown in Fig. 6.1.

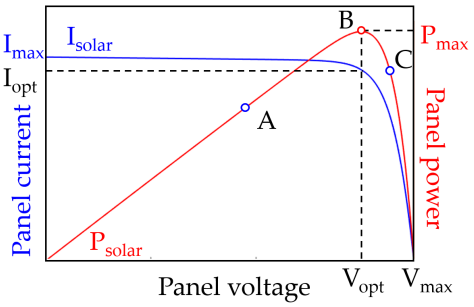

FIGURE 6.1: 1-peak PV output property.

Based on Fig. 6.1, the points A, B and C are located at the left side, peak and right side of the P-V curve, respectively. The derivatives m of points A, B and C can be obtained as follows.

$$\begin{cases} m_A = \dfrac{dP_A}{dV_A} = I_A + U_A \dfrac{dI_A}{dV_A} > 0 \\ m_B = \dfrac{dP_B}{dV_B} = I_B + U_B \dfrac{dI_B}{dV_B} = 0 \\ m_C = \dfrac{dP_C}{dV_C} = I_C + U_C \dfrac{dI_C}{dV_C} < 0 \end{cases} \tag{6.1}$$

It can be concluded that with different positions, the P-V derivative will possess different values as shown in Fig. 6.2. The derivative m will gradually approach zero when the working point moves toward the peak point.

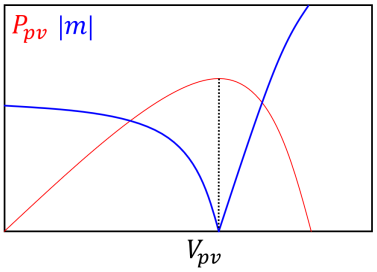

FIGURE 6.2: Derivative m of PV output P-V function.

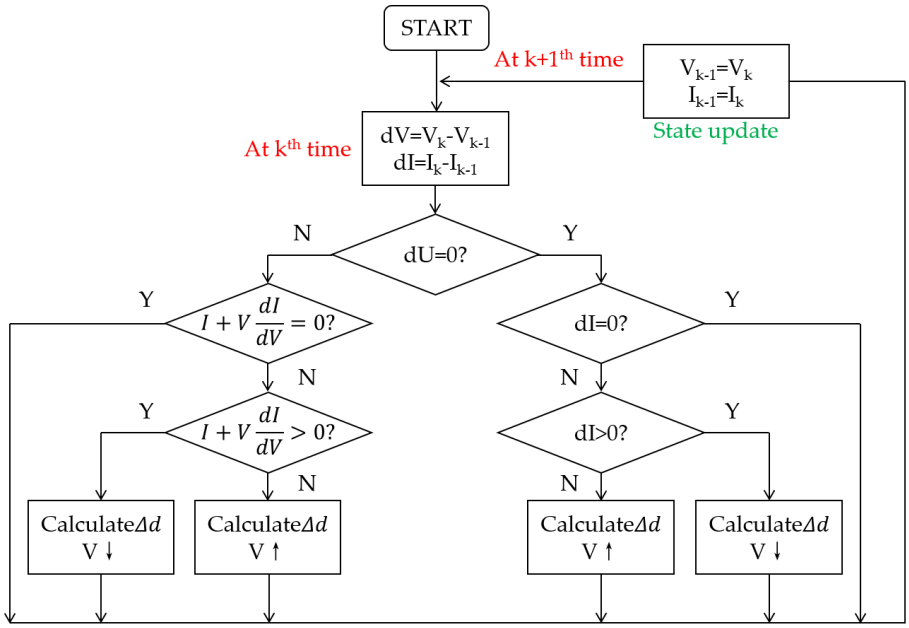

FIGURE 6.3: Variant step incremental conductance method flowchart.

In the conventional InCon method, the derivative of P_{pv} with respect to V_{pv} will be employed to detect the current system working point rough position and then the converter duty will be tuned to move the working point toward the peak point. The InCon algorithm flowchart is shown in Fig. 6.3. Furthermore, the duty step is always set as a constant value. However, when the solar irradiance intensity is different, the P-V curve will also express different properties, as shown in Fig. 6.4. Therefore, for the case of $|m_1|$ with higher derivative descent/ascent, especially at the peak range, the step should be reduced to track the optimal position with higher accuracy. For the case of $|m_3|$ with lower derivative descent/ascent, the step can be increased moderately to accelerate the tracking process. Therefore, the conventional InCon will not be appropriate for all the cases. In order to solve this issue, in this research, a variant step InCon method is proposed.

The P-V derivative m can be obtained.

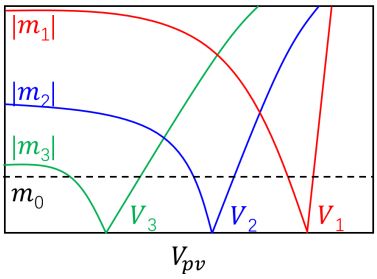

FIGURE 6.4: Derivative m_1, m_2 and m_3.

$$m = \frac{dP_{pv}}{dV_{pv}} \tag{6.2}$$

At the peal point, m will approach zero.

$$\lim_{P_{pv} \to P_{pv\_max}} \left| \frac{dP_{pv}}{dV_{pv}} \right| = 0 \tag{6.3}$$

Then the duty step variation can be obtained as follows.

$$\Delta d = N \left| \frac{dP_{pv}}{dV_{pv}} \right| \tag{6.4}$$

$$d(k) = d(k-1) \pm \Delta d \tag{6.5}$$

In the equation, N should be low for $|m_1|$ and high for $|m_3|$. In the proposed method, the ratio of peak power and voltage is considered to tune N. Because the area where the lunar rover will be launched is known in advance, the PV output property with the medium solar irradiance can be taken as the tuning standard as shown in Fig. 6.5. In this case, the PV output power P_0 and voltage V_0 are employed as follows.

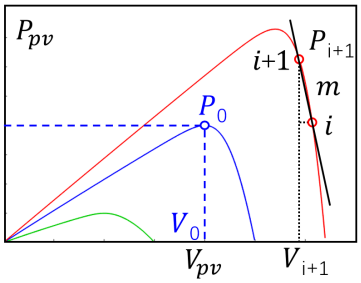

FIGURE 6.5: Variant step analysis.

$$|m| > m_0 \quad \Delta d = N_0 \left| \frac{dP}{dV} \right| \tag{6.6}$$

TABLE 6.1: Employed PV property of 45 W

V_{oc}/V	I_{sc}/A	V_{opt}/V	I_{opt}/A	P_{max}
35	1.6	30	1.5	45

$$|m| \leq m_0 \quad \Delta d = N_0 \left|\frac{dP}{dV}\right| \frac{P_0/V_0}{P/V} \tag{6.7}$$

With the assistance of $\frac{P_0/V_0}{P/V}$, the duty step Δd can be tuned considering the P-V curve derivative descent/ascent. For example, for the case of m_1, Δd can be reduced for higher tracking accuracy but for the case of m_3, Δd can be effectively increased to accelerate the tracking process.

6.1.1 Experiment Verification

The proposed variant step InCon method is verified with experiments. The employed PV output property is shown in Fig. 6.6 and the parameters are shown in Tab. 6.1. The experiment results of the conventional and variant step InCon methods are shown in Fig. 6.7 and 6.8.

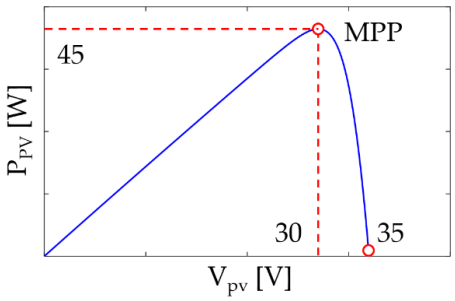

FIGURE 6.6: Employed 1-peak PV output property.

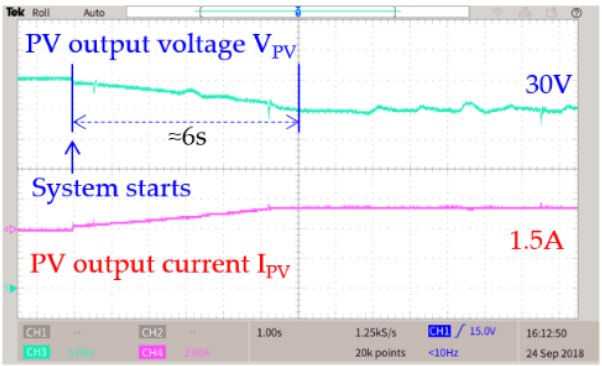

FIGURE 6.7: Experiment results of conventional incremental conductance method.

In Fig. 6.7, when the duty step and algorithm frequency are set as $\Delta step = 0.002$ and $f_{al} = 50Hz$, the tracking time is $T_{tra} = 6.0s$. Furthermore, after the maximum

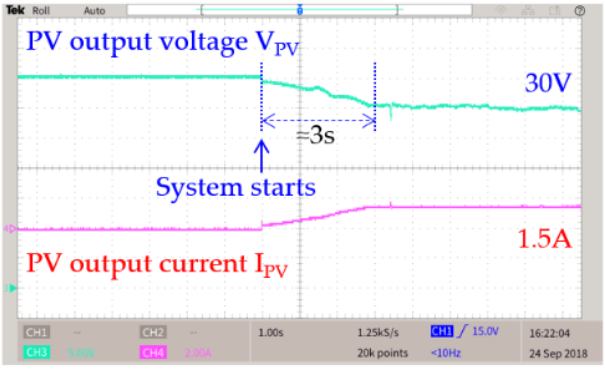

FIGURE 6.8: Experiment results of proposed variant step incremental conductance method.

power point is tracked, the PV output fluctuation is still intense, indicating the system working point is oscillating around the optimal position. Under working conditions, these oscillations will cause system instability and should be avoided as much as possible. In Fig. 6.8, the variant step is employed and the algorithm is also set as $f_{al} = 50Hz$. The tracking time is reduced as $T_{tra} = 3s$ and furthermore, the oscillation is also reduced after the optimal working position is tracked because the step at peak area is reduced.

Based on the above experiment results and analysis, the proposed variant step InCon method feasibility has been verified.

6.2 Particle Replace Particle Swarm Optimization Algorithm

6.2.1 PSO Algorithm Velocity and Position Update Property

When the lunar rover PV works in the partial shading conditions, the global MPPT algorithm should be conducted. In this research, the PSO algorithm is employed. In general, in PSO algorithm, the global maximum tracking is conducted based on the particle movements in the algorithm iteration process. The particle velocity and position update equations are shown as follows.

$$v_i^{k+1} = wv_i^k + c_1 r_1 \left(P_i - x_i^k\right) + c_2 r_2 \left(G - x_i^k\right) \tag{6.8}$$

$$x_i^{k+1} = x_i^k + v_i^{k+1} \tag{6.9}$$

In the equation, ω is the inertia weight; c_1 is the personal best acceleration coefficient; c_2 is the global best acceleration coefficient; r_1 and r_2 are the uniform distributed random numbers; P_i is the i^{th} particle personal best at the k^{th} iteration; G is the global best at the k^{th} iteration; x_i^k is the i^{th} particle duty at the k^{th} iteration; x_i^{k+1} is the i^{th} particle duty at $k+1^{th}$ iteration; v_i^k is the i^{th} particle velocity at the k^{th} iteration; v_i^{k+1} is the i^{th} particle velocity at the $k+1^{th}$ iteration.

In Equ. 6.8, c_1 and c_2 represent the particle velocity proneness to be influenced by the personal and global bests: high c_1 means the personal best can exert more influence to the particle velocity update, and then the probability of the real global maximum to be tracked is high and the whole tracking time will be prolonged; high

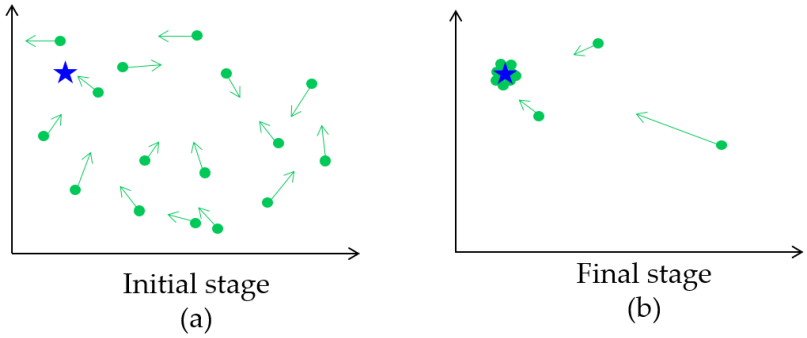

FIGURE 6.9: (a) Initial stage of PSO algorithm. (b) Final stage of PSO algorithm.

c_2 means the global best can exert can more influence, and then the probability of the real global maximum to be tracked is low but the whole tracking time will be reduced.

Based on above analysis, the flowchart of PSO algorithm can be obtained in Fig. 6.10. In the application of PSO algorithm, all the particles will gradually move to the optimal position with the constrain of personal and global bests and finally approach the convergence.

6.2.2 Gaussian Particle Swarm Optimization

Based on Equ. 6.8, there are three parameters of ω, c_1 and c_2 to be tuned before PSO algorithm starts. In order to reduce the parameter tuning task, in this research, the Gaussian particle swarm optimization (GPSO) is employed.

The GPSO velocity and position updates are shown as follows.

$$v_i^{k+1} = v_i^k + g_1\left(P_i - x_i^k\right) + g_2\left(G - x_i^k\right) \tag{6.10}$$

$$x_i^{k+1} = x_i^k + v_i^{k+1} \tag{6.11}$$

Therefore, the parameters which should be tuned only are g_1 and g_2. Furthermore, because the variance of Gaussian distribution is lower than the uniform distribution, the GPSO convergence capability should be improved.

6.2.3 Distribution Analysis on GPSO Algorithm

In this section, the distribution property of GPSO is analyzed. Based on Equ. 6.10 and 11, the following definitions can be obtained.

$$\alpha_{1i}^{(k)} = P_i - x_i^{(k)} \tag{6.12}$$

$$\alpha_{2i}^{(k)} = G - x_i^{(k)} \tag{6.13}$$

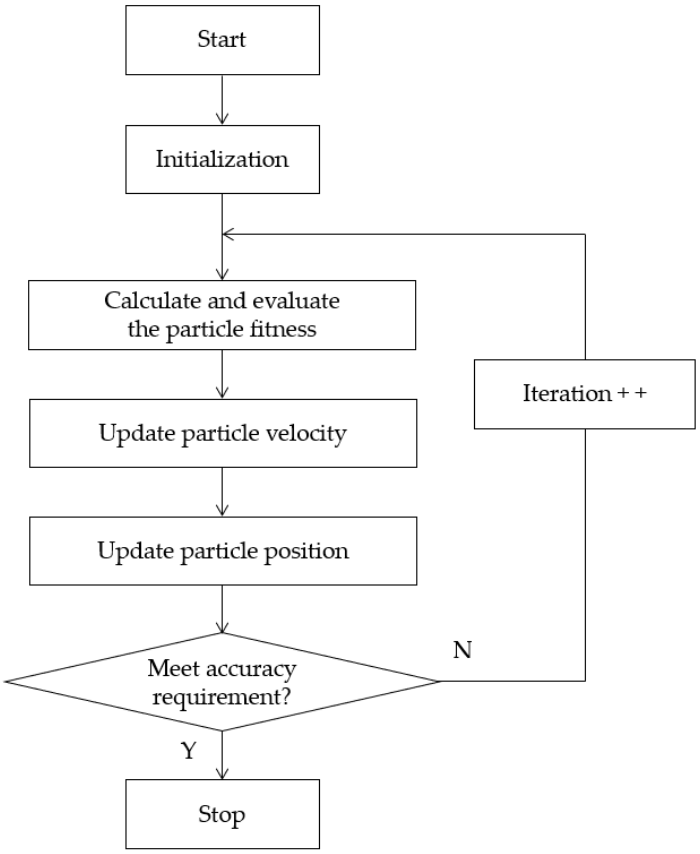

FIGURE 6.10: PSO algorithm flowchart.

$$\beta_i^{(k)} = v_i^{(k)} \tag{6.14}$$

$$\gamma_i^{(k)} = x_i^{(k)} \tag{6.15}$$

Therefore, the following can be obtained.

$$x_i^{(k+1)} = \gamma_i^{(k)} + \beta_i^{(k)} + \alpha_{1i}^{(k)} g_1 + \alpha_{2i}^{(k)} g_2 \tag{6.16}$$

Furthermore, suppose the following can be obtained.

$$Z_i^{(k)} = x_i^{(k+1)} \tag{6.17}$$

$$X_{1i}^{(k)} \sim N\left(\alpha_{1i}^{(k)}\mu_1 + \frac{\beta_i^{(k)} + \gamma_i^{(k)}}{2}, \alpha_{1i}^{2(k)}\sigma_1^2\right) \tag{6.18}$$

$$X_{2i}^{(k)} \sim N\left(\alpha_{2i}^{(k)}\mu_2 + \frac{\beta_i^{(k)} + \gamma_i^{(k)}}{2}, \alpha_{2i}^{2(k)}\sigma_2^2\right) \tag{6.19}$$

Therefore, the following can be obtained.

$$Z_i^{(k)} = X_{1i}^{(k)} + X_{2i}^{(k)} \tag{6.20}$$

The i^{th} particle distribution $Z^{(k)}$ at the k^{th} iteration follows the Gaussian distribution.

$$Z_i^{(k)} \sim N\left(\mu_i, \sigma_i^2\right) \tag{6.21}$$

$$\mu_i = \alpha_{1i}^{(k)}\mu_1 + \alpha_{2i}^{(k)}\mu_2 + \beta_i^{(k)} + \gamma_i^{(k)} \tag{6.22}$$

$$\sigma_i^2 = \alpha_{1i}^{2(k)}\sigma_1^2 + \alpha_{2i}^{2(k)}\sigma_2^2 \tag{6.23}$$

Suppose there are n_p particles at each iteration, and the distribution $Z_{ite}^{(k)}$ of all the particles of k^{th} iteration can be obtained.

$$Z_{\text{ite}}^{(k)} = \sum_{i=1}^{n_p} Z_i^{(k)} \sim N\left(\mu_{iite}, \sigma_{ite}^2\right) \tag{6.24}$$

$$\mu_{ite} = \sum_{i=1}^{n_p}\left(\alpha_{1i}^{(k)}\mu_1 + \alpha_{2i}^{(k)}\mu_2 + \beta_i^{(k)} + \gamma_i^{(k)}\right) \tag{6.25}$$

$$\sigma_{ite}^2 = \sum_{i=1}^{n_p}\left(\alpha_{1i}^{2(k)}\sigma_1^2 + \alpha_{2i}^{2(k)}\sigma_2^2\right) \tag{6.26}$$

Suppose there are n_{all} iterations conducted in GPSO algorithm, and the distribution Z_{all} of all the particles from all the iterations can be obtained in Equ. 6.27. Due to the Gaussian distribution property, the overall distribution Z_{all} of all the particles from all the iterations also follows the Gaussian distribution.

$$Z_{all} = \sum_{k=1}^{n_{all}} Z_{ite}^{(k)} = \sum_{k=1}^{n_{all}}\sum_{i=1}^{n_p} Z_i^{(k)} \sim N\left(\mu_{all}, \sigma_{all}^2\right) \tag{6.27}$$

$$\mu_{all} = \sum_{k=1}^{n_{all}}\sum_{i=1}^{n_p}\left(\alpha_{1i}^{(k)}\mu_1 + \alpha_{2i}^{(k)}\mu_2 + \beta_i^{(k)} + \gamma_i^{(k)}\right) \tag{6.28}$$

$$\sigma_{all}^2 = \sum_{k=1}^{n_{all}} \sum_{i=1}^{n_p} \left(\alpha_{1i}^{2(k)} \sigma_1^2 + \alpha_{2i}^{2(k)} \sigma_2^2 \right) \tag{6.29}$$

After the GPSO algorithm has conducted a certain iterations, the majority of particles will move to the optimal position. Therefore, the personal and global bests can be seen to share the same position.

$$x_i^{(k)} = P_i = G \tag{6.30}$$

The particle velocity update approaches zero.

$$\lim_{k>=n_1} \alpha_{1i}^{(k)} \mu_1 + \alpha_{2i}^{(k)} \mu_2 + \beta_i^{(k)} = 0 \tag{6.31}$$

Furthermore, the variance of particle distribution Z_i will also approach zero.

$$\lim_{k>=n_1} \alpha_{1i}^{2(k)} \sigma_1^2 + \alpha_{2i}^{2(k)} \sigma_2^2 = 0 \tag{6.32}$$

Therefore, the particle distribution Z_i after enough iterations can be obtained in the following.

$$Z_i^{(k)} \sim N\left(\gamma_i^{(k)}, \varepsilon^{2(k)} \right), \gamma_i^{(k)} \to G, \varepsilon^{2(k)} \to 0^+ \tag{6.33}$$

In the equation, $\varepsilon^{2(k)}$ is the variance of the i^{th} particle at the k^{th} iteration. Furthermore, k is high enough in Equ. 6.33.

Based on the above mathematical analysis, the following properties can be obtained.

(1) At the first iteration, if there are enough particles employed, it can be regarded that there will be at least one particle which is close enough to the optimal position and the fitness is higher than the other particles.

(2) Z_{all} follows the Gaussian distribution according to Equ. 6.27. In the algorithm iteration process, at the latter stage, almost all of the particles will move around the optimal position, and the particle amount which are still far from the optimal position can be omitted.

(3) Furthermore, if each iteration is focused, it also can be concluded that the particle distribution of each iteration also follows the Gaussian distribution according to Equ. 6.24. Because in GPSO, the particle movements are independent to each other, if the employed particles are enough, the particles which are far from the current tracked optimal position can be omitted, and GPSO algorithm can be driven only by the particles which are close to the optimal position without accuracy deterioration.

(4) The Z_{all} distribution can be decomposed into a sum of a series of sub Gaussian distributions.

With the above GPSO property analysis, the particle replacement method is proposed in the next section.

6.2.4 Particle Replacement Method

In the conventional PSO method, the particle movement is conducted based on the velocity and position update equations. At each iteration, the particle position is changed according to the inertia property, personal and global best positions. However, this kind of "step-by-step" particle movement will cost too much time for the particle convergence. For example, in Fig. 6.11(a), all the particle movements are achieved based on the step-by-step updates in the GPSO algorithm. However, because the particle Par_1 initial position is far from the optimal position, it takes much more time to move to the optimal position compared with the other particles of Par_2, Par_3 and Par_4. In particular, at the 4^{th} iteration, even though Par_2, Par_3 and Par_4 almost converge to the same position, because Par_1 still deviates from the optimal position, it takes more iterations for all the particles to converge to the same position.

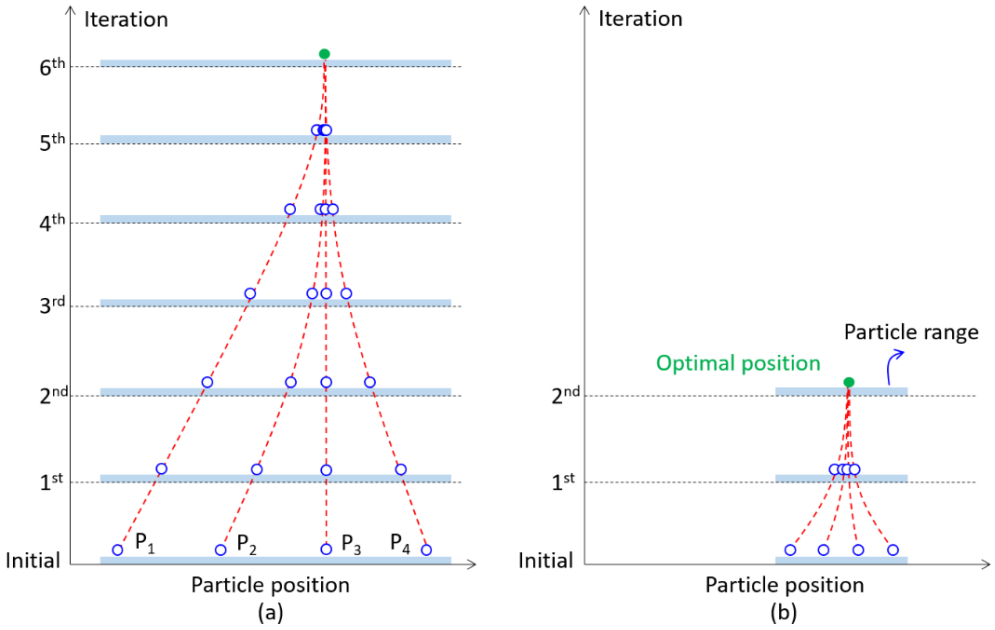

FIGURE 6.11: (a) Conventional GPSO tracking process. (b) GPSO tracking with reduced particle distribution range.

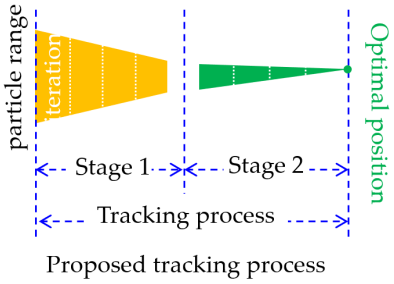

FIGURE 6.12: Proposed 2-stage tracking process.

However, if the rough optimal position is known before the GPSO tracking, the particle distribution range can be reduced and then the whole tracking time can be reduced, as shown in Fig. 6.11(b).

Therefore, in order to accelerate the particle convergence, a particle replacement (PR) method is proposed, and in this way the whole tracking process is divided into

2 stages, namely the PR stage and GPSO stage, as shown in Fig. 6.12. Furthermore, the PR stage is shown in Fig. 6.13.

As shown in Fig. 6.13, at the k^{th} iteration, 4 particles are employed and the highest value of 4 particle powers at the current iteration is defined as $hv^{(k)}$. Furthermore, the particle whose power is $hv^{(k)}$ is defined as $Par_{hv}^{(k)}$. Therefore, the highest value point of the k^{th} iteration is $(Par_{hv}^{(k)}, hv^{(k)})$. Furthermore, the local maximum from the initial iteration to the current iteration is marked as $LM^{(k)}$. Suppose at the k^{th} iteration, the highest value is equal to the local maximum, namely $hv^{(k)} = LM^{(k)}$, the local maximum can be expressed as $(Par_{LM}^{(k)}, hv^{(LM)})$ with $Par_{LM}^{(k)} = Par_{hv}^{(k)}$.

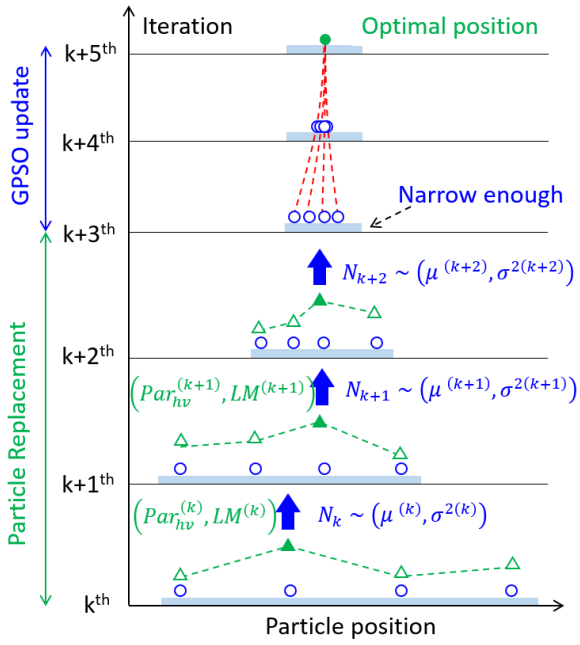

FIGURE 6.13: Particle replace process with iterations.

Therefore, the local maximum can be updated based on the highest value at the k^{th} iteration.

(1) When $hv^{(k)} \geq LM^{(k-1)}$

$$LM^{(k)} = hv^{(k)} \tag{6.34}$$

$$Par_{LM}^{(k)} = Par_{hv}^{(k)} \tag{6.35}$$

(b) When $hv^{(k)} < LM^{(k-1)}$

$$LM^{(k)} = LM^{(k-1)} \tag{6.36}$$

$$Par_{LM}^{(k)} = Par_{LM}^{(k-1)} \tag{6.37}$$

Therefore, the Gaussian distribution expectation $\mu^{(k)}$ will be updated based on the $LM^{(k)}$ variation.

(1) When $hv^{(k)} \geq LM^{(k-1)}$

In this case, in Fig. 6.14(a) and (b), the local maximum $LM^{(k)}$ and the position $Par_{LM}^{(k)}$ should be updated according to Equ. 6.34 and 35. Because the $LM^{(k)}$ increases from $LM^{(k-1)}$, it can be concluded that the particles at the k^{th} iteration are moved toward the optimal position indicating the global maximum, marked as GM, may have not been tracked. Therefore, in this case, in order not to exclude the GM from

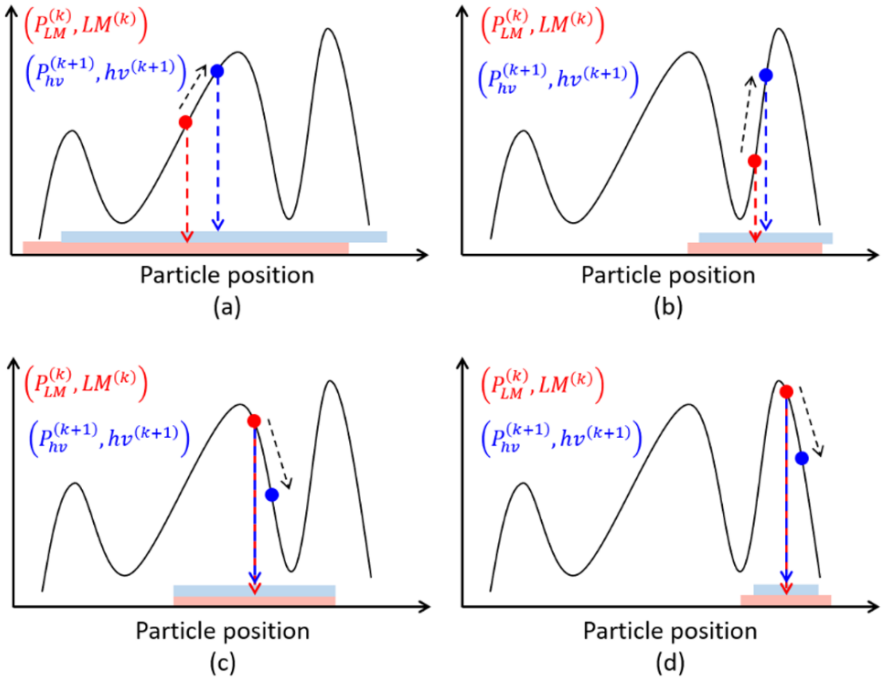

FIGURE 6.14: (a) When $hv^{(k+1)} > LM^{(k)}$ at the local peak. (b) When $hv^{(k+1)} > LM^{(k)}$ at the global peak. (c) When $hv^{(k+1)} < LM^{(k)}$ at the local peak. (d) When $hv^{(k+1)} < LM^{(k)}$ at the global peak.

the particle range, the Gaussian distribution variance $\sigma^{2(k)}$ cannot be reduced. In this way, the Gaussian expectation and variance updates are obtained as follows.

$$\mu^{(k)} = Par_{LM}^{(k)} \tag{6.38}$$

$$\sigma^{2(k)} = \sigma^{2(k-1)} \tag{6.39}$$

(2) When $hv^{(k)} < LM^{(k-1)}$

As shown in Fig. 6.14(c) and (d), in this case, the local maximum $LM^{(k)}$ and the position $Par_{LM}^{(k)}$ should be kept same according to Equ. 6.36 and 37. Because $hv^{(k)} < LM^{(k-1)}$, there is a probability that the current local maximum $LM^{(k)}$ is the GM. If $LM^{(k)}$ is not the GM in Fig. 6.14(c), both the Gaussian expectation $\mu^{(k)}$ and variance $\sigma^{2(k)}$ should not be changed. Namely, Equ. 6.40 and 41 can be obtained.

$$\mu^{(k)} = Par_{LM}^{(k)} \tag{6.40}$$

$$\sigma^{2(k)} = \sigma^{2(k-1)} \tag{6.41}$$

However, if $LM^{(k)}$ is the GM in Fig. 6,14(d), for the $k+1^{th}$ iteration, the Gaussian distribution expectation $\mu^{(k)}$ should be kept at $Par_{LM}^{(k)}$. Furthermore, to reduce the particle range to move the particles toward the GM, the variance $\sigma^{2(k)}$ should be reduced. Therefore, the Gaussian expectation and variance updates are obtained as follows.

$$\mu^{(k)} = Par_{LM}^{(k)} \tag{6.42}$$

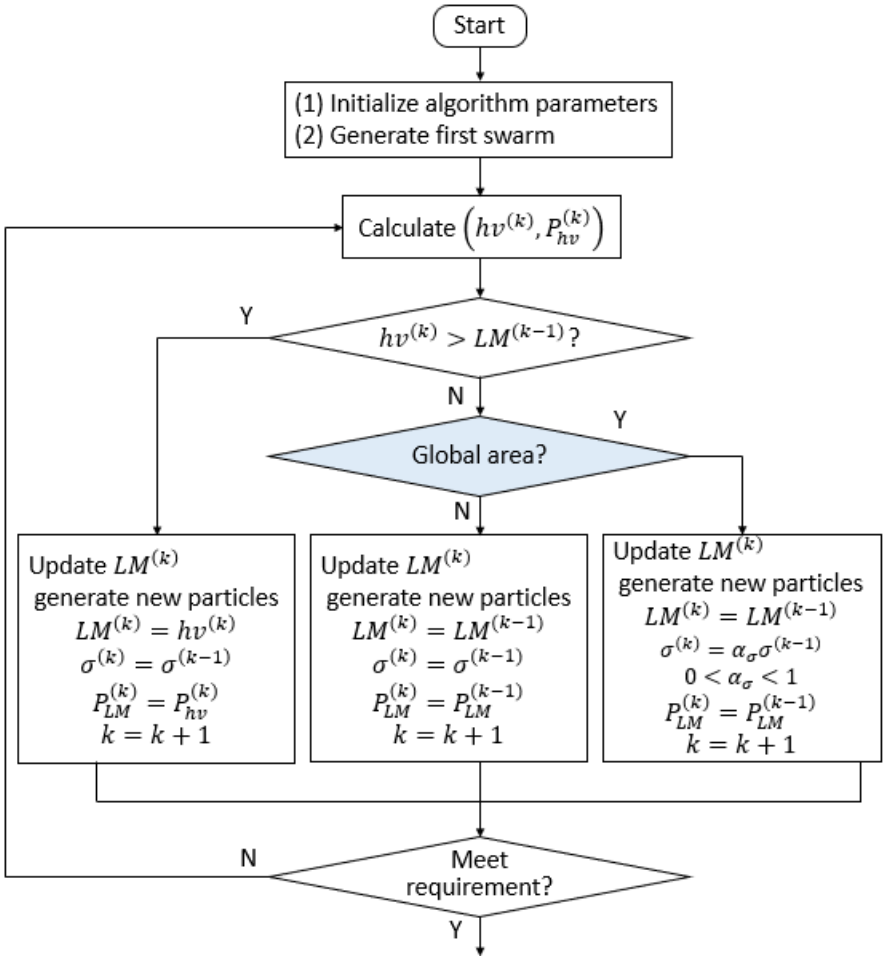

FIGURE 6.15: Flowchart of proposed particle replace stage.

$$\sigma^{2(k)} = \beta\sigma^{2(k-1)}, \beta \in (0,1) \tag{6.43}$$

Based on the above analysis, no matter whether $hv^{(k)}$ is higher than $LM^{(k-1)}$ or not, the Gaussian distribution expectation should be $LM^{(k)}$. Furthermore, the Gaussian distribution variance $\sigma^{2(k)}$ is related to whether the current local maximum $LM^{(k)}$ is the GM. The PR stage flowchart is shown in Fig. 6.15. Because only when $LM^{(k)}$ is the GM can the Gaussian distribution variance be reduced, the GM detection is the key factor which determines the algorithm accuracy and processing time.

6.2.5 Global Peak Detection Analysis

6.2.5.1 Countdown Method

In this section, the conventional countdown method is employed. In this method, if the local maximum LM^k is equal to the global maximum GM, namely $LM^k = GM$, no matter where the particles are regenerated for the $k + 1^{th}$ iteration, the highest value $hv^{(k+1)}$ will be still lower than LM^k, namely $hv^{(k+1)} < LM^k$. In the employed countdown method, with $hv^{(k+1)} < LM^k$, the following iterations without Gaussian distribution parameters changed will be conducted, and the consecutive times that the highest value is lower than the local maximum will be counted and defined as c_d.

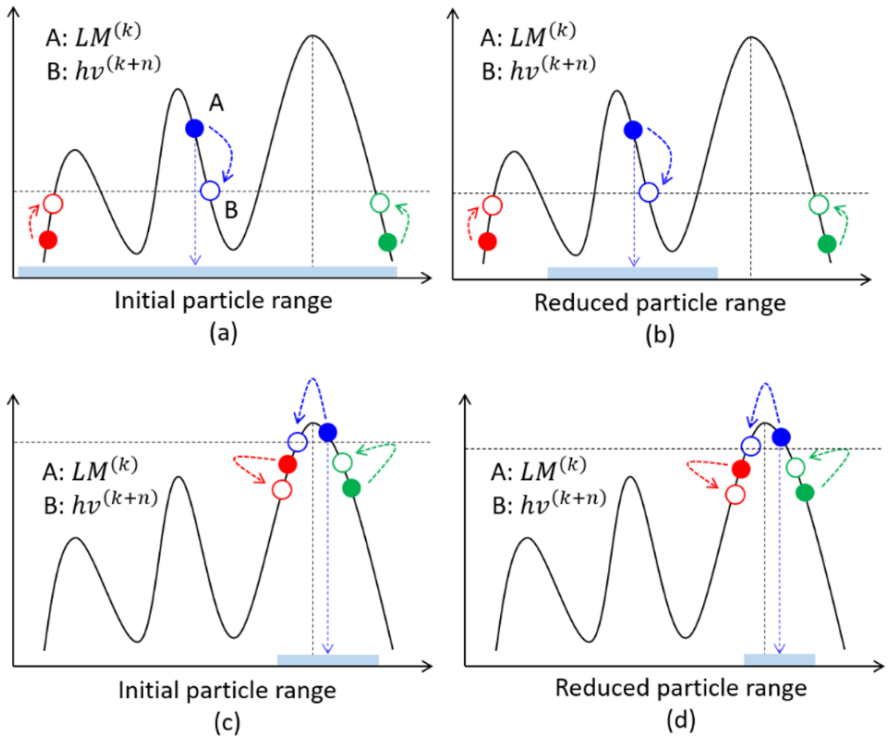

FIGURE 6.16: (a) When $hv^{(k+n)} < LM^{(k)}$ at the starting steps. (b) Particle range is reduced at the starting steps. (c) When $hv^{(k+n)} < LM^{(k)}$ at the ending steps. (d) Particle range is reduced at the ending steps.

If the parameter c_d is higher than the preset parameter, namely $c_d > c_{d0}$, the current local maximum will be taken as the GM and the Gaussian distribution variance will be reduced. However, if before the c_{d0} is approached, the highest value which is higher than the local maximum appears, the Gaussian distribution parameters will be updated according to Equ. 6.40 and 41. The flowchart is shown in Fig. 6.17.

Based on the above analysis, the preset factor c_{d0} should be carefully determined because a high c_{d0} may cause unnecessary long tracking time while a low c_{d0} may lead to real global maximum tracking mistake. For example, in Fig. 6.16(a), when the algorithm is at the beginning stage, the particles are scattered in the particle range. Even though the highest value $hv^{(k)}$ has been lower than the local maximum $LM^{(k)}$ for c_{d0} times, the particle range should not be reduced because the global maximum GM has not been tracked. However, in Fig. 6.16(c), when the algorithm is at the ending stage, almost all the particles have moved around the optimal position and even though $hv^{(k)}$ drops from $LM^{(k-1)}$ for only 1 time, the particle range should be reduced to accelerate the particle convergence. If the system still waits for the c_{d0} counting, the tracking process will cost too much unnecessary time.

6.2.5.2 Simulated Annealing Method

As analyzed in the above section, inappropriate c_{d0} value will cause unnecessary tracking time, and then in this section, a SA method is proposed for the global peak detection. In fact, the carefully tuned c_{d0} can not be suitable for all the PV working properties. For example, when the solar irradiance changes, that the preset c_{d0} is still feasible for the changed PV output property should be focused. The SA algorithm is

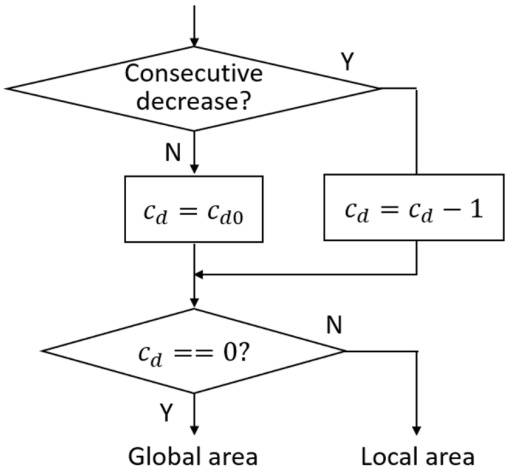

FIGURE 6.17: Flowchart of countdown method.

introduced in chapter5, and in this part, the PV output power is taken as the system energy. The probability can be obtained as follows.

$$P_{sa} = \exp\left(\frac{P_{pv}^{(k)} - P_{pv}^{(k-1)}}{\alpha_T^k T_{ini}}\right) \tag{6.44}$$

In Equ. 6.44, $P_{pv}^{(k)}$ and $P_{pv}^{(k-1)}$ are the PV output power at the k^{th} and $k-1^{th}$ iterations, respectively. Furthermore, $\alpha_T \in (0,1)$. P_{sa} is the probability that the current local maximum is not the global maximum. Therefore, the probability P_{GM} that the current LM is the GM can be obtained as follows.

$$P_{GM} = 1 - P_{sa} \tag{6.45}$$

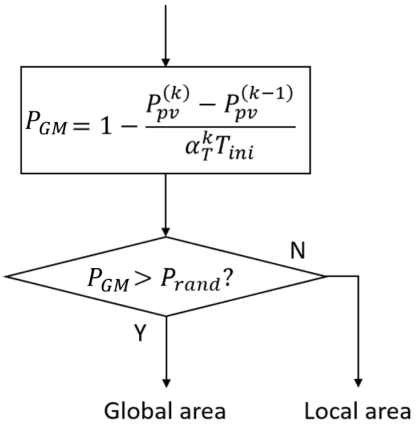

FIGURE 6.18: Flowchart of proposed simulated annealing method.

Therefore, the SA flowchart is shown in Fig. 6.18.

6.2.6 Experiment Verification of Proposed Method

The proposed algorithm is named as the PR-GPSO and SA-PR-GPSO, and the structures are shown in Fig. 6.19. Furthermore, in order to verify the proposed algorithm,

TABLE 6.2: Employed 2-peak, 3-peak and 3-peak PV property parameters.

Case	V_{oc}/V	I_{sc}/A	V_{opt}/V	I_{opt}/A	P_{max}
1	31.29	3.16	27.67	1.77	48.98
2	40.34	2.96	24.40	1.95	47.58
3	43.75	2.84	30.45	1.61	49.02

the 2-peak, 3-peak and 4-peak PV curves in Fig. 6.20-22 and Tab. 6.2 are employed in this research.

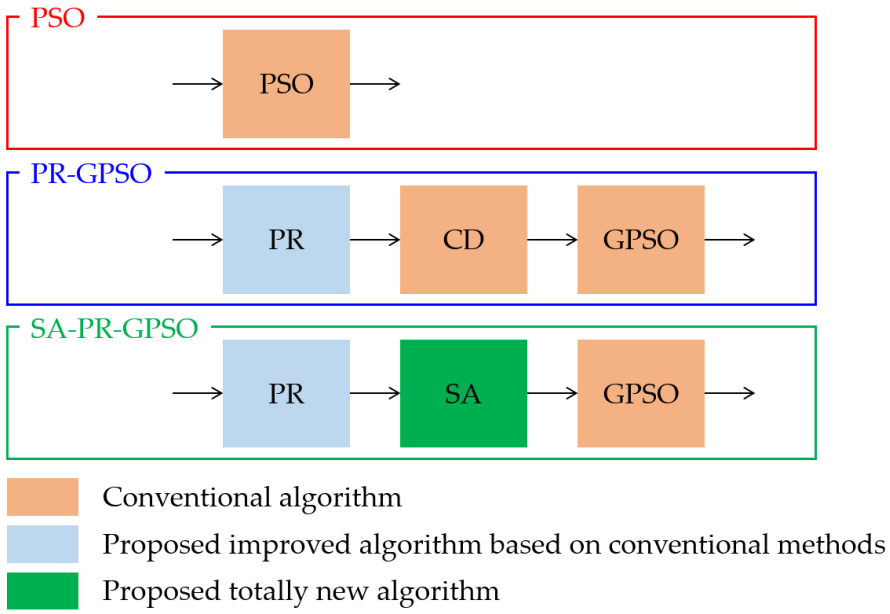

FIGURE 6.19: Employed algorithm structures.

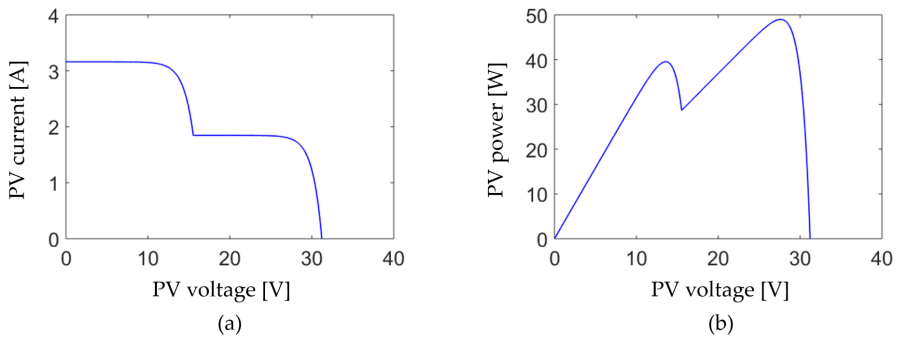

FIGURE 6.20: Employed 2-peak PV output property.

In the experiment, the parameters of employed PSO, PR-GPSO and SA-PR-GPSO algorithms are defined as follows. In the PSO algorithm, the inertia weight, personal best factor and global best factor are set as: $w = 0.4$, $c_1 = 0.2$ and $c_2 = 2$, respectively. In the PR-GPSO algorithm, the Gaussian distribution variance and countdown standard are defined to be $\sigma^2 = 0.1$ and $c_{d0} = 4$, respectively. Furthermore, in the second GPSO stage, the personal best factor global best factor are set as: $g_1 \sim N(0.2, 0.1)$

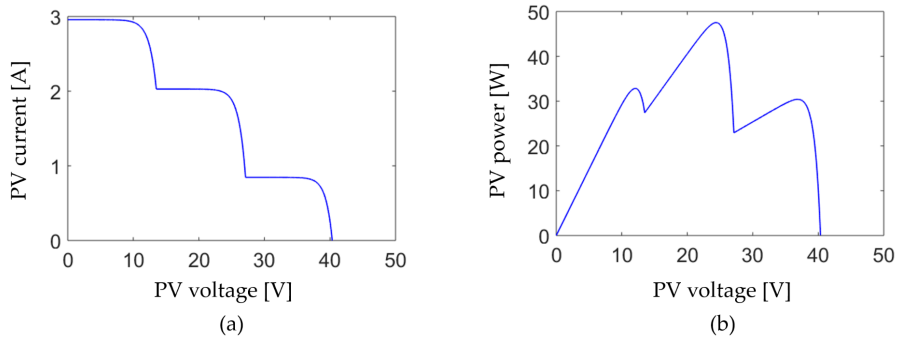

FIGURE 6.21: Employed 3-peak PV output property.

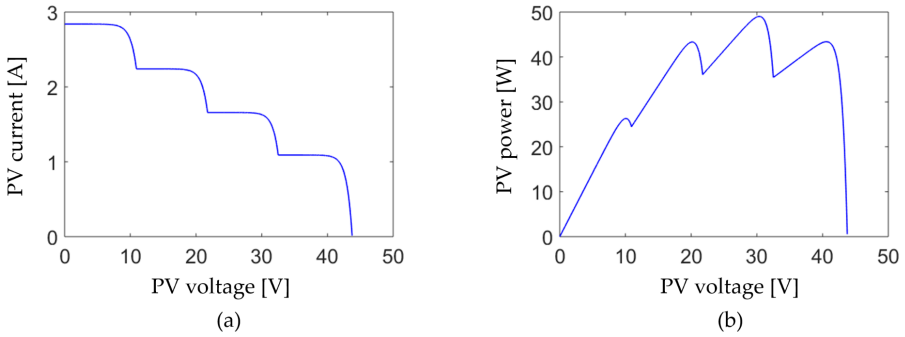

FIGURE 6.22: Employed 4-peak PV output property.

and $g_2 \sim N(2, 0.1)$, respectively. In the SA-PR-GPSO algorithm, the SA initial temperature and temperature decrease factor are defined to be $T_{ini} = 10$ and $\alpha_T = 0.1$, respectively. The final temperature is defined as the value when the system probability meets the condition of $P_{GMPP} > 0.95$. The following GPSO stage parameters are the same with them of the PR-GPSO algorithm. Furthermore, there are 4 particles employed in the algorithms, and the initial duties are defined to be 0.1, 0.4, 0.7 and 0.9, respectively. In the PSO and GPSO algorithms, the duty step maximum length is defined to be 0.02 and all the algorithms are conducted at $f_{al} = 3.3Hz$.

Based on the employed PV properties and algorithms, the MPPT experiment results of 2-peak, 3-peak and 4-peak curves are shown in Fig. 6.23-31.

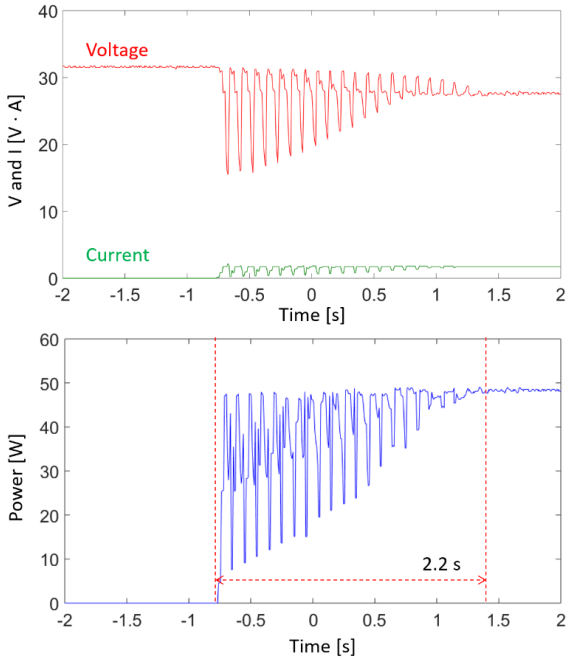

FIGURE 6.23: Experiment results of 2-peak: PSO algorithm.

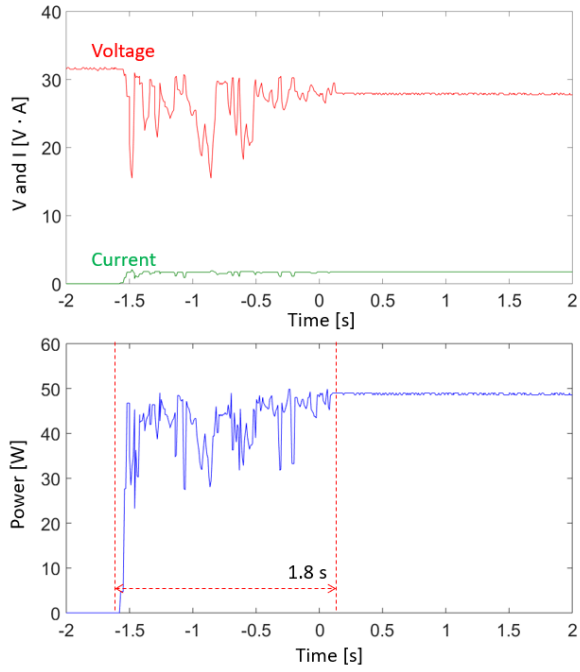

FIGURE 6.24: Experiment results of 2-peak: PR-GPSO algorithm.

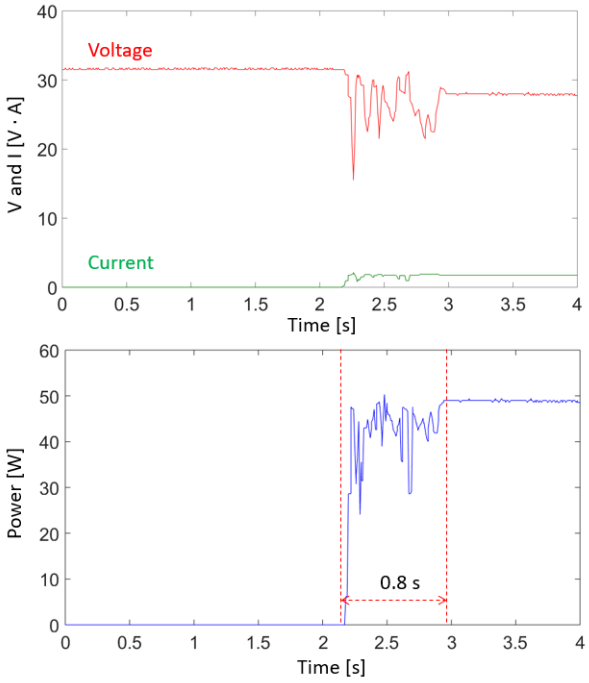

FIGURE 6.25: Experiment results of 2-peak: SA-PR-GPSO algorithm.

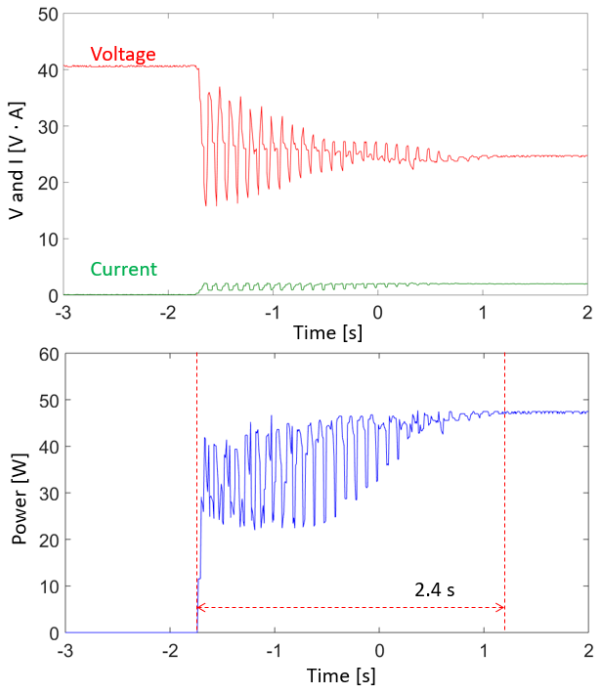

FIGURE 6.26: Experiment results of 3-peak: PSO algorithm.

In the 2-peak case as shown in Fig. 6.23-25, it can be concluded that all the employed PSO, PR-GPSO and SA-PR-GPSO algorithms have achieved the global MPPT tracking. The tracking time T_{tra} of 2-peak, 3-peak and 4-peak cases are 2.2 s, 1.8 s and 0.8 s for the PSO, PR-GPSO and SA-PR-GPSO algorithms, respectively. The tracking accuracy A_{tra} of 3 algorithms are 98.8%, 99.0% and 99.2%, respectively. However, there is an intense PV output power fluctuation in the PSO tracking experiment, and this is because the particle position in the PSO algorithm are updated step-by-step

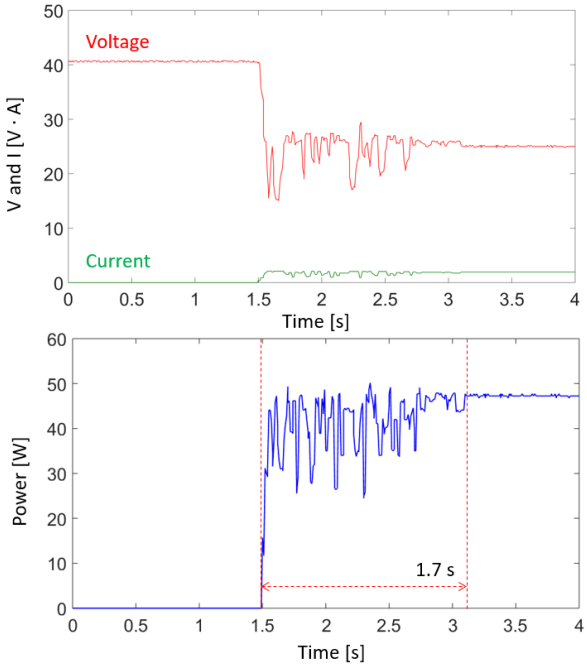

FIGURE 6.27: Experiment results of 3-peak: PR-GPSO algorithm.

under working conditions. Therefore, when the particle switches in the algorithm at one iteration, the converter duty will be changed abruptly and then the PV output power will fluctuate intensely.

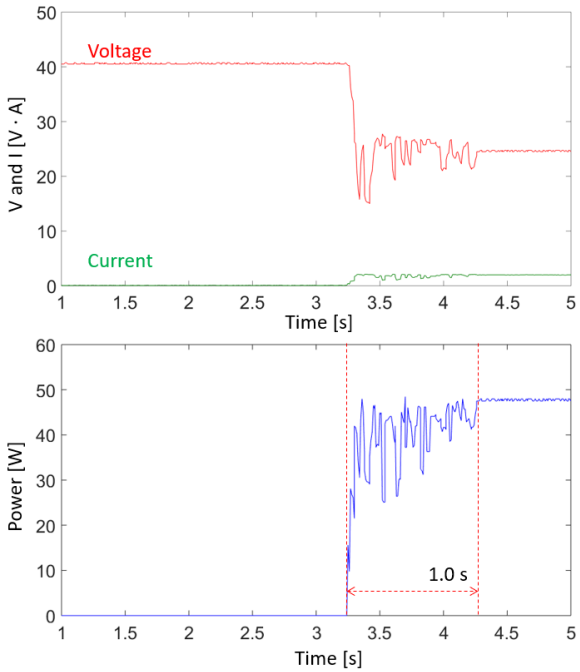

FIGURE 6.28: Experiment results of 3-peak: SA-PR-GPSO algorithm.

However, in the PR-GPSO algorithm, because the particle position update is achieved by Gaussian distribution, the step-by-step update can be avoided. Therefore, even though the particle switches at one iteration, because the particle duties are near to each, there will be no intense PV output power fluctuation. Comparing

the PR-PSO and SA-PR-PSO algorithms, the tracking process time has been effectively reduced. This is because the employed SA method can avoid the extra tracking time in the conventional countdown method.

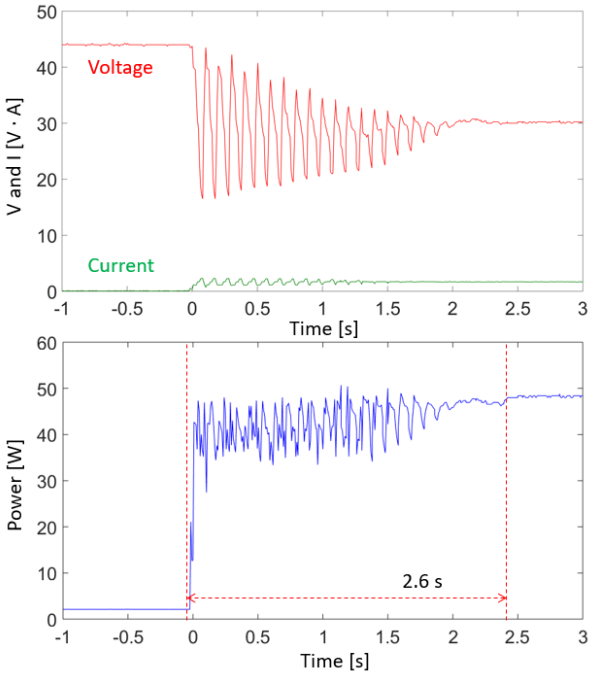

FIGURE 6.29: Experiment results of 4-peak: PSO algorithm.

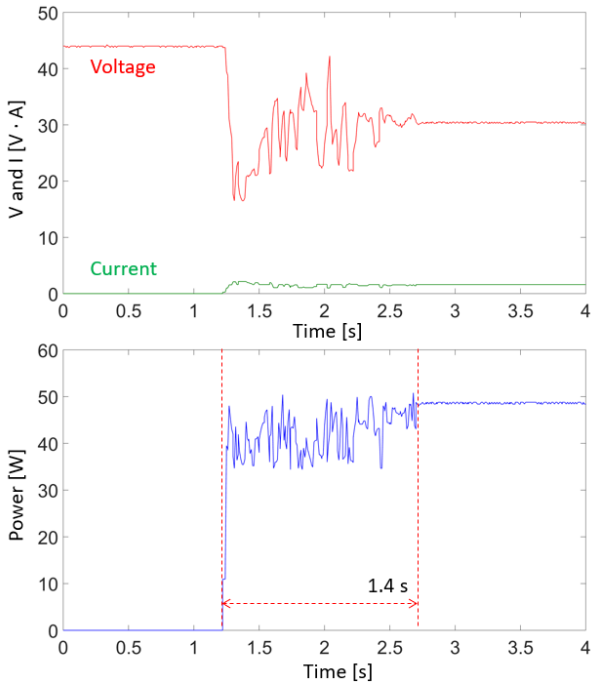

FIGURE 6.30: Experiment results of 4-peak: PR-GPSO algorithm.

In the 3-peak case as shown in Fig. 6.26-28, the tracking time T_{tra} of PSO, PR-GPSO and SA-PR-GPSO algorithms are 2.4 s, 1.7 s and 1.0 s, respectively. The tracking accuracy A_{tra} of 3 methods are 98.8%, 99.0% and 99.2%, respectively.

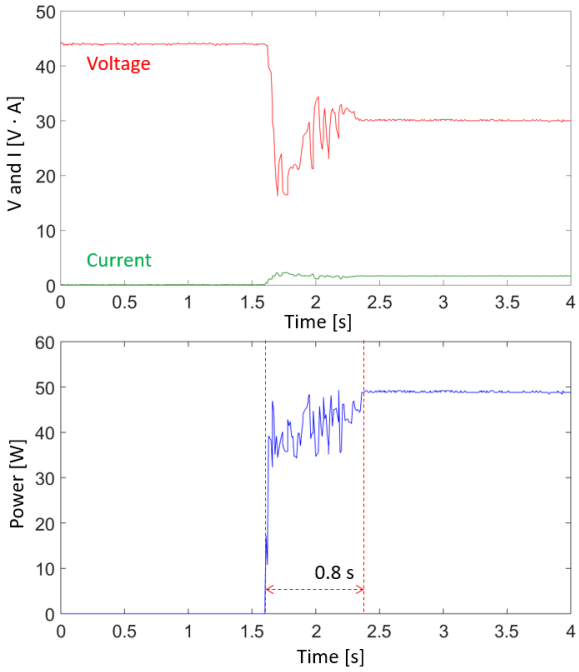

FIGURE 6.31: Experiment results of 4-peak: SA-PR-GPSO algorithm.

In the 4-peak case as shown in Fig. 6.29-31, the tracking time T_{tra} of PSO, PR-GPSO and SA-PR-GPSO algorithms are 2.6 s, 1.4 s and 0.8 s, respectively. The tracking accuracy A_{tra} of 3 methods are 98.5%, 99.1% and 99.3%, respectively.

Based on the above experiment results, the proposed SA-PR-GPSO feasibility has been verified.

6.3 Particle Jump Particle Swarm Optimization Algorithm

In the conventional PSO algorithm, the particle movement is conducted based on Equ. 6.8 and 6.9. For example, for the PV MPPT tracking, there are 4 particles employed in the conventional PSO algorithm as shown in Fig. 6.32.

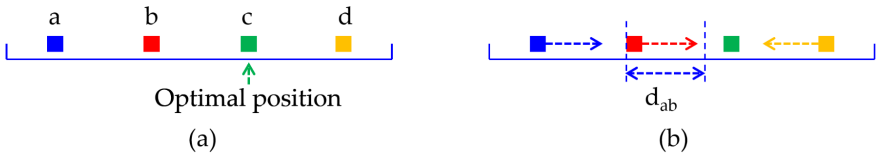

FIGURE 6.32: Tracking process of conventional PSO algorithm.

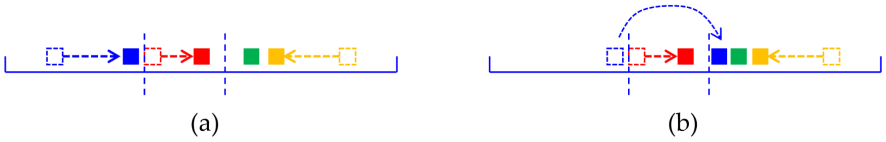

FIGURE 6.33: Tracking process of proposed particle jump principle.

Based on Fig. 6.32(a), suppose the particle c is the at the optimal position. In the tracking process, the other particles a, b and d should move toward the optimal position c to track the global maximum. The tracking process is shown in Fig. 6.32(b). Both the particle a and b move toward the optimal position and the traversals of particle a and b can be regarded as subsequent in time domain. Suppose the traversal of particle b is the former one and that of particle a is the latter one. The interval d_{ab} between the particle a and b has been firstly traversed by particle b, indicating there is no potential global maximum position. Therefore, the latter particle a traversal can be seen as invalid for d_{ab}. It can be hypothesized that if the latter particle a traversal can be avoided, the whole tracking process time will be reduced as shown in Fig. 6.33.

6.3.1 Particle Jump Method Analysis

In this section, a particle jump (PJ) PSO method has been proposed. Similar to the previous proposed SA-PR-GPSO algorithm, the proposed method whole tracking process is also divided into two stages. The first stage is conducted by the particle jump method to achieve the fast particle convergence and the second stage is carried out with PSO algorithm to track the accurate global maximum position.

The PJ process is shown in Fig. 6.34-41.

Step 1: There are 4 particles and 4 intervals employed in the proposed PJ method. The 4 particles are placed at the centers of 4 intervals, respectively, and each particle is arranged with a Gaussian distribution to generate the future position. The Gaussian distribution initial parameters are defined as follows: $\mu_a = a, \mu_b = b, \mu_c = c, \mu_d = d$ and $\sigma_a^2 = \sigma_b^2 = \sigma_c^2 = \sigma_d^2$, indicating the employed Gaussian distributions share the same variances as shown in Fig. 6.34.

Step 2: According to Fig. 6.35, with the initial 4 particle positions, the power of each particle is obtained at the initial iteration. Based on the 4 power data, the local maximums LMs and global maximum GM can be determined. The particle c and power P_c are supposed to be the optimal position and GM, respectively. Furthermore, the powers of P_a, P_b and P_d of particle a, b and d are the LMs of interval

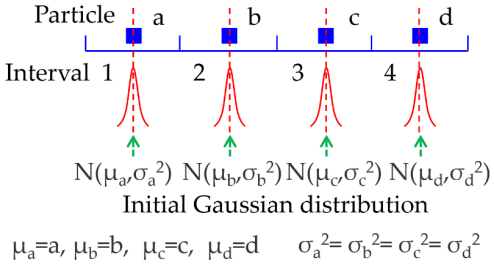

FIGURE 6.34: Step 1.

1, 2 and 4, respectively. For particle c, $LM_3 = GM$. Each Gaussian distribution expectation is set as the LM, respectively.

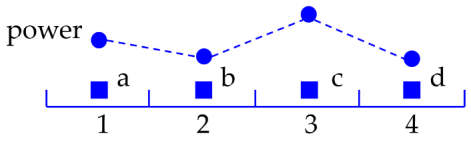

FIGURE 6.35: Step 2.

Step 3: Because the GM belongs to the particle c in the interval 3, the potential optimal position should be explored in the interval 1, 2 and 4, respectively. In order to search the potential position with higher probability, the search range should be widened. In this paper, the search range widening is conducted on the Gaussian distribution variance increase. For example, as shown in Fig. 6.36, the variance of Gaussian distribution $N_c(\mu_c, \sigma_c^2)$ is kept still while the other variances are increased correspondingly.

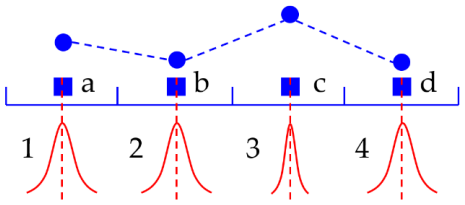

FIGURE 6.36: step 3.

Step 4: The particles for the next iterations are regenerated based on the updated Gaussian distribution respectively in Fig. 6.37. With higher σ_a^2, σ_b^2 and σ_d^2, the new particles a, b and d can explore more widely in the corresponding intervals.

Step 5: With the new particles at this iteration, all the particle powers are also calculated. Comparing the current powers with the previous data, the LMs and GMs should be updated as shown in Fig. 6.38.

Step 6: Based on the updated GM and LM data, the Gaussian distribution variance of the particle which GM belongs to should be kept still and the other variances should be further increased. For example, as shown in Fig. 6.39, because the particle power P_a, P_b and P_d are not the GM, the variances σ_a^2, σ_b^2 and σ_d^2 will be further increased to obtain more scattered particles for the next iteration. Furthermore, the expectations μ_a, μ_b and μ_d are updated with the LM_1, LM_2 and LM_4, respectively.

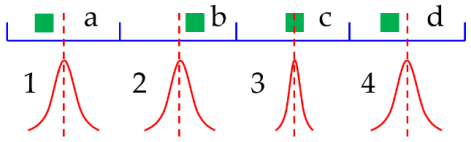

FIGURE 6.37: Step 4.

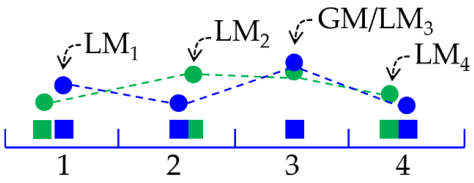

FIGURE 6.38: Step 5.

With the updated Gaussian distribution parameters, the algorithm will go back to the step 4 to conduct the potential optimal position searching process.

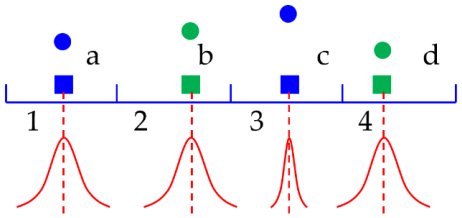

FIGURE 6.39: Step 6.

Step 7: Based on the loop conduction from the step 4 to 6, the Gaussian distribution variances of the particles whose powers are not the GM will be consecutively increased. Therefore, there will be an iteration at which the potential optimal position searching process has been conducted for long enough time, and for some interval (for example, interval 1), there is no position found at which the PV power is higher than the current tracked GM. Therefore, it can be regarded that there is no potential optimal position in this interval and it should be discarded. The particle which is in the interval to be discarded should jump to the interval where the current tracked GM is. For example, in Fig. 6.40, the particle a jumps into the interval 3 and the interval 1 is discarded.

With particle a jumping into the interval 3, the corresponding Gaussian distribution also should be updated. Because both particle a and c are in the interval 3, the Gaussian distribution variances should follow the equation of $\sigma_a^2 = \sigma_c^2$. The expectations μ_a and μ_c should be set as the particle positions, respectively.

Step 8 and 9: With above steps, the interval 1 is discarded by the particle a and it jumps into the interval where the current tracked GM is. Repeat the above steps for enough times, the rest particles will also jump into the current tracked GM interval. For example, in this paper, particle b and d will jump into interval 3 after enough iterations as shown in Fig. 6.41.

With the above steps of 1-9, the employed particles will jump into the same interval where the current tracked GM is. At the time when all the particles jump into the same interval, the PJ stage will be ended and the following PSO stage will start. The PJ stage is employed to accelerate the particle convergence and the following PSO

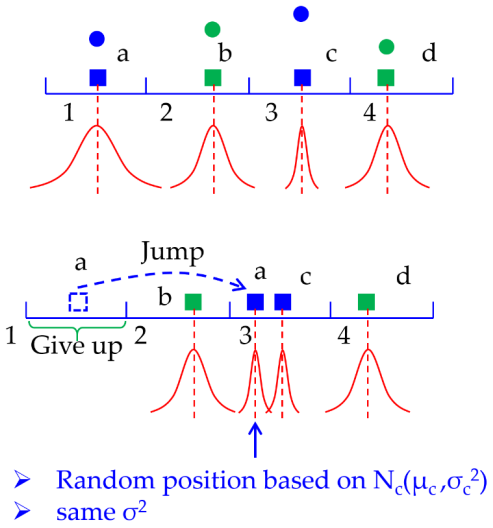

FIGURE 6.40: Step 7.

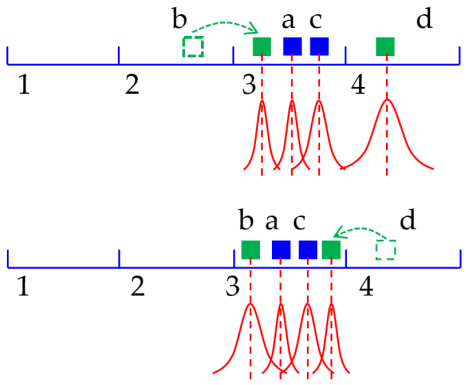

FIGURE 6.41: Step 8 and 9.

stage will do the precise global maximum positioning. Compared with the conventional PSO algorithm, the proposed two-stage PJ PSO algorithm can achieve faster global maximum tracking performance.

6.3.2 Particle Jump Determination Analysis

Based on the above analysis, when there is no potential position at which the particle power is higher than the current tracked global maximum *GM* in another interval, the corresponding particle should jump away from the current interval to the one where the current tracked *GM* is. However, whether the particle should jump or not should be determined by the algorithm. In this section, the following 2 methods are proposed.

6.3.2.1 Variance Increase Method

In the PJ stage, the particle variance will be increased if the particle power is not higher than the current tracking *GM*. Therefore, an intuitive determination standard

can take the Gaussian distribution variance into consideration. In this section, a variance increase method is proposed and the flowchart is shown in Fig. 6.42.

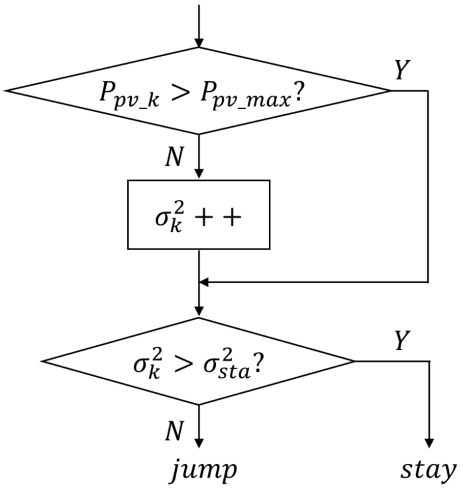

FIGURE 6.42: Flowchart of variance increase method.

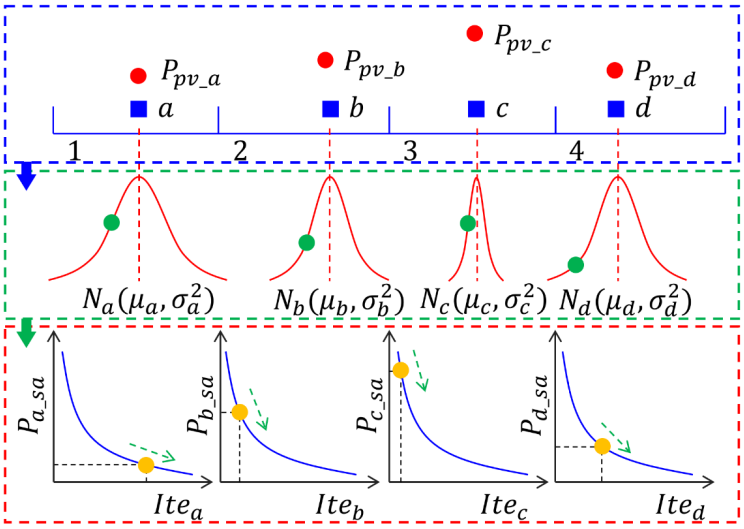

FIGURE 6.43: Simulated module arranged to each particle.

Before the algorithm starts, an upper limit σ_{sta}^2 can be set for the variance increase method. After a certain iterations, when the variance of some particle is higher than σ_{sta}^2, the corresponding interval can be seen to have been traversed for enough times and there is no potential position at which the particle power can exceed the current tracked GM. Therefore, the particle should discard the corresponding interval and jump to the GM interval. For the variance increase method, the simple complementation is one of the most effective advantages. However, the disadvantage is also obvious that the upper limit σ_{sta}^2 should be carefully determined. Because a too high σ_{sta}^2 will lead to the long traversal time while a too low σ_{sta}^2 will cause the misjump, indicating the potential real GM may be missed by the algorithm.

6.3.2.2 Simulated Annealing Method

In this paper, in order to determine the appropriate particle jump time and occasion, the SA method is adopted. Before the particle jumps away from some interval, the particle position update in this interval is based on Gaussian distribution. If the particle power is not the GM, the Gaussian distribution variance should be increased. As shown in Fig. 6.43, in the proposed method, a SA module is arranged to each particle. In the module, the PV output power is taken as the system energy, and then the probability function of each module can be derived.

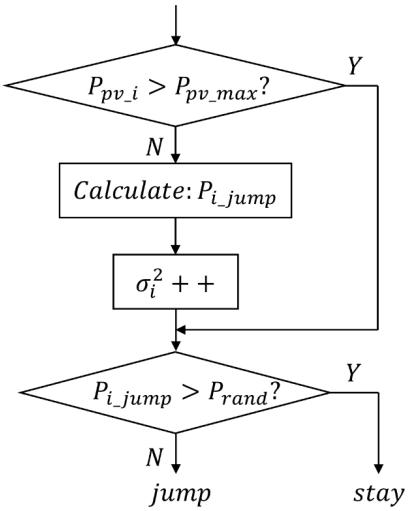

FIGURE 6.44: Flowchart of proposed simulated annealing method.

$$P_{i\_sa} = e^{\frac{P_{pv\_i} - P_{pv\_max}}{\alpha_T^{ite_i} T_{ini}}} \tag{6.46}$$

In the equation, i stands for the particle a, b, c and d; P_{pv_i} is the PV output power of particle i; P_{pv_max} is GM; ite_i is the iteration times; P_{i_sa} is the probability of that for the i^{th} particle, there is a potential position in the current interval.

In the algorithm iteration process, the particle position is the system state disturbance and the PV output power is system state energy. At each iteration, for each particle whose power cannot exceed the current tracked GM, the particle jump probability will be calculated as follows.

$$P_{i\_jump} = 1 - P_{i\_sa} \tag{6.47}$$

The proposed SA method flowchart is shown in Fig. 6.44. Therefore, with algorithm iteration conducting, for the i^{th} particle, if the PV output power P_{pv_i} is lower than the current GM, the particle jump probability P_{i_jump} will keep exponentially increase. In this way, with $P_{pv\_i} < P_{pv\_max}$ in the beginning stage, the particle i may not jump, but if it happens in the ending stage, the particle i may jump. Therefore, with the SA method, the particle jump can be determined with variant probability analysis.

6.3.3 Experiment Verification

The proposed algorithm is named as the PJ-PSO and SA-PJ-PSO, and the structures are shown in Fig. 6.45. Furthermore, in order to verify the proposed algorithm, the 2-peak, 3-peak and 4-peak PV curves in Fig. 6.20-22 and Tab. 6.2 are employed in this research.

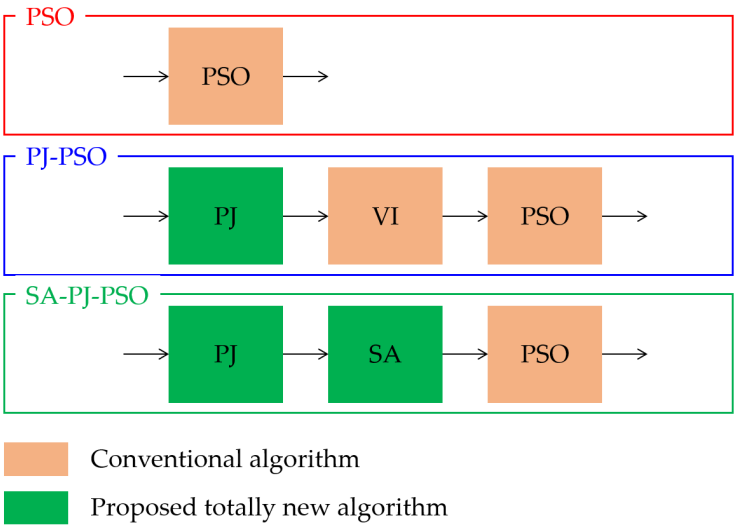

FIGURE 6.45: Employed algorithm structures.

In the experiment, the parameters of employed PSO, PJ-PSO and SA-PJ-PSO algorithms are defined as follows. In the PSO algorithm, the inertia weight, personal best factor and global best factor are set as: $w = 0.4$, $c_1 = 0.2$ and $c_2 = 2$, respectively. In the PJ-GPSO algorithm, there are 4 intervals and 4 particles employed in the particle jump stage. The interval are defined to be (0.1, 0.3), (0.3, 0.5), (0.5,0.7) and (0.7,0.9), respectively. The initial particle duties are set at the center in each interval, namely the initial particle duties are 0.2, 0.4, 0.6 and 0.8, respectively. Furthermore, for the Gaussian distribution, the initial variances are defined to be $\sigma_a^2 = \sigma_b^2 = \sigma_c^2 = \sigma_d^2 = 0.1$. In the variance increase method, the preset variance standard is defined to be $\sigma_{sta}^2 = 0.35$ and the variance increment is defined as $\delta\sigma^2 = 0.02$. The PSO stage parameters are same with the PSO algorithm. In the SA-PJ-PSO algorithm, only the SA module parameters are different from the above parameters and they are $T_{ini} = 100$ and $\alpha_T = 0.2$. The final temperature is defined as the value when the system probability meets the condition of $P_{i_{jump}} > 0.95$. In the PSO and GPSO algorithms, the duty step maximum length is defined to be 0.02 and all the algorithms are conducted at $f_{al} = 3.3Hz$.

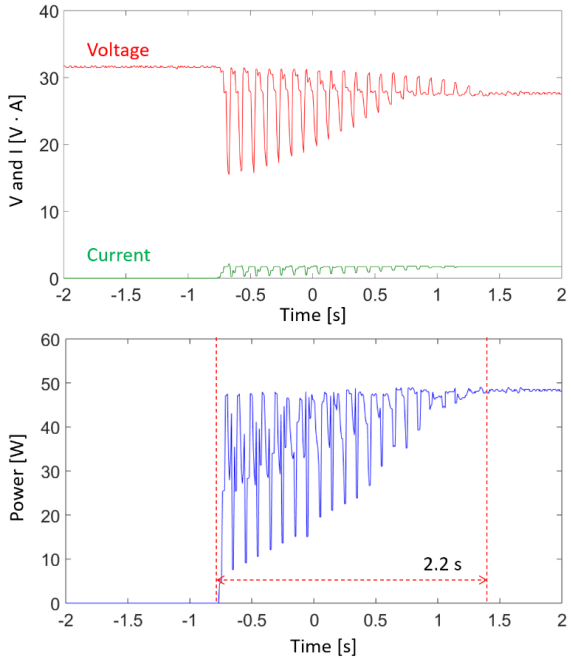

FIGURE 6.46: Experiment results of 2-peak: PSO algorithm.

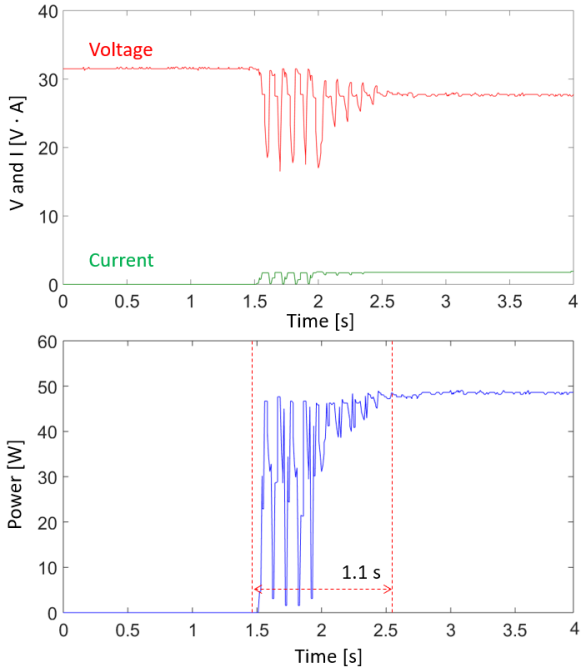

FIGURE 6.47: Experiment results of 2-peak: PJ-PSO algorithm.

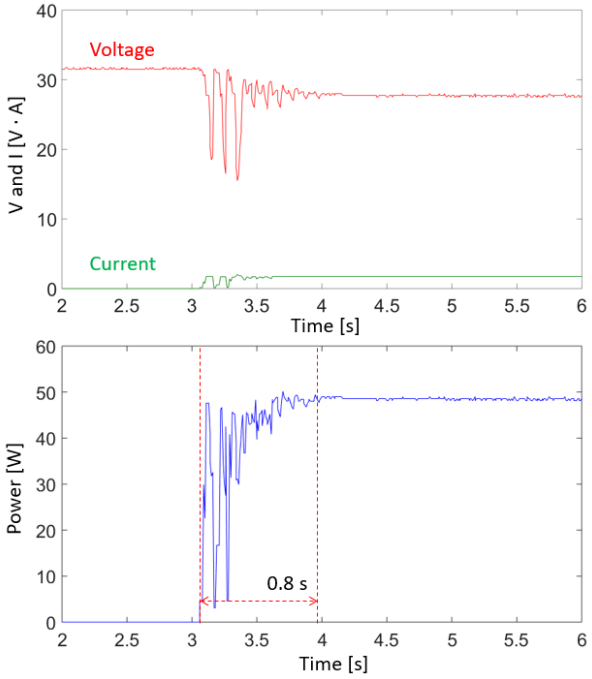

FIGURE 6.48: Experiment results of 2-peak: SA-PJ-PSO algorithm.

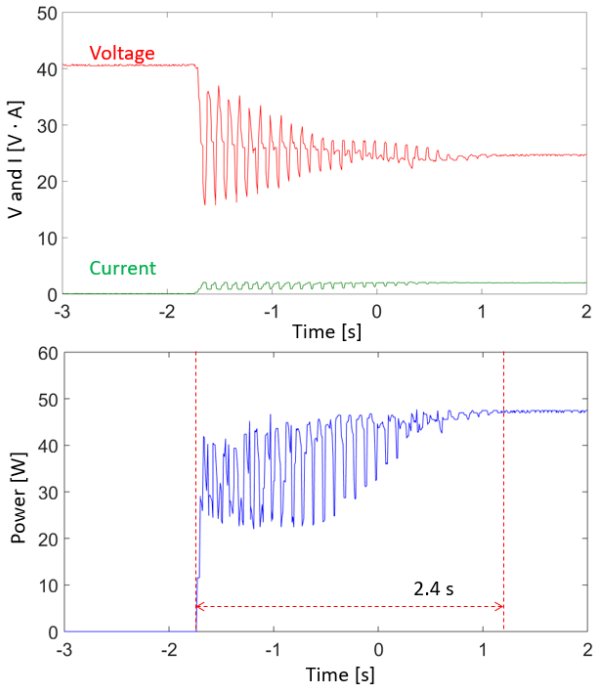

FIGURE 6.49: Experiment results of 3-peak: PSO algorithm.

Based on the employed PV properties and algorithms, the MPPT experiment results of 2-peak, 3-peak and 4-peak curves are shown in Fig. 6.46-54.

In the 2-peak case as shown in Fig. 6.46-48, it can be concluded that all the employed PSO, PJ-PSO and SA-PJ-PSO algorithms have achieved the global MPPT tracking. The tracking time T_{tra} are 2.2 s, 1.1 s and 0.8 s for the PSO, PJ-PSO and SA-PJ-PSO algorithms, respectively. The tracking accuracy A_{tra} of 3 algorithms are 98.8%, 99.2% and 99.0%, respectively. However, there is an intense PV output power

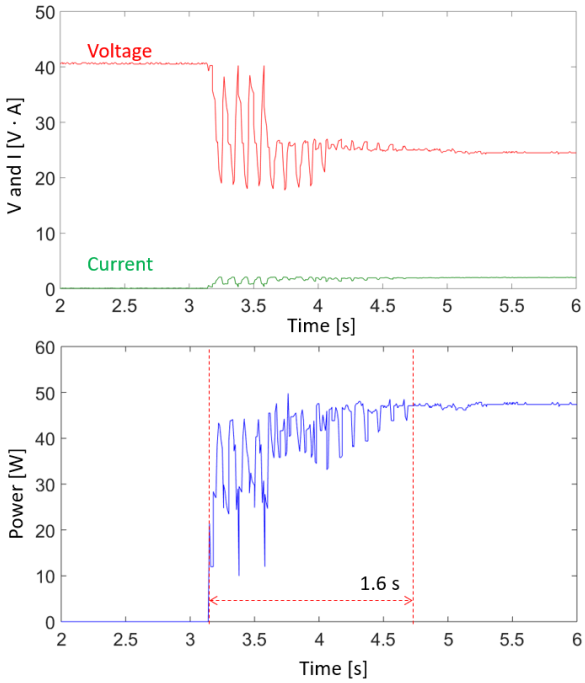

FIGURE 6.50: Experiment results of 3-peak: PJ-PSO algorithm.

fluctuation in the PSO tracking experiment, and this is because the particle position in the PSO algorithm are updated step-by-step under working conditions. Therefore, when the particle switches in the algorithm at one iteration, the converter duty will be changed abruptly and then the PV output power will fluctuate intensely.

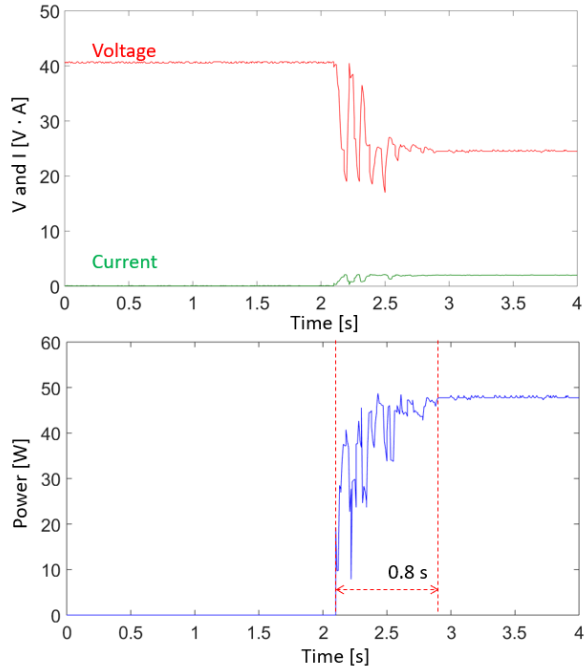

FIGURE 6.51: Experiment results of 3-peak: SA-PJ-PSO algorithm.

However, in the PJ-PSO algorithm, because the particle can jump away from the interval where there is no potential position, the fluctuation process is greatly

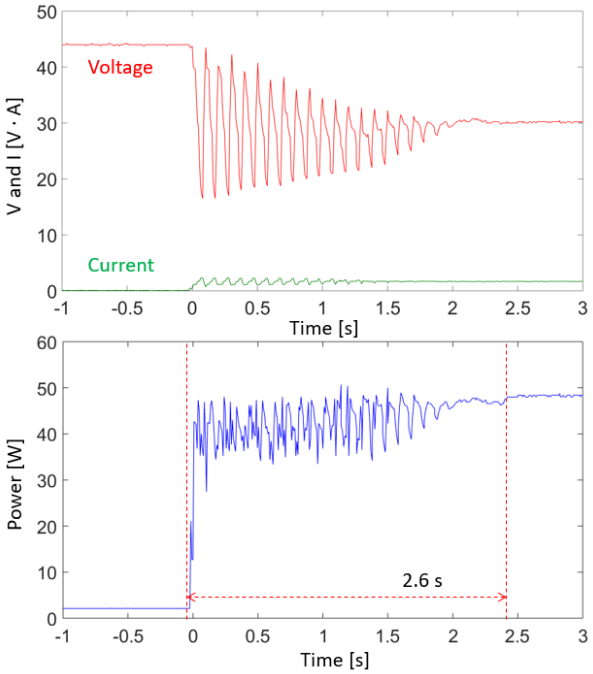

FIGURE 6.52: Experiment results of 4-peak: PSO algorithm.

reduced. Comparing the PJ-PSO and SA-PJ-PSO algorithms, the tracking process time has been effectively reduced. This is because the employed SA method can avoid the extra tracking time in the conventional variance increase method.

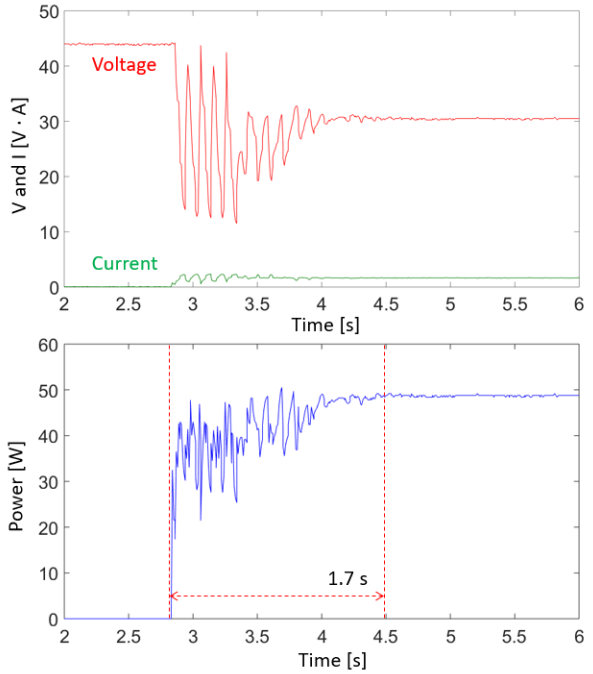

FIGURE 6.53: Experiment results of 4-peak: PJ-PSO algorithm.

In the 3-peak case as shown in Fig. 49-51, the tracking time T_{tra} of PSO, PJ-PSO and SA-PJ-PSO algorithms are 2.4 s, 1.6 s and 0.8 s, respectively. The tracking accuracy A_{tra} of 3 methods are 98.8%, 99.2% and 99.4%, respectively.

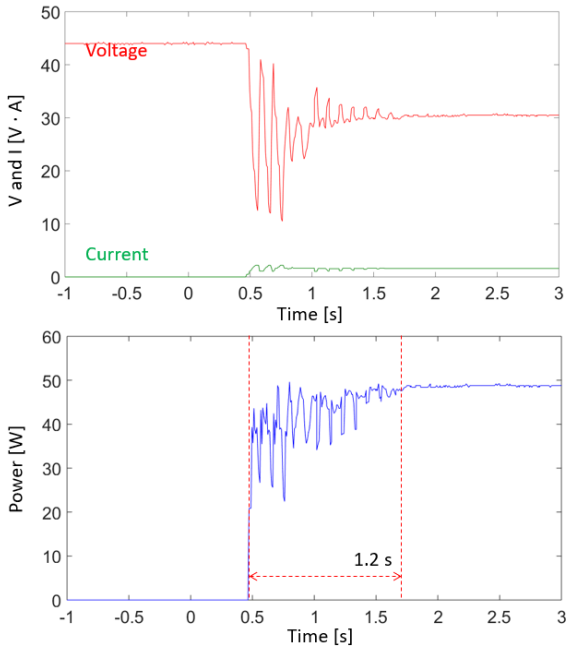

FIGURE 6.54: Experiment results of 4-peak: SA-PJ-PSO algorithm.

In the 4-peak case as shown in Fig. 52-54, the tracking time T_{tra} of PSO, PJ-PSO and SA-PJ-PSO algorithms are 2.6 s, 1.7 s and 0.8 s, respectively. The tracking accuracy A_{tra} of 3 methods are 98.5%, 99.1% and 99.3%, respectively.

Based on the above experiment results, the proposed SA-PJ-PSO feasibility has been verified.

6.4 PV MPPT Control with Sweep Method

With the above analysis, when the PV works under partial shading conditions, the global MPPT control can be achieved with the proposed SA-PR-GPSO and SA-PJ-PSO algorithms. In order to verify the proposed algorithm MPPT time improvement, in this section, the fundamental PV sweep method is taken as the control method.

In the sweep method, the MPPT converter duty is traversed from 0 to 1, and in the sweep process, both the maixmum PV power and the corresponding duty will be recorded. After the sweep process, the recorded duty will be employed by the converter and then the MPPT control can be achieved. Therefore, based on the sweep method property, it can be concluded that the sweep frequency and duty variation step are the two key factors determining the sweep performance. With the above analysis, the sweep simulations will be conducted in this section. In the following sweep simulations, the duty variation step is $d_{step} = 0.001$ and the sweep frequency is $f_{sweep} = 1kHz$.

6.4.1 Sweep Simulation with Constant PV Solar Irradiance

When the PV possesses the 2-peak and 4-peak properties, the sweep simulation results are shown in Fig. 6.55 and 56 respectively.

With the duty variation step of $d_{step} = 0.001$, the 2-peak and 4-peak PV properties are effectively restored. Therefore, after the sweep process, the optimal converter

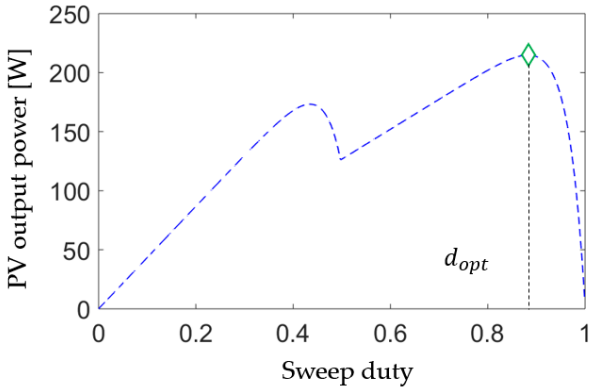

FIGURE 6.55: Sweep simulation of 2-peak PV property.

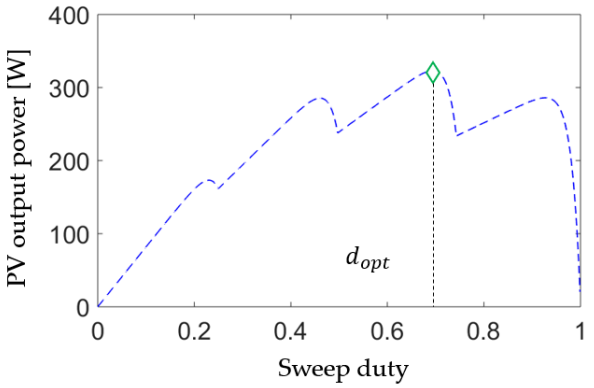

FIGURE 6.56: Sweep simulation of 4-peak PV property.

duty d_{opt} can be employed to conduct the MPPT control. In this section, because the simulation frequency is different with the experiment frequency, the MPPT time will not be focused.

With the above, it can be concluded that under partial shading conditions, when the solar irradiance on the PV is constant in the sweep process, the MPPT control can be achieved with 1-time sweep. Because the converter duty variation step is very low, the sweep frequency can be set high enough. In this way, simple implementation and fast tracking capability are the main advantages of the sweep method compared with other algorihtms.

6.4.2 Sweep Simulation with Variant PV Solar Irradiance

Under working conditions, the PV solar irradiance always changes and in this section, the PV output changes from 4-peak to 2-peak property as shown in Fig. 6.57 and 58. Suppose the solar irradiance variation happens in the sweep process, the sweep simulation result is shown in Fig. 6.59.

Before the solar irradiance variation happens, the 4-peak PV property is swept, the former 2 peaks are restored. However, when the converter duty $d_{sweep} = 0.5$, the solar irradiance changes and the 2-peak PV property will be output. In this case, the sweep process continues until $d_{sweep} = 1$. Therefore, as shown in Fig. 6.59, d_A is regarded as the optimal duty after the sweep process even though d_B is the real optimal duty. Therefore, with the false converter duty, the MPPT control will fail.

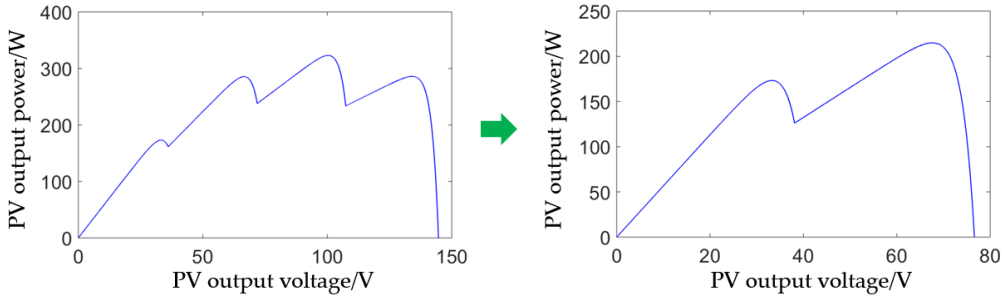

FIGURE 6.57: Variation from PV 4-peak property to 2-peak property.

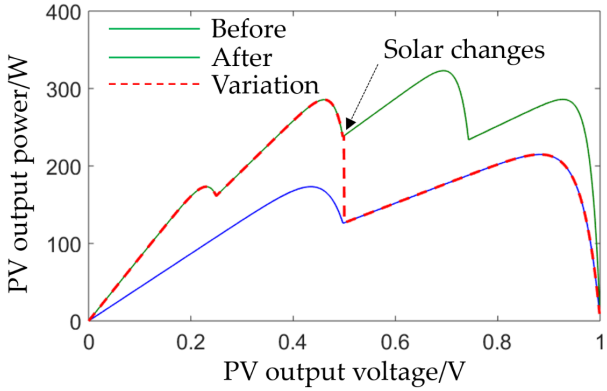

FIGURE 6.58: PV output property variation from 4 peaks to 2 peaks.

In order to achieve successful MPPT control, under working conditions, the sweep process should be conducted at least two times to avoid duty failure under partial shading conditions. For example, when the solar irradiance keeps constant in the PV MPPT sweep process, the sweep results of 2 times will be the same, namely $d_{opt1} = d_{opt2}$, as shown in Fig. 6.60 and 61.

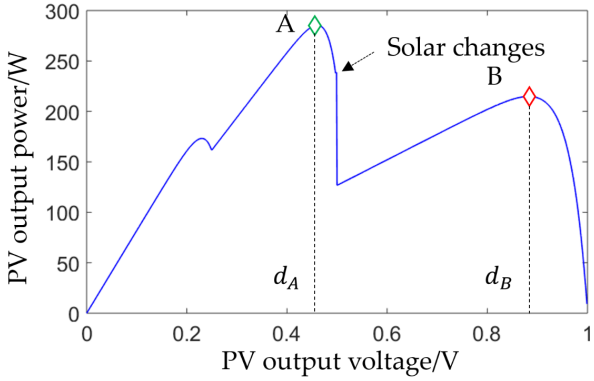

FIGURE 6.59: Sweep simulation of 4-2-peak PV property.

However, when the solar irradiance changes in the sweep process, the restored PV properties of the 2 times sweeping will be different as shown in Fig. 6.62 and 63. Therefore, in this case, a third sweeping will be required to determine the optimal duty in Fig. 6.64. Based on the sweep results, it also can be concluded that, if the solar irradiance variation further happens, the sweep process should be conducted for more times. Therefore, the MPPT time of sweep method is not only the 1-time sweep process but multiple times.

6.4.3 SA-PR-GPSO Simulation with Constant Solar Irradiance

With the above analysis, when the solar irradiance keeps constant, the sweep method can achieve the fast MPPT control under partial shading conditions. Therefore, in order to compare the sweep method and proposed SA-PR-GPSO algorithm, the SA-PR-GPSO algorithm simulation is also conducted.

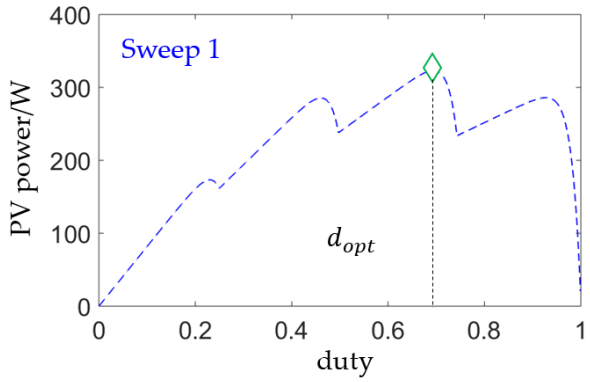

FIGURE 6.60: First sweep simulation of 2-peak PV property.

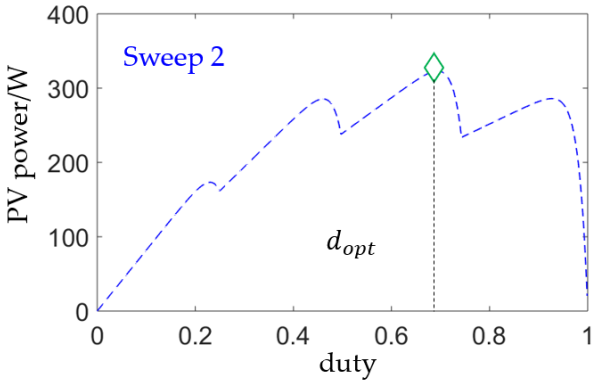

FIGURE 6.61: Second sweep simulation of 2-peak PV property.

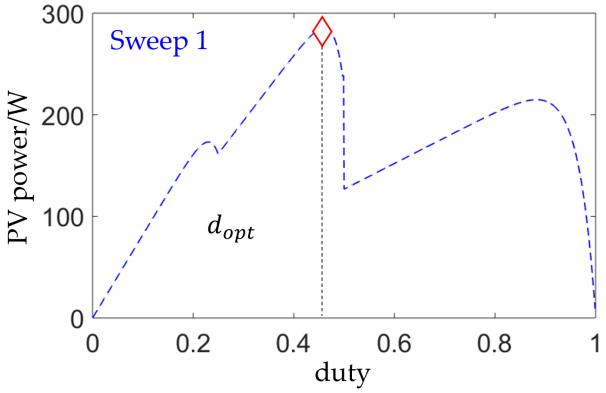

FIGURE 6.62: First sweep simulation of 4-2-peak PV property.

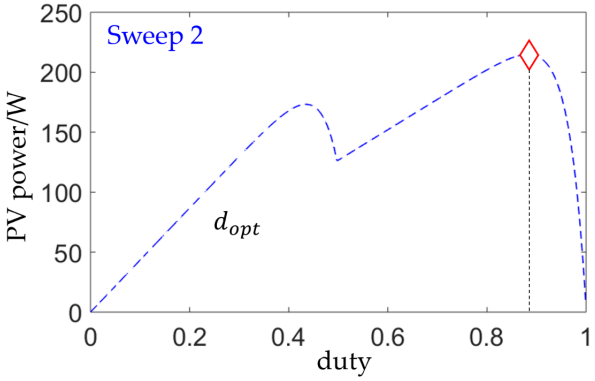

FIGURE 6.63: Second sweep simulation of 4-2-peak PV property.

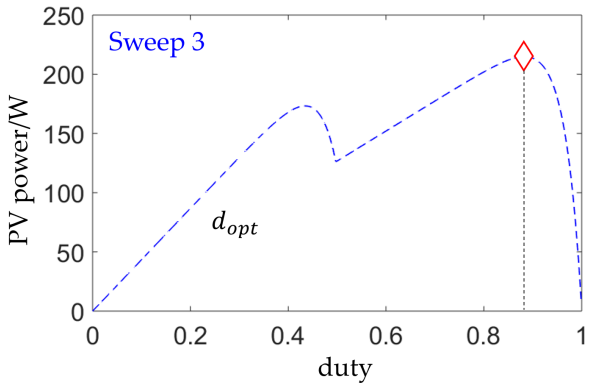

FIGURE 6.64: Third sweep simulation of 4-2-peak PV property.

In the SA-PR-GPSO algorithm, there are 4 particles employed and the initial duties are set as 0.2, 0.4, 0.6 and 0.9, respectively. Furthermore, because in the simulation, the algorithm frequency is different with that in the experiment, in this section, the MPPT iteration times will be taken as the standard to assess the MPPT performance. The 2-peak and 4-peak SA-PR-GPSO algorithm simulation results are shown in Fig. 6.65-68.

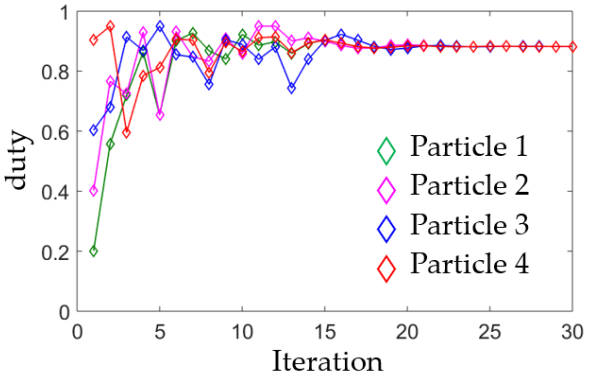

FIGURE 6.65: Duty variations of SA-PR-GPSO algorithm with 2-peak PV property.

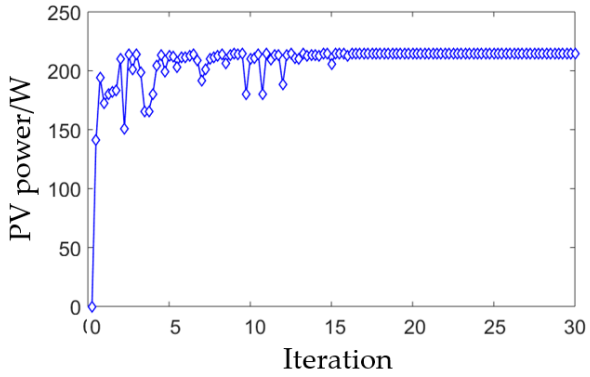

FIGURE 6.66: PV output power variation with SA-PR-GPSO algorithm with 2-peak PV property.

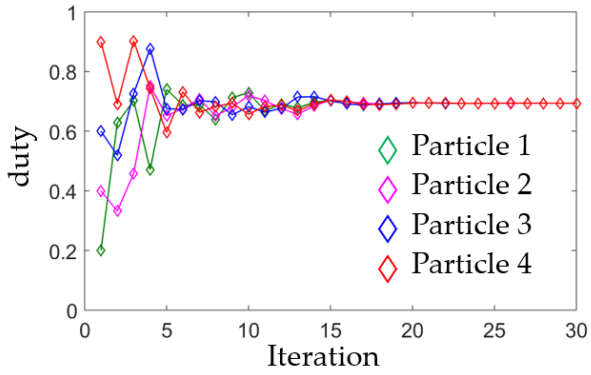

FIGURE 6.67: Duty variations of SA-PR-GPSO algorithm with 4-peak PV property.

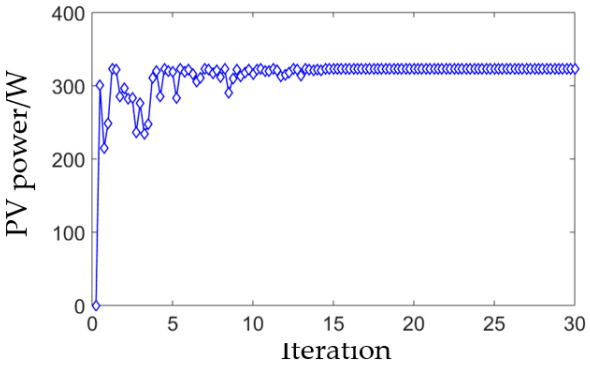

FIGURE 6.68: PV output power variation with SA-PR-GPSO algorithm with 4-peak PV property.

As shown in Fig. 6.65, when the PV outputs 2-peak property, the fast particle convergence can be achieved and the MPPT control can be approached approximately at the 20^{th} iteration. In Fig. 6.66, when the PV outputs 4-peak property, even though the PV output property fluctuates more intensely than the 2-peak case, the MPPT control also can be approximately achieved at the 20^{th} iteration. Similarly, as shown in Fig. 6.67 and 68, when the PV outputs 4-peak property, the global MPPT control is also achieved at approximately 20^{th} iteration.

6.4.4 SA-PR-GPSO Simulation with Variant Solar Irradiance

When the PV output changes from the 4-peak property to the 2-peak property, the MPPT performance of the proposed SA-PR-GPSO algorithm is shown in Fig. 6.69 and 70.

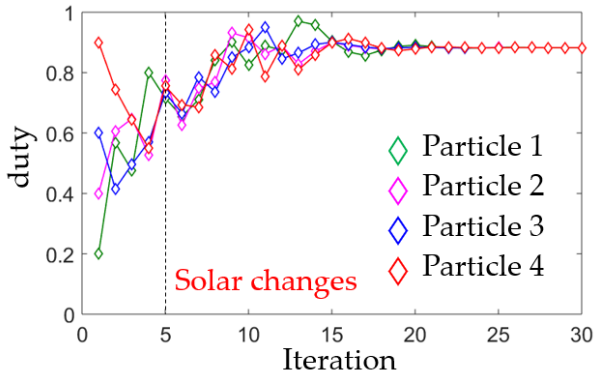

FIGURE 6.69: Duty variations of SA-PR-GPSO algorithm with 4-2-peak PV property.

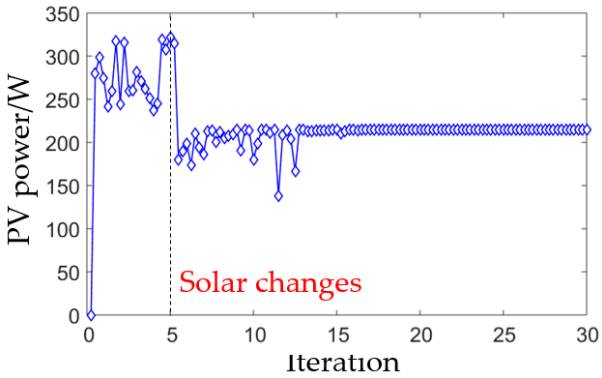

FIGURE 6.70: PV output power variation with SA-PR-GPSO algorithm with 4-2-peak PV property.

In the simulation, the solar irradiance variation happens at the 5^{th} iteration. In the SA-PR-GPSO process, before the 5^{th} iteration, the particle duties vary around 0.6 and the PV output power is approximately 280 W. After 5^{th} iteration, the particle duties gradually change to 0.9 and the PV output power drops to 200 W. After 20 iterationsa, the MPPT control has been achieved.

Based on the simulation results, it can be concluded that when the solar irradiance varies in the SA-PR-GPSO MPPT process, the particles can move to the new power peak automatically and then the MPPT control can be achieved. Furthermore, compared with the constant solar irradiance cases, the variant solar irradiance MPPT time is not obviously prolonged and the MPPT control is also achieved at the 20^{th} iteration. Therefore, with the SA-PR-GPSO algorithm, the MPPT control can be achieved with only one-time tracking process.

6.4.5 SA-PR-GPSO Experiment of Sweep Method with Constant Solar Irradiance

Under working conditions, with the proposed receiver side buck converter system topology, the MPPT algorithm frequency should be further reduced because the current in the WPT circuit can not be rapidly changed. In this case, the SA-PR-GPSO algorithm frequency is set as 3.3 Hz and the employed four particle duties are set as 0.2, 0.4, 0.6 and 0.9, respectively. When the PV outputs 2-peak property, the SA-PR-GPSO MPPT experiment result is shown in Fig. 6.71 and 72.

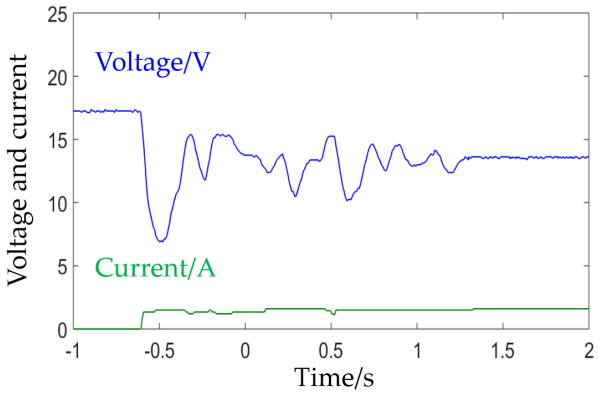

FIGURE 6.71: Voltage and current variations of SA-PR-GPSO algorithm with 2-peak PV output property.

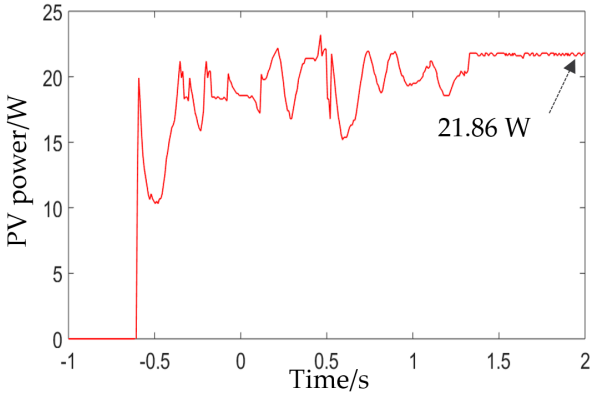

FIGURE 6.72: Power variations of SA-PR-GPSO algorithm with 2-peak PV output property.

It can be concluded that, the proposed SA-PR-GPSO algorithm MPPT time is approximately $t_{MPPT} = 1.9s$ and the tracked maximum power is approximately $P_{max} = 21.86W$. Furthermore, in the steady stage, the converter optimal duty is $d_{opt} = 0.7041$.

6.4.6 Experiment of Sweep Method with Constant Solar Irradiance

In the above simulation, the sweep frequency is not considered because there is no reference value of the simulation frequency. In this section, the sweep method is verified with experiments. The converter duty step d_{step} is set as 0.01 and 0.001, respectively. The sweep frequency f_{sweep} is set from 20 Hz to 2000 Hz, respectively. The sweep experiments results are shown in Tab. 6.3 and 4.

TABLE 6.3: Sweep method performance with $d_{step} = 0.01$

f_{sweep}/Hz	d_{opt}	V_{pv}/V	I_{pv}/A	P_{pv}/W	Time/s
200	0.89	15.11	1.34	20.24	0.41
100	0.85	14.89	1.42	21.14	0.81
66	0.84	14.67	1.47	21.56	1.22
50	0.81	14.62	1.48	21.63	1.62
40	0.81	14.55	1.49	21.67	2.02
33	0.80	14.45	1.51	21.81	2.43
28	0.80	14.43	1.52	21.93	2.83
25	0.80	14.43	1.52	21.93	3.24
22	0.79	14.43	1.52	21.93	3.64
20	0.80	14.33	1.52	21.78	4.05

TABLE 6.4: Sweep method performance with $d_{step} = 0.001$

f_{sweep}/Hz	d_{opt}	V_{pv}/V	I_{pv}/A	P_{pv}/W	Time/s
2000	0.898	15.16	1.32	20.01	0.40
1000	0.846	14.89	1.42	21.14	0.80
666	0.831	14.74	1.45	21.37	1.20
500	0.815	14.57	1.49	21.70	1.60
400	0.809	14.52	1.49	21.63	2.00
333	0.809	14.52	1.49	21.63	2.40
285	0.807	14.50	1.50	21.75	2.80
250	0.806	14.48	1.50	21.72	3.20
222	0.808	14.50	1.50	21.75	3.60
200	0.808	14.50	1.50	21.75	4.00

With the above data of sweep method and SA-PR-GPSO algorithm, Fig. 6.75-82 can be obtained.

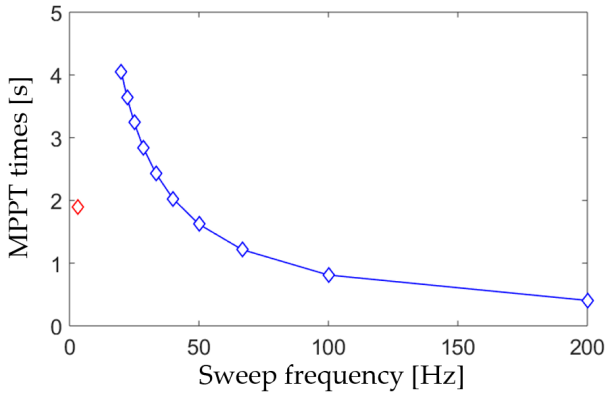

FIGURE 6.75: MPPT time variation at different frequencies in sweep method.

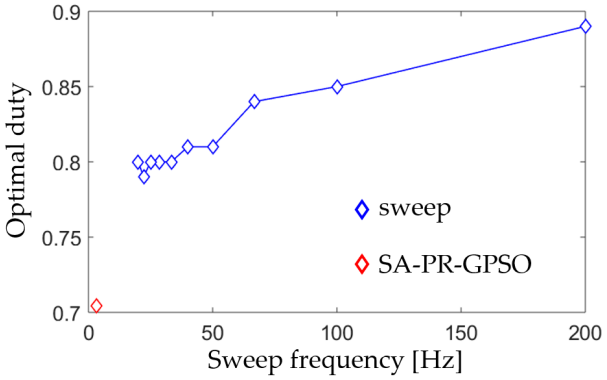

FIGURE 6.73: Optimal duty variation at different frequencies in sweep method.

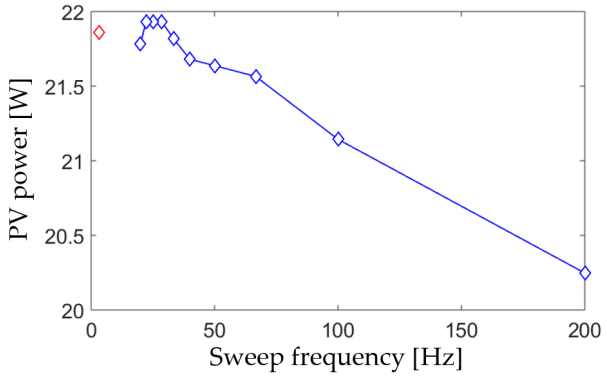

FIGURE 6.74: PV power variation at different frequencies in sweep method.

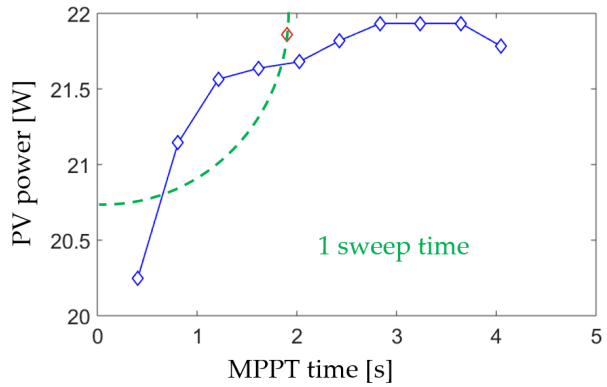

FIGURE 6.76: Performance assessment of PV power and MPPT time in sweep method with 1-time sweep process.

When the converter duty step $d_{step} = 0.01$, as shown in Fig. 6.76, it can be concluded that when the sweep frequency f_{sweep} is set as 100 Hz, 66 Hz and 50 Hz, the MPPT time of the sweep method is shorter than that of the SA-PR-GPSO algorithm. Furthermore, when f_{sweep} is set as 22 Hz, 25 Hz and 28 Hz, the tracked maximum PV power P_{pv} is higher than that of SA-PR-GPSO algorithm. However, suppose the effect zone as the area with the distance between the (0,22) and the SA-PR-GPSO point as the radius. Only the left side 3 points are better than the SA-PR-GPSO algorithm.

However, as analyzed in the above, of the solar irradiance changes in the sweep

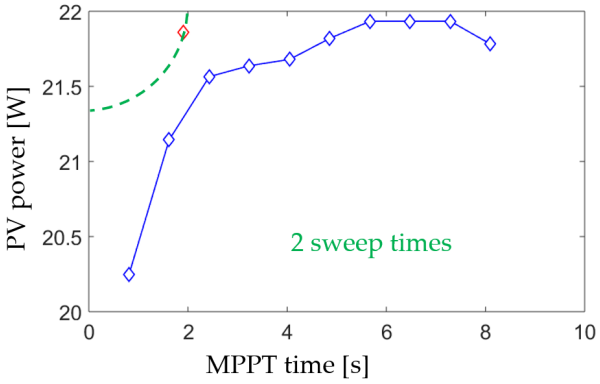

FIGURE 6.77: Performance assessment of PV power and MPPT time in sweep method with 2-time sweep processes.

process, at least the second sweep will be required. Therefore, calculate the 2 times of the sweep method time, the new effective zone can be obtained in Fig. 6.77. Therefore, with 2 sweep processes, the proposed SA-PR-GPSO algorithm possesses superiority over all the other sweep methods.

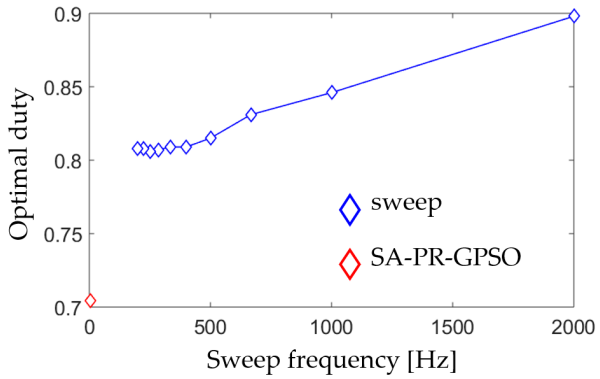

FIGURE 6.78: Optimal duty variation at different frequencies in sweep method.

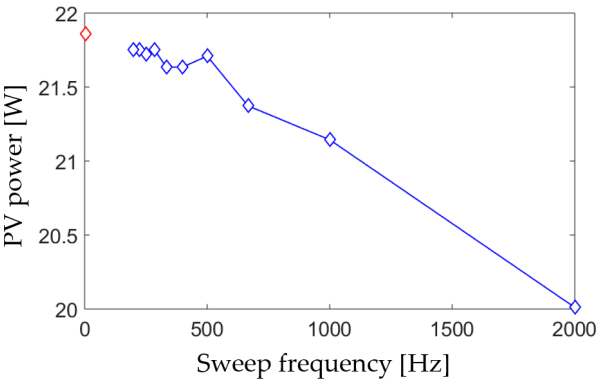

FIGURE 6.79: PV power variation at different frequencies in sweep method.

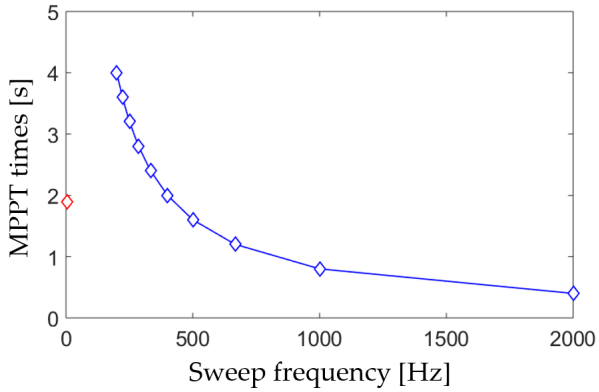

FIGURE 6.80: MPPT time variation at different frequencies in sweep method.

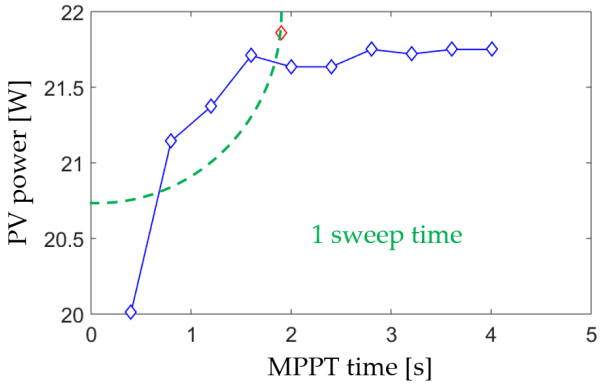

FIGURE 6.81: Performance assessment of PV power and MPPT time in sweep method with 1-time sweep process.

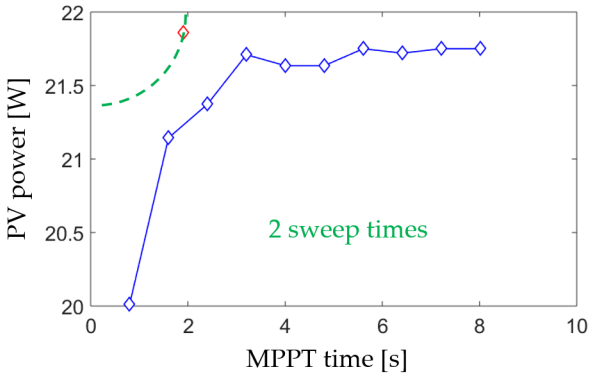

FIGURE 6.82: Performance assessment of PV power and MPPT time in sweep method with 2-time sweep processes.

When the converter duty step $d_{step} = 0.001$, as shown in Fig. 6.81, it can be concluded that when the sweep frequency f_{sweep} is set as 1000 Hz, 666 Hz and 500 Hz, the MPPT time of the sweep method is shorter than that of the SA-PR-GPSO algorithm. Furthermore, when f_{sweep} is set as 222 Hz, 250 Hz and 285 Hz, the tracked maximum PV power P_{pv} is higher than that of SA-PR-GPSO algorithm. However, suppose the effect zone as the area with the distance between the (0,22) and the

SA-PR-GPSO point as the radius. Only the left side 3 points are better than the SA-PR-GPSO algorithm.

However, as analyzed in the above, of the solar irradiance changes in the sweep process, at least the second sweep will be required. Therefore, calculate the 2 times of the sweep method time, the new effective zone can be obtained in Fig. 6.82. Therefore, with 2 sweep processes, the proposed SA-PR-GPSO algorithm possesses superiority over all the other sweep methods.

6.5 Proposed Algorithm Feasibility in Lunar Rover

In this paper, as introduced in the previous section, the CPU platform is the MYWAY PE-PRO and the detailed parameters are shown in Tab. 6.5.

TABLE 6.5: Employed CPU parameters

Item	Parameter
Processor	TMS320F28335
Processor Type	Floating Point
Internal Clock Frequency	150MHz
On-Chip RAM	34k $\times$ 16bit
Flash Memory	512k $\times$ 8bit
Serial EEPROM	64k $\times$ 8bit

In the lunar rover prototype, the designed to be employed CPU is the SH7708 series including the SH7708, SH7708S and SH7708R. The detailed parameters are shown in Tab. 6.6.

TABLE 6.6: Lunar rover prototype CPU paramters

Item	Parameter
Internal Clock Frequency	SH7708 60 MHz SH7708S 60 MHz SH7708R 100 MHz
Data Bus	8/16 bits
Memory Type	Mask ROM OTPROM EPROM EEPROM Flash memory SRAM
Memory Capacity	Maximum 32 Mbytes

In the experiment, the DSP AD is conducted at 20 kHz, which is far lower than the TMS320F28335 internal clock frequency. Furthermore, the SH7708 memory can be customized. Based on the SH7708 property, it can be concluded that the proposed algorithm is feasible for the lunar rover prototype.

6.6 Summary

In this chapter, in order to conduct the PV MPPT control, a local MPPT variant step InCon algorithm and 2 global MPPT SA-PR-GPSO and SA-PJ-PSO algorithms are proposed. In the proposed variant step incremental conductance method, the PV output power peak height is employed to tune the algorithm step to accelerate the tracking process. In the proposed SA-PR-GPSO algorithm, the tracking process is divided into the PR and GPSO stages. The PR stage is employed to replace the particles with Gaussian distribution at each iteration to accelerate the particle convergence and the GPSO stage is used to conduct the accurate optimal positioning. Similarly, the proposed SA-PJ-PSO algorithm also consists of two stages, namely the PJ stage and PSO stage. In the PJ stage, the fast particle convergence is achieved by particle jump and the following PSO stage is employed to conduct the accurate positioning. Furthermore, the sweep method feasibility is analyzed and it has been demonstrated that the sweep method need at least t times sweep to determine the optimal duty to conduct the PV global MPPT control under partial shading conditions. Finally, the proposed MPPT algorithm experiment verification is conducted based on the MYWAY PE-PRO which is constructed with TI TMS320F28335. The expected lunar rover prototype CPU is the SH7708 series. Based on the SH7708 series property, the proposed algorithm can be excecuted without obvious computation cost.

Chapter 7

Conclusion

In the conventional lunar rover structure, the PV panel is connected to the rover side instruments with a wire connection through the thermal insulation MLI materials. However, at lunar night, because the outside temperature is lower than -100°C, there will be a tremendous heat leakage along the wire from the rover body inside instruments to the outside circumstances. Because the heat leakage should be amended by the battery, an extra 40 kg battery volume module is required when the heat leakage is 20 W. In order to avoid the lunar rover heat leakage at lunar night, a WPT system is proposed and verified in this paper.

Firstly, the conventional wire connection between the PV and rover side instruments is replaced with a WPT system. The transmitter side is placed at the PV side, and the receiver side is placed in the rover body. In the thermal simulation of the lunar rover with a WPT system, because the physical connection between the rover body inside and outside circumstances is completely blocked, there is no heat leakage at all at lunar night, indicating the proposed WPT system structure is feasible.

Secondly, considering the position of the converter used to conduct the PV MPPT control, there are two WPT systems are proposed: the TC topology and RC topology. In the TC topology, the converter is directly connected to the PV at the transmitter side. The TC topology WPT system MPPT implementation feasibility has been verified with 1-peak PV output power property. Based on the experiment results, the tracking time is approximately 3 s, which is lower than the 10 s upper tracking time limit. In the RC topology, the converter is connected to the rectifier at the receiver side. Under working conditions, the rectifier output data is employed by the algorithm to conduct the MPPT control. The RC topology is verified by the multiple-peak PV output power properties. Based on the experiments, the global MPPT time is limited within 1.8 s, 1.9 s and 2.8 s for the 22 W, 29 W and 45 W cases, respectively. Comparing the TC and RC topologies, the PV output data can be directly employed by the TC topology WPT system, and then the tracking process can be less influenced by the data collection error. Furthermore, the PV and inverter can be isolated by the converter indicating the flyback current from the inverter will not influence the PV module, which can improve the lunar rover stability and extend the working life. However, on the other hand, because the MPPT algorithm should be conducted in digital way, the converter should be controlled based on the rover side control signal. Therefore, there are two consequences resulted in: the wireless communication should be conducted between the transmitter and receiver sides, and the converter needs to be assisted with extra thermal management system. In this way, the TC topology WPT system feasibility will be sharply reduced. In the RC topology, the rectifier output data is employed by the algorithm to conduct the MPPT control, and then it can be expected that the tracking performance will be slightly lower than that of TC topology. However, because there is no digital control required at the transmitter side, only based on the least facility the whole system can conduct the

MPPT control. Therefore, considering the great advantage of facility simplification, the disadvantage of accuracy decrease can be omitted and the RC topology is more suitable for the lunar rover WPT system.

Thirdly, at lunar night the Moon surface temperature is extremely low and the rover inside temperature should be kept at the room temperature to protect the instruments, and then the generated power at lunar day should be stored for the lunar night usage. In this paper, considering the relation of the PV, battery and load. A 6-mode power management strategy is proposed. In the proposed strategy, the PV and battery are only the power supply and request roles respectively, and the battery is employed as the buffer to achieve the power balance between the PV and load. For the TC and RC topologies, because the converter positions are different, the OPPT control methods mode are also different. The proposed power management strategy is verified by experiments, and based on the experiment results, all the 6 modes can be effective achieved. Furthermore, when the working condition changes, for example, the solar irradiance and load, the proposed power management strategy can automatically switch the working mode to cope with the changed system requirements.

Fourthly, due to the high temperature on the Moon surface at lunar day, the transmitter side WPT circuit device will encounter parameter variations. In this case, the WPT module properties will be changed, such as the system resonance frequency and optimal load. In order to tracking the maximum system DC-to-DC efficiency under the condition of parameter variations, a SA method is employed. The system DC-to-DC efficiency is employed as the system state energy, and both the inverter frequency and load are employed as the system perturb to conduct the global search. The proposed SA method is verified with simulations. In the simulation, 6 parameter variation cases with different preset nominal parameters are employed and all of them change to the same parameters in fact. With the proposed method, the maximums of Dc-to-DC efficiency of 6 cases are effectively tracked within 1 s and in general with lower parameter variations, the tracking time can be reduced.

Fifthly, the proposed PV MPPT algorithms can be divided into two categories, namely the local MPPT variant step InCon algorithm and the global MPPT SA-PR-GPSO as well as SA-PJ-PSO algorithms. In the variant step InCon method, the PV output P-V peak height is employed to tune the converter duty step to accelerate the tracking process. Compared with the conventional InCon method, the step can be increased when the P-V peak is not high enough compared with the preset standard to accelerate the system working point movement, and also can be decreased when the P-V peak is high enough to improve the tracking accuracy. Based on the experiment results, the tracking time is approximately 3 s compared with the 6 s tracking time of convention InCon method. When the partial shading condition happens, the global MPPT control should be conducted. In the proposed SA-PR-GPSO algorithm, the tracking process is composed of 2 stages, namely the PR stage and GPSO stage. In the first stage, the particles are replaced based on the Gaussian distribution to achieve the fast convergence to reduce the global peak search process, and in the second stage, the accurate optimal positioning will be conducted with the GPSO algorithm. When the PV output power possesses 4 peaks under partial shading conditions, the tracking time of the proposed SA-PR-GPSO algorithm is limited within 0.8 s compared with 2.4 s tracking time of conventional PSO algorithm. Similarly, the tracking process in the proposed SA-PJ-PSO algorithm is also divided into 2 stages, namely the PJ stage and PSO stage. In the first stage, the particles can jump into the interval where the current tracked maximum is to avoid invalid traversal of the intervals which have been verified that no potential particle positions can be found

to reduce the global peak search time. In the second stage, the accurate optimal positioning is conducted in PSO algorithm. Based on the experiment results, when there are 4 peaks at the P-V curve, the tracking time of the proposed SA-PJ-PSO algorithm is 1.4 s compared with 2.1 s of the conventional PSO algorithm.

Based on the above analysis, it can be concluded that the proposed RC WPT system is feasible and applicable for the lunar rover. For the future research, the system maximum DC-to-DC efficiency tracking research should be further optimized. Based on the WPT efficiency and power factor analysis in chapter 5, it can be expected that only the receiver side load variation can achieve the maximum tracking mission. Furthermore, the combination of the PV and WPT system can be promoted into more areas, such as the dynamic electric vehicle wireless charge.

Bibliography

[1] Fuke, Yasutaka, and Eric Krotkov. "Dead reckoning for a lunar rover on uneven terrain." Proceedings of IEEE International Conference on Robotics and Automation. Vol. 1. IEEE, 1996.

[2] Simmons, Reid, et al. "Experience with rover navigation for lunar-like terrains." Proceedings 1995 IEEE/RSJ International Conference on Intelligent Robots and Systems. Human Robot Interaction and Cooperative Robots. Vol. 1. IEEE, 1995.

[3] Basilevsky, A. T., et al. "Morphometry of small impact craters in the Lunokhod-1 and Lunokhod-2 study areas." Planetary and Space Science 92 (2014): 77-87.

[4] "Lunokhod 1." Wikipedia, Wikimedia Foundation, 2 Dec. 2019, https://en.wikipedia.org/wiki/Lunokhod_1.

[5] "Lunar Roving Vehicle." Wikipedia, Wikimedia Foundation, 3 Nov. 2019, https://en.wikipedia.org/wiki/Lunar_Roving_Vehicle.

[6] Salzberg, I. M. "Tracking the Apollo lunar rover with interferometry techniques." Proceedings of the IEEE 61.9 (1973): 1233-1236.

[7] Severny, A. B., E. I. Terez, and A. M. Zvereva. "The measurements of sky brightness on Lunokhod-2." The Moon 14.1 (1975): 123-128.

[8] Basilevsky, A. T., et al. "Geologic characteristics of the Luna 17/Lunokhod 1 and Chang'E-3/Yutu landing sites, northwest Mare Imbrium of the Moon." Planetary and Space Science 117 (2015): 385-400.

[9] Peng, W. X., et al. "Active particle-induced X-ray Spectrometer for CHANG'E-3 YuTu Rover Mission and its first results." 45th Lunar and Planetary Science Conference. 2014.

[10] Heldmann, J. L., et al. "Mojave volatiles prospector (MVP): Science and operations results from a lunar polar rover analog field campaign." (2015).

[11] Morkos, Beshoy, et al. Development of Endurance Testing Apparatus Simulating Wheel Dynamics and Environment on Lunar Terrain. No. 2010-01-0765. SAE Technical Paper, 2010.

[12] Williams, J-P., et al. "The global surface temperatures of the moon as measured by the diviner lunar radiometer experiment." Icarus 283 (2017): 300-325.

[13] Johnson, Francis S. "Lunar atmosphere." Reviews of Geophysics 9.3 (1971): 813-823.

[14] Landis, Geoffrey A., et al. "Photovoltaic power for a lunar base." Acta Astronautica 22 (1990): 197-203.

[15] Langseth, Marcus G., Stephen J. Keihm, and Kenneth Peters. "Revised lunar heat-flow values." Lunar and Planetary Science Conference Proceedings. Vol. 7. 1976.

[16] Pettit, Edison, and Seth B. Nicholson. "Lunar radiation and temperatures." The Astrophysical Journal 71 (1930): 102-135.

[17] Balasubramaniam, Ramaswamy, et al. "Analysis of solar-heated thermal wadis to support extended-duration lunar exploration." Journal of Thermophysics and Heat Transfer 25.1 (2011): 130-139.

[18] Sternovsky, Zoltan, et al. "Variability of the lunar photoelectron sheath and dust mobility due to solar activity." Journal of Geophysical Research: Space Physics 113.A10 (2008).

[19] Miller, Steven D., and Robert E. Turner. "A dynamic lunar spectral irradiance data set for NPOESS/VIIRS day/night band nighttime environmental applications." IEEE Transactions on Geoscience and Remote Sensing 47.7 (2009): 2316-2329.

[20] Stubbs, Timothy J., Richard R. Vondrak, and William M. Farrell. "A dynamic fountain model for lunar dust." Advances in Space Research 37.1 (2006): 59-66.

[21] Zook, Herbert A., and James E. McCoy. "Large scale lunar horizon glow and a high altitude lunar dust exosphere." Geophysical Research Letters 18.11 (1991): 2117-2120.

[22] Kraner, Hobart W., et al. "Radioactivity of the lunar surface." Science 152.3726 (1966): 1235-1236.

[23] Korotev, Randy L. "Concentrations of radioactive elements in lunar materials." Journal of Geophysical Research: Planets 103.E1 (1998): 1691-1701.

[24] Patil, Omkar, et al. "Review on planetary rovers Lunokhod to curiosity and beyond." Research & Reviews: Journal of Space Science & Technology 7.1 (2018): 15-23.

[25] "JAXA Digital Preservation." http://jda.jaxa.jp/.

[26] Berkelman, Peter, et al. Design of a Day/Night Lunar Rover. No. CMU-RI-TR-95-24. CARNEGIE-MELLON UNIV PITTSBURGH PA ROBOTICS INST, 1995.

[27] Anderson, William, et al. "Variable thermal conductance link for lunar landers and rovers." 46th AIAA/ASME/SAE/ASEE Joint Propulsion Conference & Exhibit. 2010.

[28] Komle, N. I., et al. "Development of thermal sensors and drilling systems for lunar and planetary regoliths." Advances in Space Research 42.2 (2008): 363-368.

[29] Zhang, Jinhai, et al. "Volcanic history of the Imbrium basin: A close-up view from the lunar rover Yutu." Proceedings of the National Academy of Sciences 112.17 (2015): 5342-5347.

[30] Litaker, Harry, Shelby Thompson, and Robert Howard. "Human Habitation in a Lunar Electric Rover during a 14-Day Field Trial." Proceedings of the Human Factors and Ergonomics Society Annual Meeting. Vol. 54. No. 19. Sage CA: Los Angeles, CA: SAGE Publications, 2010.

[31] Hui, Shu Yuen Ron, Wenxing Zhong, and Chi Kwan Lee. "A critical review of recent progress in mid-range wireless power transfer." IEEE Transactions on Power Electronics 29.9 (2013): 4500-4511.

[32] Li, Joshua Le-Wei, et al. "Keynote speakers: Wireless power transfer: From long-distance transmission to short-range charging." 2013 IEEE International RF and Microwave Conference (RFM). IEEE, 2013.

[33] Jawad, Aqeel Mahmood, et al. "Opportunities and challenges for near-field wireless power transfer: A review." energies 10.7 (2017): 1022.

[34] Askari, Alex, et al. "Underwater wireless power transfer." 2015 IEEE Wireless Power Transfer Conference (WPTC). IEEE, 2015.

[35] Kesler, Morris, and Colin McCarthy. "Highly resonant wireless power transfer in subsea applications." WiTricity white paper (2013).

[36] "Wireless Power Transfer." Wikipedia, Wikimedia Foundation, 16 Nov. 2019, https://en.wikipedia.org/wiki/Wireless_power_transfer.

[37] Lumpkins, William. "Nikola Tesla's Dream Realized: Wireless power energy harvesting." IEEE Consumer Electronics Magazine 3.1 (2013): 39-42.

[38] "Tesla Wireless." Resonance Science Foundation, https://resonance.is/stanford-scientists-making-wireless-electricity-transmission-reality/tesla-wireless/.

[39] Kurs, Andre, et al. "Wireless power transfer via strongly coupled magnetic resonances." science 317.5834 (2007): 83-86.

[40] Wang, Hao, and Xin Li. "Review and research progress of wireless power transfer for railway transportation." IEEJ Transactions on Electrical and Electronic Engineering 14.3 (2019): 475-484.

[41] Mou, Xiaolin, et al. "Survey on magnetic resonant coupling wireless power transfer technology for electric vehicle charging." IET Power Electronics 12.12 (2019): 3005-3020.

[42] Li, Xun, Kwai Man Luk, and Baoyan Duan. "Multiobjective Optimal Antenna Synthesis for Microwave Wireless Power Transmission." IEEE Transactions on Antennas and Propagation 67.4 (2019): 2739-2744.

[43] Yi, Xianjin, et al. "A Microwave Power Transmission Experiment Based on the Near-Field Focused Transmitter." IEEE Antennas and Wireless Propagation Letters 18.6 (2019): 1105-1108.

[44] Marques, J-R., et al. "Joule-level high-efficiency energy transfer to subpicosecond laser pulses by a plasma-based amplifier." Physical Review X 9.2 (2019): 021008.

[45] Dickinson, R. M. "Evaluation of a microwave high-power reception-conversion array for wireless power transmission." (1975).

[46] Celeste, A., P. Jeanty, and G. Pignolet. "Case study in Reunion island." Acta Astronautica 54.4 (2004): 253-258.

[47] Yuwei, Zou, et al. "Current research situation and developing tendency about wireless power transmission." 2010 International Conference on Electrical and Control Engineering. IEEE, 2010.

[48] Jin, Ke, and Weiyang Zhou. "Wireless laser power transmission: A review of recent progress." IEEE Transactions on Power Electronics 34.4 (2018): 3842-3859.

[49] Xie, Liguang, et al. "Wireless power transfer and applications to sensor networks." IEEE Wireless Communications 20.4 (2013): 140-145.

[50] Ye, Zhao-Hong, et al. "Energy efficiency analysis of U-coil wireless power transfer system." IEEE Transactions on Power Electronics 31.7 (2015): 4809-4817.

[51] Wang, Zhi-Hui, et al. "Load detection model of voltage-fed inductive power transfer system." IEEE Transactions on Power electronics 28.11 (2013): 5233-5243.

[52] Sample, Alanson P., David T. Meyer, and Joshua R. Smith. "Analysis, experimental results, and range adaptation of magnetically coupled resonators for wireless power transfer." IEEE Transactions on industrial electronics 58.2 (2010): 544-554.

[53] Imura, Takehiro, and Yoichi Hori. "Maximizing air gap and efficiency of magnetic resonant coupling for wireless power transfer using equivalent circuit and Neumann formula." IEEE Transactions on industrial electronics 58.10 (2011): 4746-4752.

[54] Li, Siqi, and Chunting Chris Mi. "Wireless power transfer for electric vehicle applications." IEEE journal of emerging and selected topics in power electronics 3.1 (2014): 4-17.

[55] Zhang, Wei, and Chunting Chris Mi. "Compensation topologies of high-power wireless power transfer systems." IEEE Transactions on Vehicular Technology 65.6 (2015): 4768-4778.

[56] Lu, Fei, et al. "An inductive and capacitive combined wireless power transfer system withLC-compensated topology." IEEE Transactions on Power Electronics 31.12 (2016): 8471-8482.

[57] Jegadeesan, Rangarajan, and Yong-Xin Guo. "Topology selection and efficiency improvement of inductive power links." IEEE Transactions on Antennas and Propagation 60.10 (2012): 4846-4854.

[58] Pantic, Zeljko, and Srdjan M. Lukic. "Framework and topology for active tuning of parallel compensated receivers in power transfer systems." IEEE Transactions on Power Electronics 27.11 (2012): 4503-4513.

[59] Zhao, Jinbo, et al. "A general design method of primary compensation network for dynamic WPT system maintaining stable transmission power." IEEE Transactions on Power Electronics 31.12 (2016): 8343-8358.

[60] Villa, Juan L., et al. "High-misalignment tolerant compensation topology for ICPT systems." IEEE Transactions on Industrial Electronics 59.2 (2011): 945-951.

[61] Zhao, Lei, et al. "A misalignment-tolerant series-hybrid wireless EV charging system with integrated magnetics." IEEE Transactions on Power Electronics 34.2 (2018): 1276-1285.

[62] Zheng, Cong, et al. "High-efficiency contactless power transfer system for electric vehicle battery charging application." IEEE Journal of Emerging and Selected Topics in Power Electronics 3.1 (2014): 65-74.

[63] Gao, Yabiao, Kathleen Farley, and Zion Tse. "A uniform voltage gain control for alignment robustness in wireless EV charging." Energies 8.8 (2015): 8355-8370.

[64] Ibrahim, Mohammad, et al. " Advanced modeling of a 2-kW series series resonating inductive charger for real electric vehicle." IEEE Transactions on Vehicular Technology 64.2 (2014): 421-430.

[65] Buja, Giuseppe, Manuele Bertoluzzo, and Kishore Naik Mude. "Design and experimentation of WPT charger for electric city car." IEEE Transactions on Industrial Electronics 62.12 (2015): 7436-7447.

[66] Lee, Seung-Hwan, Jae-Hee Kim, and Jun-Ho Lee. "Development of a 60 kHz, 180 kW, over 85% efficiency inductive power transfer system for a tram." Energies 9.12 (2016): 1075.

[67] Lee, Seung-Hwan, and Robert D. Lorenz. "Development and validation of model for 95%-efficiency 220-W wireless power transfer over a 30-cm air gap." IEEE Transactions on Industry Applications 47.6 (2011): 2495-2504.

[68] Wu, Hunter H., et al. "A high efficiency 5 kW inductive charger for EVs using dual side control." IEEE Transactions on Industrial Informatics 8.3 (2012): 585-595.

[69] Huh, Jin, et al. "Narrow-width inductive power transfer system for online electrical vehicles." IEEE Transactions on Power Electronics 26.12 (2011): 3666-3679.

[70] Lin, Deyan, Cheng Zhang, and SY Ron Hui. " Mathematic analysis of omnidirectional wireless power transfer-Part-II three-dimensional systems." IEEE Transactions on Power Electronics 32.1 (2016): 613-624.

[71] Sample, Alanson P., David T. Meyer, and Joshua R. Smith. "Analysis, experimental results, and range adaptation of magnetically coupled resonators for wireless power transfer." IEEE Transactions on industrial electronics 58.2 (2010): 544-554.

[72] Jonah, Olutola, and Stavros V. Georgakopoulos. "Wireless power transfer in concrete via strongly coupled magnetic resonance." IEEE Transactions on Antennas and Propagation 61.3 (2012): 1378-1384.

[73] Qingxin, Yang, et al. "Direct field-circuit coupled analysis and corresponding experiments of electromagnetic resonant coupling system." IEEE Transactions on Magnetics 48.11 (2012): 3961-3964.

[74] Ahn, Dukju, and Maysam Ghovanloo. "Optimal design of wireless power transmission links for millimeter-sized biomedical implants." IEEE transactions on biomedical circuits and systems 10.1 (2015): 125-137.

[75] Knecht, Oliver, Roman Bosshard, and Johann W. Kolar. "High-efficiency transcutaneous energy transfer for implantable mechanical heart support systems." IEEE Transactions on Power Electronics 30.11 (2015): 6221-6236.

[76] Salam, Zainal, Jubaer Ahmed, and Benny S. Merugu. "The application of soft computing methods for MPPT of PV system: A technological and status review." Applied energy 107 (2013): 135-148.

[77] Kellogg, W. D., et al. "Generation unit sizing and cost analysis for stand-alone wind, photovoltaic, and hybrid wind/PV systems." IEEE Transactions on energy conversion 13.1 (1998): 70-75.

[78] Parida, Bhubaneswari, S_Iniyan, and Ranko Goic. "A review of solar photovoltaic technologies." Renewable and sustainable energy reviews 15.3 (2011): 1625-1636.

[79] Riffonneau, Yann, et al. "Optimal power flow management for grid connected PV systems with batteries." IEEE Transactions on sustainable energy 2.3 (2011): 309-320.

[80] Li, Xiangjun, Dong Hui, and Xiaokang Lai. "Battery energy storage station (BESS)-based smoothing control of photovoltaic (PV) and wind power generation fluctuations." IEEE transactions on sustainable energy 4.2 (2013): 464-473.

[81] Subudhi, Bidyadhar, and Raseswari Pradhan. "A comparative study on maximum power point tracking techniques for photovoltaic power systems." IEEE Transactions on sustainable energy 4.1 (2012): 89-98.

[82] Hsiao, Ying-Tung, and China-Hong Chen. "Maximum power tracking for photovoltaic power system." Conference Record of the 2002 IEEE Industry Applications Conference. 37th IAS Annual Meeting (Cat. No. 02CH37344). Vol. 2. IEEE, 2002.

[83] Zakzouk, Nahla E., et al. "Improved performance low-cost incremental conductance PV MPPT technique." IET Renewable Power Generation 10.4 (2016): 561-574.

[84] Bazzi, Ali M., and Philip T. Krein. "Ripple correlation control: An extremum seeking control perspective for real-time optimization." IEEE Transactions on Power Electronics 29.2 (2013): 988-995.

[85] Brunton, Steven L., et al. "Maximum power point tracking for photovoltaic optimization using ripple-based extremum seeking control." IEEE transactions on power electronics 25.10 (2010): 2531-2540.

[86] Won, Chung-Yuen, et al. "A new maximum power point tracker of photovoltaic arrays using fuzzy controller." Proceedings of 1994 Power Electronics Specialist Conference-PESC'94. Vol. 1. IEEE, 1994.

[87] Du, Yang, et al. "Designing localized MPPT for PV systems using fuzzy-weighted extreme learning machine." Energies 11.10 (2018): 2615.

[88] Duman, Serhat, Nuran Yorukeren, and Ismail H. Altas. "A novel MPPT algorithm based on optimized artificial neural network by using FPSOGSA for standalone photovoltaic energy systems." Neural Computing and Applications 29.1 (2018): 257-278.

[89] Koad, Ramdan BA, Ahmed Faheem Zobaa, and Adel El-Shahat. "A novel MPPT algorithm based on particle swarm optimization for photovoltaic systems." IEEE Transactions on Sustainable Energy 8.2 (2016): 468-476.

[90] Li, Hong, et al. "An overall distribution particle swarm optimization MPPT algorithm for photovoltaic system under partial shading." IEEE Transactions on Industrial Electronics 66.1 (2018): 265-275.

[91] Sundareswaran, Kinattingal, et al. "Development of an improved P&O algorithm assisted through a colony of foraging ants for MPPT in PV system." IEEE transactions on industrial informatics 12.1 (2015): 187-200.

[92] Hadji, Slimane, Jean-Paul Gaubert, and Fateh Krim. "Theoretical and experimental analysis of genetic algorithms based MPPT for PV systems." Energy Procedia 74 (2015): 772-787.

[93] Tey, Kok Soon, et al. "Improved differential evolution-based MPPT algorithm using SEPIC for PV systems under partial shading conditions and load variation." IEEE Transactions on Industrial Informatics 14.10 (2018): 4322-4333.

[94] Ishaque, Kashif, and Zainal Salam. "A deterministic particle swarm optimization maximum power point tracker for photovoltaic system under partial shading condition." IEEE transactions on industrial electronics 60.8 (2012): 3195-3206.

[95] dos Santos Coelho, Leandro, and Chu-Sheng Lee. "Solving economic load dispatch problems in power systems using chaotic and Gaussian particle swarm optimization approaches." International Journal of Electrical Power & Energy Systems 30.5 (2008): 297-307.

[96] Koad, Ramdan BA, Ahmed Faheem Zobaa, and Adel El-Shahat. "A novel MPPT algorithm based on particle swarm optimization for photovoltaic systems." IEEE Transactions on Sustainable Energy 8.2 (2016): 468-476.

[97] Shongwe, Samkeliso, and Moin Hanif. "Comparative analysis of different single-diode PV modeling methods." IEEE Journal of Photovoltaics 5.3 (2015): 938-946.

[98] Ahmed, Jubaer, and Zainal Salam. "A Maximum Power Point Tracking (MPPT) for PV system using Cuckoo Search with partial shading capability." Applied Energy 119 (2014): 118-130.

Publication List

Journal Paper

[1] **Author**: Bingcheng Ji, Katsuhiro Hata, Takehiro Imura, Yoichi Hori, Sayuri Honda, Shuhei Shimada, Osamu Kawasaki
Title: A Novel Particle Jump Particle Swarm Optimization Method for PV MPPT Control under Partial Shaing Conditions
State: Accepted
Journal: IEEJ Journal of Industry Applications, Vol. 9, No. 4

[2] **Author**: Bingcheng Ji, Katsuhiro Hata, Takehiro Imura, Yoichi Hori, Shuhei Shimada, Osamu Kawasaki
Title: PV MPPT Control under Partial Shading Conditions with a Particle Replacement Gaussian Particle Swarm Optimization Method
State: Accepted
Journal: IEEJ Journal of Industry Applications, Vol. 9, No. 4

[3] **Author**: Bingcheng Ji, Katsuhiro Hata, Takehiro Imura, Yoichi Hori, Shuhei Shimada, Osamu Kawasaki
Title: Lunar Rover PV Powered Wireless Power Transfer System MPPT Control with Receiver Side Converter and Power Management Strategy
State: Under review
Journal: IEEE Transactions on Industrial Electronics

[4] **Author**: Bingcheng Ji, Katsuhiro Hata, Takehiro Imura, Yoichi Hori, Shuhei Shimada, Osamu Kawasaki
Title: Wireless Power Transfer System Design with Power Management Strategy Control for Lunar Rover
State: Accepted
Journal: IEEJ Journal of Industry Applications, Vol. 9, No. 4

[5] **Author**: Bingcheng Ji, Katsuhiro Hata, Takehiro Imura, Yoichi Hori, Shuhei Shimada, Osamu Kawasaki
Title: Two Dimension Maximum Efficiency Tracking Method for Wireless Power Transfer System with Parameter Variation
State: Under review
Journal: Journal of Advanced Simulation in Science and Engineering

Conference Paper

[1] B. Ji, et al. "MPPT Mode Controlled Solar Battery Assisted Lunar Rover Wireless Power Transfer System with Constant Voltage Load Experiment", IEICE Technical Report, vol 118, no 115, 2018

[2] B. Ji, et al. "Basic Study of Solar Battery Powered Wireless Power Transfer System with MPPT Mode and DC Bus Stabilization for Lunar Rover", IECON 2018-44th Annual Conference of the IEEE Industrial Electronics Society. IEEE, 2018.

[3] B. Ji, et al. "MPPT Control for PV based Wireless Power Transfer System in Lunar Rover by Secondary Side Converter", 2019 IEEE PELS Workshop on Emerging Technologies: Wireless Power (WoW2019), Jun 2019

[4] B. Ji, et al. "PV MPPT Control under Partial Shading Conditions in Lunar Rover Wireless Power Transfer System", IEICE Technical Report, vol 119, no 218, 2019

[5] B. Ji, et al. "Comparative Study on Converter Position for Lunar Rover Wireless Power Transfer System with PV MPPT Control", AWPT 2019

Pending Patent

[1] 月面探査機の無線給電システムのデザインと実験研究制御システムおよび制御方法

Award

[1] 2019年度電子情報通信学会無線電力伝送研究会若手奨励賞